SAPIENZA
UNIVERSITÀ DI ROMA

Probing new physics with exotic compact objects: the role of fermion soliton stars

Scuola dottorale in scienze astronomiche, chimiche, fisiche, matematiche e della terra "Vito Volterra"
Dottorato di Ricerca in Fisica (XXXVII cycle)

Loris Del Grosso
ID number 1705231

Advisor	Co-Advisor
Prof. Paolo Pani	Prof. Alfredo Urbano

Academic Year 2023/2024

Probing new physics with exotic compact objects: the role of fermion soliton stars

PhD thesis. Sapienza University of Rome

This thesis has been typeset by LaTeX and the Sapthesis class.

Version: December 20, 2024

Author's email: loris.delgrosso@uniroma1.it

Abstract

Many of the biggest puzzles in physics, such as the nature of dark matter and the behavior of spacetime singularities, stem from the interplay between gravity and quantum mechanics. Compact objects, like neutron stars and black holes, offer a unique setting to investigate these questions, as they probe strong gravitational fields and may be the only possible way to observe dark particles. With the recent discovery of gravitational waves, we now have an uncharted way to study such extreme environments, potentially shedding light on those fundamental issues.

This thesis focuses on fermion soliton stars, a class of compact objects that emerge from a theory in which a nonlinear self-interacting scalar field couples with fermions via a Yukawa interaction, resulting in an effective fermion mass that depends on the fluid properties. We elucidate the fundamental features of this model and its links to the Standard Model and beyond. Moreover, we provide distinctive signatures of the model in the gravitational wave signal, offering a way to distinguish fermion soliton stars from other types of compact objects.

*

* *

* *

Finis studiorum, non finis quaerendi.

* —***Anonymous*** *

Preface

The research presented in this thesis was conducted at Sapienza University of Rome, within the Gravity Theory and Gravitational Wave Phenomenology Group. Part of this work was also performed at Johns Hopkins University in Baltimore, which I kindly thank for the hospitality.

List of publications

The work in this thesis is based on the following publications:

- Title: Fermion soliton stars
  Journal: Phys. Rev. D 108, 044024 (2023), arXiv:2301.08709 [gr-qc]
  Authors: **Loris Del Grosso**, Gabriele Franciolini, Paolo Pani, Alfredo Urbano
- Title: Fermion soliton stars with asymmetric vacua
  Journal: Phys. Rev. D 108, 064042 (2023), arXiv:2308.15921 [gr-qc]
  Authors: **Loris Del Grosso**, Paolo Pani
- Title: Compact objects in and beyond the Standard Model from non-perturbative vacuum scalarization
  Journal: Phys. Rev. D 109, 095006 (2024), arXiv:2401.06716 [hep-ph]
  Authors: **Loris Del Grosso**, Paolo Pani, Alfredo Urbano
- Title: Tidal Love numbers and approximate universal relations for fermion soliton stars
  Journal: Phys. Rev. D 109, 124008 (2024), arXiv:2404.06979 [gr-qc]
  Authors: Emanuele Berti, Valerio De Luca, **Loris Del Grosso**, Paolo Pani

Acronyms

BH: black hole
BSM: beyond the Standard Model
ECO: exotic compact object
EOS: equation of state
ET: Einstein Telescope
FSS: fermion soliton star
GW: gravitational wave
HSC: Hyper Suprime-Cam
ISCO: innermost stable circular orbit
KAGRA: Kamioka Gravitational Wave Detector
LHC: Large Hadron Collider
LIGO: Laser Interferometer Gravitational-Wave Observatory
LISA: Laser Interferometer Space Antenna
LVK: Ligo-Virgo-Kagra collaboration
MSSM: minimal supersymmetric Standard Model
NS: neutron star
NTS: non-topological soliton
OGLE: Optical Gravitational Lensing Experiment
PBH: primordial black hole
PN: post-Newtonian
QCD: quantum chromodynamics
QNM: quasinormal mode
SM: Standard Model
STF: symmetric trace-free
TLN: tidal Love number
TOV: Tolman-Oppenheimer-Volkoff
VEV: vacuum expectation value
WEC: weak energy condition

Contents

Chapter 1

Introduction

The realm of physics underwent deep revolutions during the twentieth century. First of all, spacetime, which for Newton was absolute and equal to itself in all points of the Universe, was shown to be rather a dynamic object, whose properties (including the rate at which time passes) highly depend on the velocity of the observer and the local matter distribution. That was the most profound lesson taught by the theories of special and general relativity, proposed by Einstein, respectively, in 1905 and 1916. Corroborated by many experimental tests, the theory of gravity that arose after Einstein's work has established itself as our best theory to probe the world of the infinitely big, from the scale of the solar system to the size of the observable Universe.

The second revolution was the discovery of quantum mechanics, which allowed the human mind to penetrate the bizarre laws of the infinitely small. This theoretical success was intimately connected with an intense experimental activity aimed at shedding light on the subatomic world, which began with the discovery of the electron by Thomson in 1897. Such an incredible effort, both on the theoretical and experimental side, reached its highest moment in the 1970s, when people realized that quantum field theory, a theoretical framework developed to unify both the laws of quantum mechanics and special relativity, was successful in explaining all the collected experimental evidence, once a relatively small number of fields and interactions were assumed. That was the discovery of the so-called *Standard Model of particle physics* (SM).

During the last decades, the SM has successfully passed extremely precise experimental tests, without showing signs of failure. However, there are strong reasons, both on the theoretical and experimental side, to believe that the Standard Model is not complete. For example, observations ranging from the galactic to the cosmological scales, suggest that the baryonic matter observed in the Universe is just a small fraction ($\sim 16\,\%$) of the *total matter* content of the Universe. The missing $\sim 84\,\%$ is called *dark matter* [5]. Whether dark matter consists of particles, classical fields, macroscopic bodies, or a combination of these, the simplest explanations require introducing new ingredients or mechanisms into the Standard Model.

Moreover, a quantum theory that fully embeds gravitational interactions into the Standard Model is missing. The conceptual difficulties that arise when one tries to unify the two pillars of fundamental physics, quantum field theory and general relativity, can be understood heuristically as follows.

Quantum field theory teaches us that to probe the world at a distance $\sim \Delta x$, we must concentrate an energy $E \sim \hbar c/\Delta x$ in that region. The smaller the region we want to probe, the higher the energy needed. This process can not continue forever. Indeed, when Δx becomes comparable with the Schwarzschild radius corresponding to the pumped energy, i.e. $\Delta x \sim G\,E/c^4$, general relativity predicts that the region collapses into a black hole. Thus, imposing that $E \sim \hbar c/\Delta x \sim c^4 \Delta x/G$ leads to $\Delta x \sim \sqrt{\hbar\, G/c^3} \sim 10^{-35}\,\mathrm{m}$. Under this length scale, called *Planck length* and denoted as l_p, the fundamental degrees of freedom of the theory are changing and new phenomena are expected to take place (such as Hawking's evaporation of these microscopic black holes). The corresponding energy scale is $m_p\, c^2 \sim \hbar c/l_p \sim 10^{19}\,\mathrm{GeV}$, where m_p is called *Planck mass*.

We cannot fail to mention also a further revolution brought about by the explosion of statistical mechanics as a tool for investigating the world of the infinitely complex. It is conceivable that interactions among these three fundamental pillars (general relativity, quantum field theory, and statistical mechanics) will generate new and fertile ideas able to push further the frontiers of human knowledge.

1.1 Compact objects as a bridge between the micro and the macro world

Based on the previous argument, one may think that the only way to reach the quantum gravity regime is by probing the Planck length, which requires an energy $E \sim 10^{19}\,\mathrm{GeV}$, many orders of magnitude larger than the energy currently available at the world's biggest collider, the Large Hadron Collider (LHC).

There is however another possible path to the quantum regime, which uses strong classical fields. Indeed, one expects that when the intensity of a classical field exceeds a critical threshold, quantum effects show up. For example, when a constant electric field E becomes bigger than

$$E_c \sim \frac{m_e}{e} \sim 10^{18}\,\mathrm{V/m}\,, \tag{1.1}$$

where m_e is the electron mass and e is the elementary charge, electron-positron pairs are spontaneously created, causing the decay of the electric field, which is a macroscopic measurable effect. This is the so-called *Schwinger pair production* [6].

In a similar spirit, it is conceivable that in the vicinity of a compact self-gravitating object (such as black holes and neutron stars), where the gravitational field is *strong*, quantum effects show up on scales much bigger than the Planck length, potentially leading to a measurable effect.

Even forgetting about quantum gravity considerations, the aforementioned dark matter problem may require, as discussed, introducing new ingredients into the Standard Model (SM). If new particles exist in Nature, they may clump together to form macroscopic self-gravitating objects, as happens for neutron stars. Such exotic compact objects (ECOs) would naturally be decoupled (or only feebly interacting) with other Standard Model particles/fields, playing naturally the role of dark matter candidates (see 2.5).

The detection of gravitational waves [7] inaugurated a hitherto uncharted window into the Universe, paving the way to the exploration of the strong gravity regime around conventional compact objects (black holes and neutron stars), as well as the possibility of probing the existence of exotic compact objects and indirectly physics beyond the Standard Model. Indeed, the discovery of an ECO in a binary merger through gravitational wave observation, would indirectly shed light on the existence of elusive particles.

These arguments clearly show that compact objects are *a bridge between the micro and the macro worlds.* As further proof of this fact, we may consider the formula expressing the maximum mass for a given model of compact objects. This explicitly links the macroscopic properties of the objects (such as mass and radius), with the parameters of the underlying microscopic theory (such as the mass of the fundamental particle). For example, let us consider the formula expressing the maximum mass M_c of a fermion star (such as a neutron star),

$$M_c \sim \frac{1}{m^2}\left(\frac{\hbar c}{G}\right)^{3/2}, \tag{1.2}$$

where m is the fermion mass (where the omitted $\mathcal{O}(1)$ prefactor depends on the particular equation of state chosen). We explicitly see that the above formula depends on a microscopic parameter, m, and on several fundamental constants, including the reduced Planck constant $\hbar$, characterizing the quantum world, and Newton's gravitational constant G, which concerns the biggest scales in the Universe.

1.2 Fermion soliton stars

In light of the previous arguments, the quest for physically motivated theories that give rise to exotic compact objects appears extremely compelling.

This thesis focuses on fermion soliton stars, a class of compact objects that emerge from the following theory

$$S = \int \mathrm{d}^4x\sqrt{-g}\Big[\frac{R}{16\pi G} - \frac{1}{2}\partial^\mu\phi\partial_\mu\phi - U(\phi) + \bar{\psi}(i\gamma^\mu D_\mu - m_f)\psi + f\phi\bar{\psi}\psi\Big], \tag{1.3}$$

describing a real scalar field ϕ and a fermion field ψ that interact through a Yukawa term. A pictorial representation of these compact objects is shown in Fig. 1.1. The choice of the scalar potential $U(\phi)$ is crucial in determining the macroscopic properties of the fermion soliton stars (see Table 1.1).

This simple field theory enjoys three fundamental properties:

- the matter Lagrangian for ϕ and ψ is renormalizable, in contrast to the widely used model describing solitonic boson stars [8, 9, 10, 11] in which the scalar potential is non-renormalizable and field values should not exceed the limit of validity of the corresponding effective field theory;

- the underlying Lagrangian is local and, together with the previous point, this ensures that all the physics derived from it will not give rise to a superluminal speed of sound;

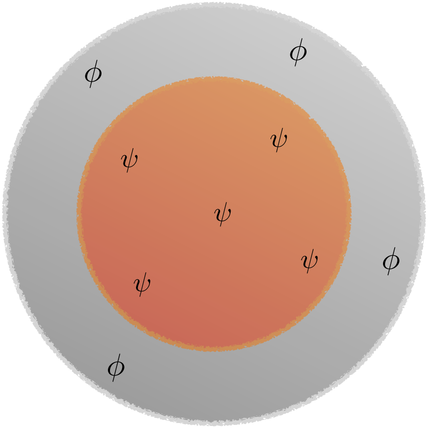

Figure 1.1. A pictorial illustration of a fermion soliton star. The inner region is dominated by fermions ψ, smoothly connected, and surrounded by, an outer layer made of the scalar field ϕ.

- arises in the SM and several BSM extensions, such as asymmetric dark matter models [12].

Model	**Potential** $U(\phi)$	**Maximum mass** $M_c/M_\odot$	**Confining regime**
Symmetric	$\frac{1}{2}\mu^2\phi^2\left(1-\frac{\phi}{\phi_0}\right)^2$	$3\left(\frac{500\,\mathrm{GeV}}{\mu}\right)\left(\frac{10^7\mathrm{GeV}}{\phi_0}\right)^2$	$m_f > 6\left(\frac{\mu}{m_p}\right)^{1/2}\phi_0$
Asymmetric	$\frac{\mu^2}{2!}\phi^2+\frac{\kappa}{3!}\phi^3+\frac{\lambda}{4!}\phi^4$	$\sim\left(\frac{\mathrm{GeV}}{\mu}\right)\left(\frac{\mathrm{GeV}}{\phi_0}\right)$	$m_f \gtrsim (\mu\phi_0)^{1/2}$
Mexican hat	$\frac{\lambda}{16}\left(\phi^2-\phi_0^2\right)^2$	$0.1\left(\frac{\mathrm{GeV}}{\mu}\right)\left(\frac{\mathrm{GeV}}{\phi_0}\right)$	$m_f > 2(\mu\phi_0)^{1/2}$

Table 1.1. Scalar potential, maximum mass, and confining regime for different fermion soliton star models. The parameters μ, ϕ_0 are, respectively, the bare mass and the vacuum expectation value of the scalar field, while m_f is the bare mass of the fermion. For asymmetric fermion soliton stars, there are $\mathcal{O}(1)$ coefficients that depend on the energy difference between the false and the true vacuum. In all three cases, the maximum compactness is ≈ 0.27. The scaling of the maximum mass is valid in the *confining regime* of the particular model, i.e. when $\phi_0/m_p \ll 1$ and, at the same time, the correspondent condition on m_f is met.

About forty years ago, Lee and Pang proposed the first version of the model with a symmetric scalar potential [13]. Working in a thin-wall limit in which the scalar field is a step function, for some values of the parameters, Lee and Pang obtained approximated solutions describing fermion soliton stars.

It is worth spending some words on the meaning of the term *soliton*, to avoid confusion that often arises reading the literature. We will define a *soliton* as a solution to a nonlinear wave equation that is localized with finite energy, everywhere regular, and compatible with an asymptotically flat spacetime. In the context of the present model, the nonlinear wave equation is provided by the equation of motion of the real scalar field ϕ (see e.g. sec. 3.1.1).

1.2.1 Outline and general structure

In Chapter 2, we present a concise introduction to the physics of compact objects. In Chapters 3 and 4, we show that fermion soliton stars exist beyond the thin-wall approximation, and we build exact static solutions within General Relativity. Moreover, we elucidate some key properties of the model, in particular the role of the effective fermion mass provided by the Yukawa coupling, and the consequences of a scalar potential with generic asymmetric vacua. We explore the model systematically, presenting mass-radius diagrams and the maximum compactness of fermion soliton stars for various choices of the parameters. In Chapter 5 we investigate applications of the previous findings adopting a particle physics perspective, presenting the mechanism of non-perturbative vacuum scalarization as a support mechanism for new compact objects that can form in the early Universe, can collapse into primordial black holes (PBHs) through accretion past their maximum mass, and serve as dark matter candidates. In Chapter 6, we briefly discuss the main possibilities to test ECOs through gravitational wave observations. Finally, in Chapter 7 we investigate the tidal deformations of fermion soliton stars and compute the corresponding tidal Love numbers for different model parameters, highlighting how this information can be used to disentangle fermion soliton stars from other families of compact objects.

In this thesis, we use natural units $\hbar = c = 1$, and the $(-,+,+,+)$ signature. We define the Planck mass through $G = m_p^{-2}$.

Chapter 2

The physics of compact objects: an introduction

2.1 Compact objects: the end point of gravitational collapse

Imagine a region of space filled with a (large) set of neutral massive particles. On scales much bigger than the typical inter-particle separation, the system is effectively described as a macroscopic fluid. In the simplest case, both viscosity and heat flow are absent and, therefore, the short-distance dynamics is fully captured, in the hydrodynamic limit, using only two functions, the energy density $\epsilon(x)$ and the pressure $p(x)$, where $x = (ct, \boldsymbol{x})$ is the spacetime point.

Since the particles are electrically neutral, the only long-range force acting on the system is gravity. Assuming that the fluid is non-relativistic (i.e. $\epsilon \approx \rho$, being ρ the mass density and $p \ll \rho$), gravitational interactions will be well-described through the Newtonian gravitational potential $\Phi(x)$. Let us call $\boldsymbol{u}(x)$ the (spatial) velocity of the fluid element located at $\boldsymbol{x}$ at time t. Then, the relevant equations are [14]

$$\partial_t \rho = -\boldsymbol{\nabla} \cdot (\rho\, \boldsymbol{u})\,, \tag{2.1}$$

$$(\partial_t + \boldsymbol{u} \cdot \boldsymbol{\nabla})\boldsymbol{u} = -\frac{\boldsymbol{\nabla} p}{\rho} - \boldsymbol{\nabla}\Phi\,, \tag{2.2}$$

$$\nabla^2 \Phi = 4\pi G \rho\,. \tag{2.3}$$

Eq. (2.1) is the continuity equation. It states that if there is a variation in the mass density ρ inside some fixed volume, this has to come from particles that enter or leave the volume. Eq. (2.2) is the Euler equation and comes from the momentum conservation. Finally, eq. (2.3) is the Poisson equation, describing the gravitational potential Φ generated by the source ρ.

To close the system of equations, we need to specify an equation of state, i.e. a relation between ρ and p of the form $p = p(\rho, T)$, where T is the temperature of the fluid. Such a relation is dictated by the microphysics of the system. For simplicity, we will consider a barotropic fluid, where $p = p(\rho)$ only.

2.1.1 Ignoring gravity

It is instructive to first consider the case where gravity is absent, i.e. $\Phi \equiv 0$. In this regime, a solution for the previous system of equations is simply $\bar{\boldsymbol{u}} \equiv 0$, $\rho = \bar{\rho}$, and $p = \bar{p}$, where $\bar{\rho}$ and $\bar{p}$ are just two constants. The latter solution describes an infinite, static fluid, i.e. not evolving in time. On top of this, we now add small perturbations, by writing $\rho = \bar{\rho} + \delta\rho$ and $p = \bar{p} + \delta p$. The equations for the perturbations $\delta\rho$ and δp are obtained by linearizing eqs. (2.1) to (2.3)

$$\partial_t \delta\rho = -\boldsymbol{\nabla} \cdot (\bar{\rho}\, \boldsymbol{u}) \,, \tag{2.4}$$

$$\bar{\rho}\, \partial_t \boldsymbol{u} = -\boldsymbol{\nabla} \delta p \,. \tag{2.5}$$

Acting with a further time derivative on eq. (2.4) and using eq. (2.5), gives

$$\partial_t^2 \delta\rho - \nabla^2 \delta p = 0 \,. \tag{2.6}$$

Since the fluid is barotropic, the pressure perturbation can be written as

$$\delta p = \frac{\partial p}{\partial \rho} \delta\rho \equiv c_s^2 \delta\rho \,, \tag{2.7}$$

where c_s is the sound speed of the fluid. Substituting the latter expression in eq. (2.6) gives

$$(\partial_t^2 - c_s^2 \nabla^2) \delta\rho = 0 \,, \tag{2.8}$$

which is a wave equation. Hence, the solutions will be sound waves

$$\delta\rho(t, \boldsymbol{x}) = A\, e^{i(\omega t - \boldsymbol{k} \cdot \boldsymbol{r})} \,, \tag{2.9}$$

where $\boldsymbol{k}$ is the wavevector, $\omega = c_s\, |\boldsymbol{k}|$ is the frequency, and $\lambda = 2\pi/|\boldsymbol{k}|$ is the wavelength of the wave.

2.1.2 Including gravity

Let us now switch on gravitational interactions. Formally, the configuration describing an infinite static fluid becomes ill-defined, since the solution of the Poisson equation eq. (2.3) with a constant density leads to a divergent gravitational potential Φ. Physically, this is merely a consequence of the fact that there are no infinite, static self-gravitating fluids. However, the physical point that we will highlight is not affected by these formal issues, which indeed can be cured through a suitable regularization procedure (such as enclosing the system in a large but finite volume).

Repeating the same steps as before, we obtain again a wave equation

$$(\partial_t^2 - c_s^2 \nabla^2) \delta\rho = 4\pi G \bar{\rho}\, \delta\rho \,, \tag{2.10}$$

but now the frequency ω of a monochromatic solution is given by the equation

$$\omega^2 = c_s^2 \boldsymbol{k}^2 - 4\pi G \bar{\rho} \,. \tag{2.11}$$

We notice that ω is either real or purely imaginary. The transition between the two regimes is controlled by the critical wavevector $\boldsymbol{k}_J$ such that $\omega^2 = 0$, i.e.

$$\boldsymbol{k}_J \equiv \frac{\sqrt{4\pi G\, \bar{\rho}}}{c_s} \,. \tag{2.12}$$

This parameter sets the fundamental scale of the system, called the *Jeans scale*. For small scales ($|\boldsymbol{k}| \gg |\boldsymbol{k}_J|$), the pressure dominates and we find the same oscillations as in the previous case. However, on large scales ($|\boldsymbol{k}| \ll |\boldsymbol{k}_J|$), gravity dominates, the frequency ω becomes imaginary and the solution of the perturbation is $\delta\rho \propto \exp(\pm\, t/\tau)$, where $\tau \equiv 1/\sqrt{4\pi G\,\bar{\rho}}$. The presence of this instability, where the density perturbation grows exponentially, determines the onset of the gravitational collapse.

To determine the actual fate of the system, a fully non-linear simulation, which also takes into account relativistic effects, is typically required. Still, it is conceivable that the late-time attractor solution will be a stationary, self-gravitating object, at least for some choices of the initial conditions. This intuition is confirmed by various numerical results (see for example [15, 16]).

2.2 Equations of stellar structure

2.2.1 The Newtonian equations for stellar structure

Based on the previous arguments, it appears extremely compelling to understand the properties of the stationary solutions to eqs. (2.1) to (2.3), since they represent the leftover of the gravitational collapse. For example, it is interesting to assess the allowed range of masses and radii where the final self-gravitating object lives. To achieve this, we simply take the static limit of eqs. (2.1) to (2.3), i.e. we assume that ρ, p, and Φ do not depend on time, while the fluid velocity $\boldsymbol{u}$ vanishes. To keep things as simple as possible, we further look for a spherical symmetric configuration, i.e. ρ, p, and Φ are taken to be only functions of the radial coordinate r. Then, eq. (2.1) becomes trivial, while eqs. (2.2) and (2.3) reduce to

$$\frac{dp}{dr} = -\rho\frac{d\Phi}{dr}\,, \tag{2.13}$$

$$\frac{1}{r^2}\frac{d}{dr}\Big(r^2\frac{d\Phi}{dr}\Big) = 4\pi G\rho\,. \tag{2.14}$$

It is convenient to integrate the last equation,

$$r^2\frac{1}{G}\frac{d\Phi}{dr} = 4\pi\int_0^r (r')^2\rho(r')dr'\,. \tag{2.15}$$

What appears on the right-hand side is nothing but the total mass $m(r)$ contained in a spherical shell of radius r. At this point, we can substitute back into eq. (2.13) obtaining one single equation,

$$\frac{dp}{dr} = -\frac{Gm(r)}{r^2}\rho(r)\,. \tag{2.16}$$

Physically, this equation demands hydrostatic equilibrium between gravitational interaction and internal pressure at any fluid element.

Adding to the latter equation also the definition of $m(r)$ (in differential form) and the equation of state, we obtain a set of three equations,

$$\frac{dm}{dr} = 4\pi r^2 \rho(r) \tag{2.17}$$

$$\frac{dp}{dr} = -\frac{Gm(r)}{r^2}\rho(r) \tag{2.18}$$

$$p = p(\rho)\,, \tag{2.19}$$

which describes the stellar structure in Newtonian gravity.

These equations have to be solved by first choosing a value ρ_c for the mass density at the center of the star, i.e. $\rho(0) = \rho_c$, and then integrating up to the point where the pressure vanishes, which defines the radius R of the star, i.e. $p(R) = 0$. The latter condition not only ensures that the fluid is localized in some finite region of space, but also guarantees the continuity of the solution at the radius of the star. Once the radius R is determined, the mass of the star will simply be $M = m(R)$.

2.2.2 Tolman-Oppenheimer-Volkoff equations

A crucial dimensionless parameter characterizing each equilibrium configuration is the modulus of the gravitational potential at the surface of the star, i.e. GM/R. This quantity is often called *compactness* and hereafter denoted as C. If $C \ll 1$, then the gravitational field near the surface of the object is weak and the Newtonian description we have been using so far is reliable. On the other hand, when $C \sim 1$, General Relativity effects become important and eqs. (2.17) to (2.19) must be corrected.

To this end, we recall that the stress-energy tensor describing a perfect fluid is covariantly written as

$$T^{\mu\nu} = (\epsilon + p)u^\mu u^\nu + p\, g^{\mu\nu}\,, \tag{2.20}$$

where ϵ and p are, respectively, the energy density (which reduces to the mass density ρ in the non-relativistic limit) and the pressure, while u^μ is the four-velocity of the fluid element, and $g^{\mu\nu}$ the metric of the spacetime. The latter is assumed to be static and spherically symmetric, conveniently described by the following line element

$$ds^2 = -e^{2u(r)}dt^2 + e^{2v(r)}dr^2 + r^2(d\theta^2 + \sin^2\theta d\varphi^2)\,, \tag{2.21}$$

in terms of two unknown functions $u(r)$ and $v(r)$.

The Einstein field equations $G_{\mu\nu} = 8\pi G\, T_{\mu\nu}$ on the spacetime given by eq. (2.21) lead to the following final set of equations

$$\frac{dm}{dr} = 4\pi r^2 \epsilon\,, \tag{2.22}$$

$$\frac{dp}{dr} = -\frac{G}{r^2}\frac{(\epsilon + p)[m(r) + 4\pi r^3 p]}{1 - \frac{2Gm(r)}{r}}\,, \tag{2.23}$$

where

$$m(r) \equiv \frac{r}{2G}(1 - e^{-2v(r)})\,. \tag{2.24}$$

The eqs. (2.22) and (2.23) are known as the *Tolman-Oppenheimer-Volkoff (TOV) equations.* Once an equations of state $p = p(\epsilon)$ is assigned, they fully characterize the stellar structure in General Relativity. In the Newtonian limit, where the fluid is non-relativistic ($\epsilon \approx \rho$, being ρ the mass density and $p \ll \rho$) and the gravitational field is weak ($\frac{2Gm(r)}{r} \ll 1$), we consistently recover eqs. (2.17) and (2.18). Notice that $m(r)$ acquires the physical meaning of total mass in a spherical shell of radius r only in the Newtonian limit. In the fully relativistic regime, it should be thought of just as a parametrization of the rr-component of the metric.

Regularity of the solution in the center of the star imposes the boundary condition $m(r = 0) = 0$. Moreover, in fully analogy with the Newtonian case, we must choose a central value of the energy density, i.e. $\epsilon(r = 0) = \epsilon_c$ (or, equivalently, a central value for the pressure). With these two boundary conditions, the TOV system can be numerically integrated up to the point where the pressure vanishes, i.e. $p(R) = 0$, which defines the radius of the star, as in the Newtonian analog. Once $m(r)$, $p(r)$, $\epsilon(r)$ and R have been found, the function $v(r)$ in eq. (2.21) is determined simply using eq. (2.24), whereas $u(r)$ is given by integrating the r-component of conservation law $\nabla_\nu T^{\mu\nu} = 0$, which gives

$$u(r) = -\int_0^r \frac{p'}{\epsilon + p} dr' + u_0 \,. \tag{2.25}$$

The constant $u_0 = u(r = 0)$ is determined by imposing the continuity of the metric at the surface of the star. Indeed, outside the star $\epsilon = p = 0$ and thus the solution must reduce to the Schwarzschild metric, by Birkhoff's theorem [17]. This leads to the condition

$$e^{2u_0} = \frac{1 - \frac{2Gm(R)}{R}}{e^{2\int_0^R -\frac{p'}{\epsilon+p} dr}} \,. \tag{2.26}$$

Finally, the mass of the star as determined by distant observes is

$$M = \int_0^R 4\pi r^2 \epsilon \, dr \,, \tag{2.27}$$

which is formally the same expression we used in Newtonian theory. However, the analogy is misleading, because eq. (2.27) takes into account not only the rest mass of the various fluid elements (as it happens in Newtonian theory), but also their internal energy and the overall gravitational potential energy [18, 19]. For this reason, M is often called the *total mass-energy* inside the radius R.

An implicit hypothesis we have been using so far is the so-called *partial decoupling of matter from gravity* [20]. It states that the equation of state can be derived by neglecting curvature effects. It is justified by the fact that the typical scale of interparticle separation is much smaller than the characteristic scale over which the metric changes appreciably.

2.3 Degenerate stars

So far we have been considered a completely generic fluid. In the following, we will focus on the particular case of *degenerate matter*, which provides a very good description of the internal structure of the most dense stars, i.e. white dwarfs and neutron stars. Degenerate matter is usually modeled as a cold Fermi gas, which we will briefly review in the following paragraph.

2.3.1 Degenerate Fermi gas

Let us consider a system of N non-interacting spin-1/2 fermions with mass m in the non-relativistic regime, distributed in a cubic box of volume $V = L^3$. The dynamics is described through the Hamiltonian [21]

$$H = \sum_{i=1}^{N} \frac{\boldsymbol{k}_i^2}{2m}\,, \tag{2.28}$$

where $\boldsymbol{k}_i$ is the momentum of the i-th particle. Since the Hamiltonian commutes with the momentum and spin operators, the single-electron wave function will be expressed as

$$\psi_{\boldsymbol{k},s}(\boldsymbol{x}) = \phi_{\boldsymbol{k}}(\boldsymbol{x})\chi_s\,, \tag{2.29}$$

that is a direct product between the Pauli spinor χ_s specifying the spin polarization, and the eigenfunction of the momentum operator $\phi_{\boldsymbol{k}}$, expressed as

$$\phi_{\boldsymbol{k}}(\boldsymbol{x}) = \sqrt{\frac{1}{V}}\, e^{i\,\boldsymbol{k}\cdot\boldsymbol{x}}\,. \tag{2.30}$$

The latter satisfies periodic boundary conditions,

$$\phi_{\boldsymbol{k}}(x_1, x_2, x_3) = \phi_{\boldsymbol{k}}(x_1 + n_1 L, x_2 + n_2 L, x_3 + n_3 L) \tag{2.31}$$

where $n_1, n_2, n_3 = 0, \pm 1, \pm 2, \cdots$. This implies that the momenta are quantized, i.e.

$$k_1 = \frac{2\pi n_1}{L}, \quad k_2 = \frac{2\pi n_2}{L}, \quad k_3 = \frac{2\pi n_3}{L}\,. \tag{2.32}$$

Thus, each single-particle quantum state is determined by the triplet of integers (n_1, n_2, n_3), corresponding to the energy

$$\epsilon_{\boldsymbol{k}} = \frac{\boldsymbol{k}^2}{2m} = \left(\frac{2\pi}{L}\right)^2 \frac{1}{2m}(n_1^2 + n_2^2 + n_3^2)\,. \tag{2.33}$$

The ground state of the system is then found by arranging all the particles in such a way that each energy level is occupied by a fermion pair (one for each of the two possible spin polarizations), starting from the lowest level (corresponding to $n_1 = n_2 = n_3 = 0$), up to the highest available level with N particles, whose energy is called *Fermi energy*, hereafter denoted as ϵ_{F}. Of course, the bigger N, the higher the energy of the last occupied state, i.e. ϵ_{F} increases with the number of particles N. The Fermi energy also defines a Fermi momentum through the expression $k_{\mathrm{F}} = \sqrt{2m\,\epsilon_{\mathrm{F}}}$.

The set of all quantum states naturally lives on a cubic lattice with unit lattice spacing. In this space, let us now consider a sphere of radius $\sqrt{n_1^2 + n_2^2 + n_3^2}$. The number of quantum states contained in this sphere is estimated as the volume of the sphere divided by the volume of a unit cell (which is one in our particular lattice), that is

$$\#\text{states} \approx \frac{4\pi}{3}\left(n_1^2 + n_2^2 + n_3^2\right)^{3/2} = \frac{V}{6\pi^2}\boldsymbol{k}^3\,, \tag{2.34}$$

where in the last step we used eq. (2.32). It is possible to show that the error made in writing the latter expression is subleading in the infinite particle limit $N \to \infty$.

As said, when the system is in the ground state, all the levels are populated up to the Fermi momentum k_F and each level hosts two particles due to spin degeneracy. Hence, the total number of particles is expressed as $N = V k_\mathrm{F}^3/3\pi^2$ and the fermion number density will be

$$n = \frac{N}{V} = \frac{k_\mathrm{F}^3}{3\pi^2}\,. \tag{2.35}$$

We have been considering so far the non-relativistic regime. However, eq. (2.35) is true also in the relativistic regime, since it is just based on counting quantum states up to a maximum level k_F. What changes is the relation between ϵ_F and k_F, which is generalized as follows

$$\epsilon_\mathrm{F} = \sqrt{k_\mathrm{F}^2 + m^2}\,. \tag{2.36}$$

The expressions for the total energy density ϵ and pressure p emerging at the macroscopic level, in a generic regime, are given by

$$\epsilon = \frac{2}{(2\pi)^3}\int_0^{k_\mathrm{F}} d^3k\,\sqrt{k^2+m^2}\,, \tag{2.37}$$

$$p = \frac{2}{(2\pi)^3}\int_0^{k_\mathrm{F}} d^3k\,\frac{k^2}{3\sqrt{k^2+m^2}}\,, \tag{2.38}$$

where these formulas are derived using standard kinetic theory [21]. Moreover, the total rest-mass density of the system is expressed as

$$\rho = m\,n\,. \tag{2.39}$$

It is also useful to define the total kinetic energy density ϵ_kin of the Fermi gas as

$$\epsilon_\mathrm{kin} = \epsilon - \rho = \frac{2}{(2\pi)^3}\int_0^{k_\mathrm{F}} d^3k\,\left(\sqrt{k^2+m^2} - m\right). \tag{2.40}$$

If the temperature is sufficiently low, the system will populate the ground state we just described. A gas of non-interacting fermions in its ground state is said to be *degenerate*. Practically, a gas becomes degenerate when the thermal energy k_BT (k_B is the Boltzmann constant) is much smaller than the Fermi energy k_F. It is therefore convenient to define a critical density n_c such that $\epsilon_\mathrm{F} = k_BT$, which corresponds to a critical Fermi momentum

$$k_\mathrm{F}^c = \sqrt{(k_BT)^2 + 2mk_BT}\,. \tag{2.41}$$

Thus, eq. (2.35) gives a critical number density $n_c = (k_\mathrm{F}^c)^3/3\pi^2$. We conclude that whenever $n \gg n_c$ the gas is degenerate, wherese if $n \ll n_c$ quantum effects are negligible.

As a concrete example, let us asses whether the neutron matter inside a neutron star is degenerate or not. The typical temperature of a neutron star is $T \sim 10^9\,\mathrm{K}$, whereas the mass of a single neutron is $m \sim 1\,\mathrm{GeV}$. Hence, eq. (2.41) leads to a critical density $\rho_c = m\,n_c \sim 10^{10}\,\mathrm{g/cm^3}$. On the other hand, the typical neutron star core density is $\rho \sim 10^{14}\,\mathrm{g/cm^3}$. Then, $\rho \gg \rho_c$ (or equivalently $n \gg n_c$), and therefore the neutron gas which is supporting the neutron star is in a degenerate phase.

2.3.2 Equation of state of degenerate matter

The integrals in eqs. (2.37) and (2.38) can be solved analytically. Then, one can in principle invert eq. (2.37) to get $k_{\rm F}$ as a function of ϵ, and plug this information into eq. (2.38). This simple argument shows that the equation of state describing a degenerate Fermi gas is barotropic, i.e. $p = p(\epsilon)$. Equivalently, $k_{\rm F}$ can be expressed in terms of the rest-mass density through eqs. (2.35) and (2.39), which leads to an equation of state of the form $p = p(\rho)$.

The functional relation between p and ϵ or ρ becomes particularly simple in two relevant regimes.

- *Non-relativistic regime.* If $p_{\rm F} \ll m$ the fermions are non-relativistic. To leading order, ϵ reduces to ρ, and the pressure can be expressed as

  $$p = K\,\rho^{\frac{5}{3}}\,, \tag{2.42}$$

  where

  $$K = \frac{1}{5}\left(\frac{3\pi^2}{m^4}\right)^{2/3}\,. \tag{2.43}$$

- *Ultra-relativistic regime.* If $p_{\rm F} \gg m$ the fermions are ultra-relativistic and every quantity can be expanded in the $m \to 0$ limit. In terms of the rest-mass density ρ, the pressure can be expressed as

  $$p = K'\,\rho^{\frac{4}{3}}\,, \tag{2.44}$$

  where

  $$K' = \frac{(3\pi^2)^{\frac{1}{3}}}{4\,m^{\frac{4}{3}}}\,. \tag{2.45}$$

  If we instead express the pressure using the energy density ϵ, we get an even simpler formula,

  $$p = \frac{1}{3}\epsilon\,. \tag{2.46}$$

  Technically speaking, to the leading order the rest-mass density ρ is zero and the only sensible expression is eq. (2.46). However, such an equation of state, when plugged into the TOV equations eqs. (2.22) and (2.23), does not give rise to configurations with finite radii. Physically, this means that it is not possible to gravitationally confine a gas of pure radiation into a regular star. A possible way to overcome this obstacle is to add a constant ϵ_0 to the energy density [22], i.e. $\epsilon = 3p + \epsilon_0$. This modifies eq. (2.46) in the following way

  $$p = \frac{1}{3}\epsilon - \frac{\epsilon_0}{3}\,. \tag{2.47}$$

In general, an equation of state with the functional form $p = K\rho^\gamma$, where K, γ are two independent parameters, is called *polytropic*.

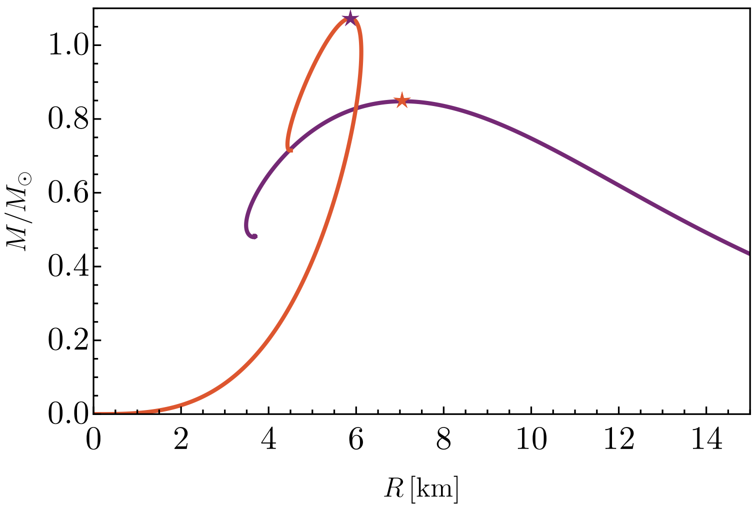

Figure 2.1. Mass-radius diagrams of a degenerate star with an equation of state eq. (2.42) (violet curve) and eq. (2.47) for $\epsilon_0 = 6 \times 10^{-3}\,\mathrm{GeV}^4$ (orange curve). We highlight with a star the position of the maximum-mass configurations.

2.3.3 Example of solutions

In this section we numerically solve eqs. (2.22) and (2.23) for different choices of the central pressure $p(r = 0) = p_c$, both in the case of non-relativistic and relativistic Fermi gas, i.e. we adopt, respectively, eq. (2.42) and eq. (2.47) as equation of state. In the latter case, we choose as a benchmark value $\epsilon_0 = 6 \times 10^{-3}\,\mathrm{GeV}^4$. We fix $m = 1\,\mathrm{GeV}$.

Once an equation of state is fixed, we thus generate a one-parameter space of solutions, each specified by a value of p_c, describing all the possible equilibrium configurations, each characterized by mass $M(p_c)$ and radius $R(p_c)$. It is often convenient to collect this information in a mass-radius diagram, as shown in fig. 2.1.

2.3.4 On the existence of a maximum mass

Inspecting fig. 2.1, we notice that each curve spans a range of masses bounded from above by the maximum possible value $M_\mathrm{c} \sim 1\,M_\odot$. In other words, the quantity M_c is the critical mass above which no equilibrium configuration can exist. This was first noticed by Chandrasekhar for white dwarfs [23] and then extended to neutron stars by some authors [24, 25]. Even if the exact value of M_c depends on the particular equation of state chosen, its existence arises in full generality, even for models of compact objects other than white dwarfs and neutron stars. Besides its phenomenological relevance, the critical mass has a remarkable theoretical importance, since it typically involves the microscopic parameters of the theory, and thus represents a bridge between the microphysics and the macroscopic world.

For concreteness, let us derive the critical mass for a family of stars supported by a relativistic degenerate Fermi gas. Integrating eq. (2.35), one finds the total number N of fermions in the system in a configuration of radius R as

$$N = \int_0^R 4\pi r^2 dr\, n = \frac{4}{9\pi}(R\, k_{\mathrm{F}})^3\,, \tag{2.48}$$

Then, the energy gas E_{gas} will be:

$$E_{\mathrm{gas}} = \int_0^R 4\pi r^2 dr\, \epsilon = \frac{1}{3\pi}(R\, k_{\mathrm{F}})^3 k_F \Rightarrow E_{\mathrm{gas}} \simeq \frac{N^{4/3}}{R}\,, \tag{2.49}$$

where in the last step we used eq. (2.48). On the other hand, the gravitational energy E_{g} inside the configuration is estimated as

$$E_{\mathrm{g}} \simeq -\frac{GM^2}{R}\,. \tag{2.50}$$

Thus, the total energy is

$$E = E_{\mathrm{gas}} + E_{\mathrm{g}} \simeq \frac{N^{4/3}}{R} - \frac{GM^2}{R}\,. \tag{2.51}$$

A bound configuration requires $E < 0$ and therefore $E = 0$ corresponds to the critical configuration beyond which no equilibrium is possible. The condition $E = 0$ yields

$$N^{4/3} = GM_{\mathrm{c}}^2\,. \tag{2.52}$$

If we estimate $N \sim M_{\mathrm{c}}/m$, we finally obtain

$$M_{\mathrm{c}} \sim \left(\frac{1}{G}\right)^{3/2} \frac{1}{m^2}\,. \tag{2.53}$$

For $m \sim 1\,\mathrm{GeV}$, we get $M_{\mathrm{c}} \sim M_{\odot}$, which is in agreement with fig. 2.1.

The maximum mass also defines a *turning point* in the mass-radius diagram. The latter plays a role when the stability of compact objects is investigated. Generically speaking, across a turning point the equilibrium configurations change behavior against radial perturbation (they become unstable if they were before stable and vice versa) [19].

2.4 Compactness bounds

In sec. 2.2.2 we introduced the compactness as

$$C = \frac{G\,M}{R}\,. \tag{2.54}$$

It is a fundamental parameter to characterize the properties of a compact object. For static and spherically symmetric configurations,

- if $C > 1/6 \approx 0.17$ then the spacetime features an ISCO (acronym for "innermost stable circular orbit"), which has an important role in the dynamics of accretion disks [26];

- if $C > 1/3 \approx 0.33$ the spacetime shows a light ring, the only circular orbit for massless test particle (which is however unstable); it has a crucial importance in describing how the compact object appears when illuminated by light [26] and it is responsible for the emission of the so-called "echoes" [26] (see sec. 6.3.2).

The maximum possible value for the compactness C is $1/2$, corresponding to a black hole. Thus, any *regular* (i.e. without curvature singularities) compact object will necessarily satisfy $C < 1/2$. However, there are reasons to believe that, within general relativity, there are no regular static configurations made out of physically reasonable matter whose compactness is arbitrarily close to the black hole limit [27]. A classical result that goes in this direction is Buchdahl's theorem [28, 19] which states that the maximum compactness of a self-gravitating object is $C < 4/9 \approx 0.44$. The theorem is based on the assumptions that the configuration is static and spherically symmetric, the fluid is perfect (see eq. (2.20)) and

$$\epsilon \geq 0\,, \qquad p \geq 0\,, \qquad \frac{d\epsilon}{dr} \leq 0\,, \tag{2.55}$$

where ϵ and p are, respectively, the energy density and the pressure. However, if we further require radial stability of the equilibrium configurations and impose that the sound speed of the fluid should not be greater than the speed of light, i.e.

$$c_s = \sqrt{\frac{dp}{d\epsilon}} \leq 1 \tag{2.56}$$

we recover the so-called *causal Buchdahl bound* [22, 11, 27] $C < 0.354$, which is smaller than $4/9$.

Relaxing some of the previous assumptions (e.g. considering theories beyond general relativity or considering exotic matter, for which eq. (2.55) does not apply) provides a way to circumvent Buchdahl's theorem. This highlights the relevance of the compactness C in parametrizing new physic effects [26].

2.5 Exotic compact objects

The only known examples of compact objects are black holes and neutron stars. As discussed in sec. 2.3.1, the latter are roughly described as a degenerate gas of neutrons bound by gravitational interaction. Diverse experimental observations constrain dark matter to act on macroscopic scales as a cold, feebly-interacting, stable fluid [5]. However, the actual microscopic degrees of freedom which constitute dark matter are not known. A viable possibility is that dark matter is composed of a new stable particle (see e.g. refs [29, 30]). It is conceivable that these particles clump together to form macroscopic self-gravitating objects, as happens for neutron stars. Such *exotic compact objects* (ECOs) would naturally be decoupled (or only feebly interacting) with other Standard Model particles. Nonetheless, they can still leave gravitational signatures, particularly in gravitational waves emitted by binary systems of two ECOs or an ECO and a neutron star/black hole [31]. This already shows the extraordinary possibilities opened after the discovery of gravitational waves.

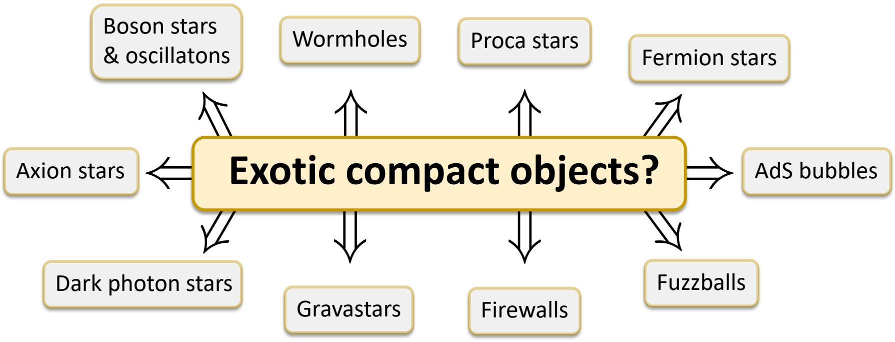

Figure 2.2. The (non-exhaustive) ECO atlas.

Even if we think on purely theoretical grounds, forgetting about the dark matter consideration, it is a rather general fact that as soon as new fields are added to the Standard Model, configurations describing ECOs arise. A non-exhaustive list of proposed models are boson stars and oscillatons [32], fermion stars [33], axion stars [34], dark photon stars [35], gravastars [36], AdS bubbles [37], wormholes [38], firewalls [39], fuzzballs [40, 41]. A conceptual map useful for navigating among the various models is shown in fig. 2.2.

In general, for an ECO to be considered a physically viable object, a few requirements should be fulfilled [42, 43]:

- to be described within a sound physical theory (such as local and causal theories with an underlying Lagrangian description, possibly motivated in some BSM scenario);
- to be stable against small perturbations and long-lived;
- to have a dynamical formation mechanism.

As suggested by ref. [26], it is evocative to make a parallel with the timeline of particle discoveries. As shown in fig. 2.3, after the detection of the electron in 1897, the number of particles discovered increased slowly for roughly two decades. From the 1920s, the slope of the line underwent a sharp increase, culminating in the 1980s with the discovery of the W and Z bosons. Then, a second period of slow increase settled down, which lasts until today.

From this standpoint, BHs and neutron stars could be just two examples of a large zoo of possible compact objects, yet to be discovered. The first GW detection of a BH binary happened in 2015 [7], while the first NS binary was detected in 2017 [44]. It is conceivable that in a few decades, thanks to the advance in GW astronomy and the development of a new generation of interferometers, new species in the zoo of compact objects will be unveiled, as it happened in the timeline of particle discoveries.

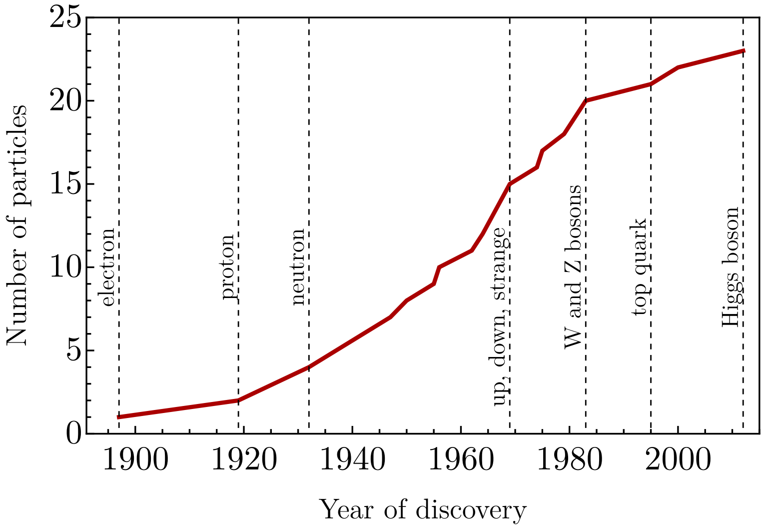

Figure 2.3. Timeline of particle discoveries.

2.5.1 Boson stars and oscillatons

One of the simplest examples of an ECO is boson stars. These are gravitational bound states supported by a cold gas of bosons, unlike the case of degenerate stars discussed in section 2.3, which are instead supported by a gas of fermions. Due to their intrinsic properties, a large fraction N of bosons occupy the lowest quantum energy level, giving rise to a macroscopic coherent state. The system is then conveniently described through a field $\Psi(x)$ of integer spin. The large occupancy number ensures that quantum fluctuations $\delta\Psi$ are small, i.e.

$$\frac{\delta\Psi}{\Psi} \to 0 \quad \text{as} \quad N \to \infty \,. \tag{2.57}$$

This allows us to study boson stars within classical field theory.

The simplest scenario is that of a free complex scalar field ϕ decoupled from the Standard Model, and described by the action

$$S = \int d^4x \sqrt{-g}\left(\frac{R}{16\pi G} - \frac{1}{2}\partial^\mu\phi^*\partial_\mu\phi - \frac{m^2}{2}\phi^*\phi\right) . \tag{2.58}$$

This theory admits static and spherically symmetric geometries, dubbed *mini boson stars* [45]. The critical mass M_c for these configurations is

$$M_c \sim \left(\frac{1}{G}\right)\frac{1}{m} \,, \tag{2.59}$$

where m is the mass of the scalar field ϕ. Current gravitational wave interferometers can probe ECOs that have roughly the mass of the Sun. Eq. (2.59) then sets the relevant scale for the boson mass m to be $\sim 10^{-10}$ eV, which is obtained in the case of QCD axion or axion-like particles. This simple computation explicitly shows how

GW detection can contribute to the search for new physics in a region completely inaccessible by current particle accelerators.

Similar solutions exist also if we include scalar self-interactions, for example adding a $\lambda|\phi|^4$ term [46] or higher dimensional operators [8]. In general, the critical mass M_c will depend on the precise form of the scalar potential $U(\phi)$, together with the maximum compactness reached by the configurations. As a rule of thumb, the stronger the self-interactions the higher the maximum compactness and mass of a stable boson star. Analogous static and spherically symmetric geometries are also formed out of massive vector fields[47, 48].

In some peculiar models, the solutions exist even without gravity. These are known as *Q-balls* [49]. They describe spatially localized clumps of particles stabilized just by their self-interaction. Crucially, they have the same properties of the ordinary vacuum as spatial infinity. For this reason, they are classified as *non-topological solitons* (NTSs), at variance with topological solitons, such as monopoles and strings. The relativistic generalization of Q-balls, where the effects of gravity are included, are called *solitonic boson stars* [8, 11].

When the scalar field in eq. (2.58) is real, no-go theorems [50, 51] prevent the existence of static geometries as long as $U(\phi) \geq 0$. Thus, one is forced to relax some assumptions. For example, one might consider a negative scalar potential in a region. This however leads to a violation of the weak energy condition [52]. Alternatively, one can look for time-dependent geometries. In this case, one finds solutions dubbed *oscillatons*, which however decay with time (although the lifetime can be very long) [32].

Both boson stars and oscillatons possess robust dynamical formation mechanicsms [53, 54] and are therefore natural outcomes of the gravitational collapse. Moreover, both are shown to be radially stable [55]. Therefore, they are sound and well-motivated examples of ECOs.

Chapter 3

Fermion soliton stars

Summary

In this chapter, we show that a real scalar field coupled to a fermion via a Yukawa term can evade no-go theorems preventing solitonic solutions (see Sec. 2.5). We study this model within General Relativity without approximations, finding static and spherically symmetric solutions that describe fermion soliton stars. The Yukawa coupling provides an effective mass for the fermion, which is key to the existence of self-gravitating relativistic solutions. We systematically study this novel family of solutions and present their mass-radius diagram and maximum compactness, which is close to (but smaller than) that of the corresponding Schwarzschild photon sphere. Finally, we discuss the ranges of the parameters of the fundamental theory in which the latter might have interesting astrophysical implications, including compact (sub)solar and supermassive fermion soliton stars for a standard gas of degenerate neutrons and electrons, respectively.

3.1 Setup

We consider a theory in which Einstein gravity is minimally coupled to a real scalar field ϕ and a fermion field ψ. The action can be written as [13]

$$S = \int \mathrm{d}^4x\sqrt{-g}\Big[\frac{R}{16\pi G} - \frac{1}{2}\partial^\mu\phi\partial_\mu\phi - U(\phi) + \bar{\psi}(i\gamma^\mu D_\mu - m_f)\psi + f\phi\bar{\psi}\psi\Big], \quad (3.1)$$

where the scalar potential is

$$U(\phi) = \frac{1}{2}\mu^2\phi^2\Big(1 - \frac{\phi}{\phi_0}\Big)^2, \quad (3.2)$$

and features two degenerate minima at $\phi = 0$ and $\phi = \phi_0$. The constant μ (resp. m_f) is the mass of the scalar (resp. fermion). The Yukawa interaction[1] is controlled by the coupling f. The fermionic field has a $U(1)$ global symmetry which ensures the conservation of the fermion number N. Also, we point out that, in the absence of gravity, the Lagrangian in eq. (3.1) describes a renormalizable field theory; this is

---

[1] See also ref. [56] for a recent work on a condensed dark matter in a model with a Yukawa coupling between a fermion and a scalar particle.

in contrast to the widely used model describing solitonic boson stars [8, 9, 10, 11] in which the scalar potential is non-renormalizable and field values should not exceed the limit of validity of the corresponding effective field theory. The covariant derivative D_μ in eq. (3.1) takes into account the spin connection of the fermionic field.

From the quadratic terms in the fermion Lagrangian, it is useful to define an effective mass,

$$m_{\rm eff} = m_f - f\phi. \tag{3.3}$$

We will focus on scenarios in which the fermion becomes effectively massless (i.e. $m_{\rm eff} = 0$) when the scalar field sits on the second degenerate vacuum, $\phi = \phi_0$. This condition implies fixing

$$f = \frac{m_f}{\phi_0}. \tag{3.4}$$

As we shall discuss, we are mostly interested in configurations where the scalar field makes a transition between the false[2] vacuum ($\phi \approx \phi_0$) to the true vacuum ($\phi \approx 0$).[3]

3.1.1 Thomas-Fermi approximation

The description of a fermionic field in eq. (3.1) requires treating the quantization of spin-1/2 particles in curved spacetime. In particular, one should deal with the problem of finding the ground state of an ensemble of N fermions in curved spacetime (see e.g. [59, 60]). However, in the macroscopic limit $N \gg 1$, it is convenient to adopt a mean-field approach, which in this context is called the Thomas-Fermi approximation[4] . The latter relies on the assumption that the gravitational and scalar fields are slowly varying functions with respect to the fermion dynamics. Consequently, they do not interact directly with the (microscopic) fermionic field ψ, but with average macroscopic quantities. In practice, one can divide the entire three-space into small domains that are much larger than the de Broglie wavelength of the typical fermion, but sufficiently small that the gravitational and scalar fields are approximately constant inside each domain. Then, every domain is filled with a degenerate (i.e. the temperature is much smaller than the chemical potential) Fermi gas (see sec. 2.3.1), in such a way that the Fermi distribution is approximated by a step function, $n_k = \theta(k_{\rm F} - k)$, where $k_{\rm F}(x^\mu)$ is the Fermi momentum observed in the appropriate local frame.

The energy density of the fermion gas reads

$$W = \frac{2}{(2\pi)^3}\int_0^{k_{\rm F}} {\rm d}^3k\, \epsilon_k, \tag{3.5}$$

---

[2] Although the minima at $\phi = 0$ and $\phi = \phi_0$ are degenerate, we shall call them true and false vacuum, respectively, having in mind the generalization in which the potential $U(\phi)$ can be nondegenerate, i.e. $U(\phi_0) \neq U(0)$ (see Fig. 3.1).

[3] Recently, ref. [57] studied a related model in which dark fermions are trapped inside the false vacuum during a first-order cosmological phase transition, subsequently forming compact macroscopic "Fermi-balls", which are dark matter candidates and can collapse to primordial black holes [58].

[4] We point the interested reader to Appendix A of ref. [13] for a complete derivation of the Thomas-Fermi approximation in curved spacetime, while here we summarise the main properties.

where $\epsilon_k = \sqrt{k^2 + m_{\text{eff}}^2}$. Notice that $W = W(x^\mu)$ through the spacetime dependence of k_{F} and m_{eff}. In an analogous way, we obtain the fermion gas pressure P and the scalar density $S = \langle \bar{\psi}\psi \rangle$ as

$$P = \frac{2}{(2\pi)^3} \int_0^{k_{\text{F}}} \mathrm{d}^3k \, \frac{k^2}{3\epsilon_k}, \tag{3.6}$$

$$S = \frac{2}{(2\pi)^3} \int_0^{k_{\text{F}}} \mathrm{d}^3k \, \frac{m_{\text{eff}}}{\epsilon_k}. \tag{3.7}$$

It is easy to show that these quantities satisfy the identity

$$W - 3P = m_{\text{eff}} S. \tag{3.8}$$

In the Thomas-Fermi approximation, the fermions enter Einstein's equations as a perfect fluid characterized by an energy-momentum tensor of the form

$$T^{[f]}_{\mu\nu} = (W + P) u_\mu u_\nu + P g_{\mu\nu}, \tag{3.9}$$

while they also enter the scalar field equation through the scalar density S. Indeed, by varying the action in eq. (3.1) with respect to ϕ, we obtain a source term of the form $\approx f\bar{\psi}\psi$. Within the Thomas-Fermi approximation, this becomes

$$f\bar{\psi}\psi \to f\langle\bar{\psi}\psi\rangle \equiv fS, \tag{3.10}$$

which is consistent with the fact that, in the fluid description, the scalar field equation couples to fermions through a term proportional to the trace $(T^{[f]})^\mu_\mu = -W + 3P$.

Equations of motion

It is now possible to write down the equations of motion for our theory in covariant form

$$\begin{gathered} G_{\mu\nu} = 8\pi G \, T_{\mu\nu}, \\ \Box\phi - \frac{\partial U}{\partial \phi} + fS = 0, \end{gathered} \tag{3.11}$$

where

$$T_{\mu\nu} = -2\Big(\frac{\partial \mathcal{L}_\phi}{\partial g^{\mu\nu}} - \frac{1}{2} g_{\mu\nu} \mathcal{L}_\phi\Big) + T^{[f]}_{\mu\nu}, \tag{3.12}$$

in which $\mathcal{L}_\phi$ is the Lagrangian density of the scalar field. In order to close the system, we need an equation describing the behavior of k_{F}. This is obtained by minimizing the energy of the fermion gas at a fixed number of fermions [13].

From now on, for simplicity, we will consider spherically symmetric equilibrium configurations, whose background metric can be expressed as

$$\mathrm{d}s^2 = -e^{2u(\rho)}\mathrm{d}t^2 + e^{2v(\rho)}\mathrm{d}\rho^2 + \rho^2(\mathrm{d}\theta^2 + \sin^2\theta \mathrm{d}\varphi^2), \tag{3.13}$$

in terms of two real metric functions $u(\rho)$ and $v(\rho)$ (at variance with the previous chapter, hereafter we denote the radial coordinate as ρ). Furthermore, we will assume that the scalar field in its equilibrium configuration is also static and spherically symmetric, $\phi(t, \rho, \theta, \varphi) = \phi(\rho)$. Being the spacetime static and spherically symmetric, $k_{\text{F}} = k_{\text{F}}(\rho)$ can only be a function of the radial coordinate.

Fermi momentum equation

In the Thomas-Fermi approximation, the fermion gas energy can be written as [13]

$$E_f = 4\pi \int \mathrm{d}\rho\, \rho^2\, e^{u(\rho)+v(\rho)}\, W, \tag{3.14}$$

while the number of fermions is

$$N = \frac{4}{3\pi} \int \mathrm{d}\rho\, \rho^2 e^{v(\rho)} k_\mathrm{F}^3(\rho). \tag{3.15}$$

To enforce a constant number of fermions, we introduce the Lagrangian multiplier ω_F and define the functional

$$E'_f[k_\mathrm{F}] = E_f[k_\mathrm{F}] - \omega_\mathrm{F}\Big(N[k_\mathrm{F}] - N_\mathrm{fixed}\Big), \tag{3.16}$$

which is minimized by imposing

$$\frac{\delta E'_f[k_\mathrm{F}]}{\delta k_\mathrm{F}(\rho)} = 0. \tag{3.17}$$

This directly brings us to the condition

$$\epsilon_\mathrm{F} = e^{-u}\omega_\mathrm{F}, \tag{3.18}$$

where $\epsilon_\mathrm{F} = \epsilon_{k_\mathrm{F}}$ is the Fermi energy. Thus, ω_F coincides with the Fermi energy in flat spacetime while it acquires a redshift factor otherwise. Since $\epsilon_F = \sqrt{k_F^2 + m_\mathrm{eff}^2}$, eq. (3.18) in turn gives

$$k_\mathrm{F}^2(\rho) = \omega_\mathrm{F}^2 e^{-2u(\rho)} - (m_f - f\phi(\rho))^2\,. \tag{3.19}$$

3.1.2 Dimensionless equations of motion and boundary conditions

In order to simplify the numerical integrations, as well as physical intuition, it is convenient to write the field equations in terms of dimensionless quantities. To this end, we define

$$x = \frac{k_\mathrm{F}}{m_f}, \qquad y = \frac{\phi}{\phi_0}, \qquad r = \rho\mu. \tag{3.20}$$

Therefore, the potential and kinetic terms become

$$\begin{aligned} U &= \mu^2\phi_0^2 \left[\frac{1}{2}y^2(1-y)^2\right] \equiv \mu^2\phi_0^2\tilde{U}(y), \\ V &= \mu^2\phi_0^2 \left[\frac{1}{2}e^{-2v(r)}(\partial_r y)^2\right] \equiv \mu^2\phi_0^2\tilde{V}(y), \end{aligned} \tag{3.21}$$

while Eqs. (3.5)-(3.7) can be computed analytically as

$$W = \frac{m_\mathrm{eff}^4}{8\pi^2}\left[s\sqrt{1+s^2}(1+2s^2) - \log\Big(s+\sqrt{s^2+1}\Big)\right] \equiv m_f^4\tilde{W}(x,y), \tag{3.22a}$$

$$P = \frac{m_\mathrm{eff}^4}{8\pi^2}\left[s\left(\frac{2}{3}s^2-1\right)\sqrt{1+s^2} + \log\Big(s+\sqrt{s^2+1}\Big)\right] \equiv m_f^4\tilde{P}(x,y), \tag{3.22b}$$

$$S = \frac{m_\mathrm{eff}^3}{2\pi^2}\left[s\sqrt{1+s^2} - \log\Big(s+\sqrt{s^2+1}\Big)\right] \equiv m_f^3\tilde{S}(x,y), \tag{3.22c}$$

where $\tilde{W}, \tilde{P}, \tilde{S}$ are dimensionless quantities and we introduced $s \equiv x/(1-y)$ for convenience. Remarkably, these expressions are the same as in the standard case of a minimally coupled degenerate gas with the substitution $m_f \to m_{\rm eff}$.

As we shall discuss in Appendix A, this property will be important when comparing this model to a scalar-tensor theory. Note that the massless limit, $m_{\rm eff} \to 0$, should be taken carefully as not all the dependence on $m_{\rm eff}$ is expressed in the dimensional prefactor. By performing the first integrals in Eqs. (3.22a)-(3.22c) in the $m_{\rm eff} \to 0$ limit, we obtain $W = P/3$, as expected for an ultrarelativistic degenerate gas.

It is convenient to further introduce the dimensionless combination of parameters

$$\Lambda = \frac{\sqrt{8\pi}\phi_0}{m_p}, \qquad \eta = \frac{m_f}{\mu^{1/2}\phi_0^{1/2}}. \tag{3.23}$$

Finally, the field equations (i.e. the Einstein-Klein-Gordon equations with the addition of the Fermi momentum equation) take the compact form

$$\begin{aligned} & e^{-2v} - 1 - 2e^{-2v} r\partial_r v = -\Lambda^2 r^2 \left[\eta^4 \tilde{W} + \tilde{U} + \tilde{V}\right], \\ & e^{-2v} - 1 + 2e^{-2v} r\partial_r u = \Lambda^2 r^2 \left[\eta^4 \tilde{P} - \tilde{U} + \tilde{V}\ \right], \\ & e^{-2v}\left[\partial_r^2 y + \left(\partial_r u - \partial_r v + \frac{2}{r}\right)\partial_r y\right] = \frac{\partial \tilde{U}}{\partial y} - \eta^4 \tilde{S}, \\ & x^2 = \tilde{\omega}_{\rm F}^2 e^{-2u(r)} - (1-y)^2, \end{aligned} \tag{3.24}$$

where $\tilde{U}$, $\tilde{V}$, $\tilde{P}$, $\tilde{W}$, and $\tilde{S}$ depend on x, y, and r, and we also introduced $\tilde{\omega}_{\rm F} = \omega_{\rm F}/m_f$. Static and spherically symmetric configurations in the model (3.1) are solutions to the above system of ordinary differential equations. For clarity, we summarize the relevant parameters in Table 3.1.

Absence of $\phi = \text{const}$ solutions

Note that, because $U = 0 = dU/d\phi$ in both degenerate vacua, it is natural to first check what happens when $\phi = \phi_0 = \text{const}$ or if $\phi = 0$. The former case (i.e., $y(\rho) = 1$) is an exact solution of the scalar equation and reduces Einstein's equations to those of gravity coupled to a degenerate gas of massless (since $m_{\rm eff}(\phi_0) = 0$) fermions. In this case, self-gravitating solutions do not have a finite radius [61]. On the other hand, due to the Yukawa coupling, in the presence of a fermion gas $\phi = 0$ is not a solution to the scalar field equation.

Thus, self-gravitating solutions to this model must have a nonvanishing scalar-field profile. In particular, we will search for solutions that (approximately) interpolate between these two vacuum states.

Boundary conditions at $\rho = 0$

Regularity at the center of the star ($\rho = 0$) imposes the following boundary conditions

$$\begin{aligned} & v(r=0) = 0, \qquad && u(r=0) = 0, \\ & y(r=0) = 1 - \epsilon, \qquad && \partial_r y(0) = 0, \\ & \tilde{P}(r=0) = \tilde{P}_c, \end{aligned} \tag{3.25}$$

Table 3.1. List of the model parameters, the fermion soliton star parameters, and the dimensionless quantities adopted to express the system of equations in compact form. Due to the condition in eq. (3.4), in our case only three model parameters are independent.

Model parameters	
μ	Scalar field mass
ϕ_0	VEV of the false vacuum
m_f	Fermion mass
f	Yukawa coupling
Solution parameters (boundary conditions)	
P_c	Fermion central pressure
$\epsilon = 1 - \phi/\phi_0$	Central scalar field displacement
Dimensionless parameters/variables	
$\Lambda = \sqrt{8\pi}\phi_0/m_p$	Dimensionless VEV of the false vacuum
$\eta = m_f/\sqrt{\mu\phi_0}$	Scale ratio
$x = k_{\mathrm{F}}/m_f$	Dimensionless Fermi momentum
$y = \phi/\phi_0$	Dimensionless scalar field
$r = \rho\mu$	Rescaled radius

where $\epsilon > 0$ will be fixed numerically through a shooting procedure in order to obtain asymptotic flatness.

The central value of the pressure $\tilde{P}_c$ is fixed in terms of $\tilde{\omega}_{\mathrm{F}}$ and ϵ through the relation

$$\tilde{P}_c = \frac{1}{24\pi^2}\left(\tilde{\omega}_{\mathrm{F}}\sqrt{\tilde{\omega}_{\mathrm{F}}^2 - \epsilon^2}(2\tilde{\omega}_{\mathrm{F}}^2 - 5\epsilon^2) + 3\epsilon^4 \operatorname{arctanh}\sqrt{1 - \frac{\epsilon^2}{\tilde{\omega}_{\mathrm{F}}^2}}\right), \tag{3.26}$$

obtained computing eq. (3.22b) in $\rho = 0$. In practice, in a large region of the parameter space one obtains $\epsilon \ll 1$. In this limit, eq. (3.26) reduces to $\tilde{P}_c \approx \tilde{\omega}_{\mathrm{F}}^4/12\pi^2$.

Finally, since a shift $u(\rho) \to u(\rho) + \mathrm{const}$ in eq. (3.24) merely corresponds to a shift of the fermionic central pressure, we have imposed $u(\rho = 0) = 0$ without loss of generality.

Definitions of mass, radius, and compactness

We define the mass of the object as

$$M = \frac{m(\rho \to +\infty)}{G}, \tag{3.27}$$

where the function $m(\rho)$ is related to the metric coefficient $v(\rho)$ by $e^{-2v(\rho)} = 1 - 2m(\rho)/\rho$, and can be interpreted as the mass-energy enclosed within the radius

ρ. In terms of the dimensionless variables introduced in eq. (3.20), it is convenient to define $\tilde{m}(r) = \mu m(\rho)$. Thus, one obtains

$$\frac{\mu M}{m_p^2} = \tilde{m}(r). \tag{3.28}$$

Notice that, in the asymptotic limit $r \to \infty$, eq. (3.28) becomes independent of the radius.

Typically, the radius of a star is defined as the value of the radial coordinate at the point where pressure drops to zero. As we shall discuss, in our case the fermion soliton stars will be characterized by a lack of a sharp boundary. Analogously to the case of boson stars [54], one can define an effective radius R within which 99% of the total mass is contained. (As later discussed, we shall also define the location R_f where only the pressure of the fermion gas vanishes.) Finally, we can define the compactness of the star as GM/R.

3.2 Some preliminary theoretical considerations

Before solving the full set of field equations numerically, in this section we provide some theoretical considerations that might be useful to get a physical intuition of the model.

3.2.1 On the crucial role of fermions for the existence of solitonic stars

Classical mechanics analogy

In order to understand why the presence of fermions in this theory plays a crucial role for the existence of stationary solutions, it is useful to study a classical mechanics analogy for the dynamics of the scalar field [49].

For the moment we consider flat spacetime. Furthermore, we start by ignoring the fermions (we will relax this assumption later on). The set of Eqs. (3.24) drastically simplifies to a single field equation

$$\partial_\rho^2 \phi + \frac{2}{\rho}\partial_\rho \phi - \frac{\partial U}{\partial \phi} = 0. \tag{3.29}$$

To make the notation more evocative of a one-dimensional mechanical system, we rename

$$\rho \to t, \quad \phi(\rho) \to \phi(t), \quad \hat{U} := -U, \tag{3.30}$$

in such a way that the equation of motion becomes

$$\phi''(t) = -\frac{\partial \hat{U}}{\partial \phi} - \frac{2}{t}\phi'(t), \tag{3.31}$$

which describes the one-dimensional motion of a particle with coordinate $\phi(t)$ in the presence of an *inverted* potential, $\hat{U}$, and a velocity-dependent dissipative force, $-(2/t)\phi'(t)$. Within this analogy, the boundary (or initial) conditions (3.25) simply become

$$\phi(t=0) = \phi_0 - \delta\phi, \quad \phi'(t=0) = 0, \tag{3.32}$$

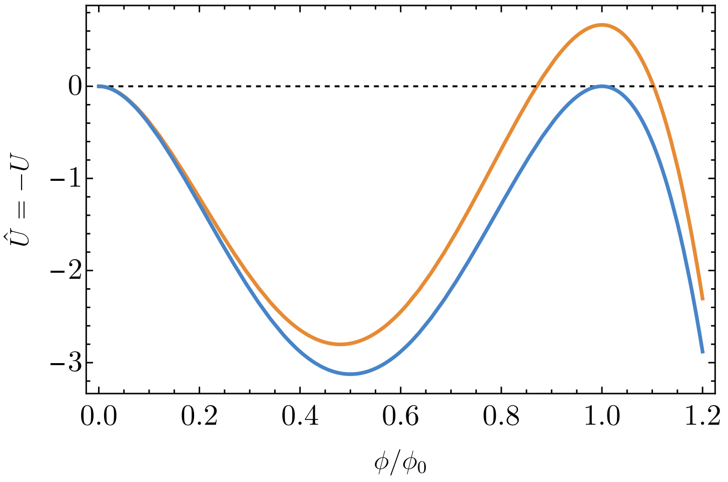

Figure 3.1. Inverted potential with degeneracy (blue line, our case) and without degeneracy between vacua (orange line). The scalar field is shown in units of the vev ϕ_0.

where ϕ_0 is the position of the false vacuum and $\delta\phi = \epsilon\phi_0$. As we impose zero velocity at $t = 0$, the initial energy is $E(0) = \hat{U}(\phi_0 - \delta\phi)$. The energy $E(t)$ of the particle at a time t is obtained by subtracting the work done by the friction:

$$E(t) - E(0) = L(t), \tag{3.33}$$

where

$$L(t) = -2\int_0^t \mathrm{d}t' \, \frac{\dot{\phi}^2(t')}{t'}. \tag{3.34}$$

Note that, owing to the initial conditions, this integral is regular at $t = 0$. On the other hand, the existence of a solution with asymptotically zero energy requires the particle to arrive with zero velocity at $\phi = 0$ for $t \to +\infty$. Therefore, we impose $E(t \to \infty) = 0$. As the total energy loss due to friction is $L(t \to \infty)$, the latter condition means

$$E(0) = -L(t \to \infty) \tag{3.35}$$

that is

$$\hat{U}(\phi_0 - \delta\phi) = 2\int_0^\infty \mathrm{d}t' \, \frac{\dot{\phi}^2(t')}{t'} \, . \tag{3.36}$$

This equation can be interpreted as an equation for $\delta\phi$ in order to allow for the existence of a "bounce" solution[5]. One can demonstrate the existence of such a solution heuristically. Let us first consider a slightly modified version of the inverted potential without degeneracy (orange plot in Fig. 3.1). Obviously, if the motion starts exactly at ϕ_0 with zero velocity, the particle would remain at rest. However, if we start on the left of the maximum the particle will roll down, bounce, and

---

[5] A bounce solution is the one reaching asymptotically the true vacuum with zero energy, after having "bounced" at the minimum of the inverted potential.

eventually climb the leftmost hill shown in Fig. 3.1. Now, if the dynamics starts *too far from* ϕ_0 (still on the left of the maximum), with zero initial velocity it might not have enough energy to reach the zero-energy point at $\phi = 0$. Similarly, if the dynamics starts *too close* to ϕ_0, the particle might reach $\phi = 0$ with positive energy and *overcome* the hill rolling up to $\phi \to -\infty$. By continuity, there must exist a unique point such that the total energy loss due to friction compensates the initial gap of energy with respect to the energy of $\phi = 0$.

However, by applying the same argument to our *degenerate* case (blue curve in Fig. 3.1), it is easy to see that there is no solution to eq. (3.36) [6]. This is because the energy loss due to friction is nonzero, so the particle will never reach $\phi = 0$ and is doomed to roll back in the potential eventually oscillating around the minimum of $\hat{U}$. This shows that, in the degenerate case considered in this work, a simple scalar model does not allow for bounce solutions in flat spacetime.

If we now reintroduce fermions in the theory, the scalar field equation reads (still in flat spacetime)

$$\phi''(t) = -\frac{\partial \hat{U}}{\partial \phi} - \frac{2}{t}\phi'(t) - fS. \tag{3.37}$$

Since $S \geq 0$, the fermions act with a force pushing our particle toward the origin, potentially giving the right kick to allow the particle to reach $\phi = 0$ asymptotically. As we shall see, this also requires $S = 0$ (i.e., no fermions) around the origin, for the particle to reach a stationary configuration at $\phi = 0$.

This simple analogy shows how the presence of the fermions is fundamental as it allows the solution to exist. In the following section, we will show how this is realized in the full theory which includes gravitational effects. Furthermore, we will show that, in certain regions of the parameter space, relativistic effects are in fact crucial for the existence of the solution, since the latter requires a minimum fermionic pressure to exist.

Evading the no-go theorem for solitons

The above conclusions, deduced from our simple heuristic picture, hold in the context of General Relativity as well. Indeed, without fermions in the system of Eqs. (3.24), and since our potential (3.2) is nonnegative, a general theorem proves that no axially symmetric and stationary solitons (that is asymptotically flat, localized, and everywhere regular solutions) can exist [50, 51].

However, the presence of fermions evades one of the hypotheses of the theorem. As we will show, in this case stationary solitons generically exist also for a *real* scalar field (at variance with the case of boson stars, which require complex scalars) and for a wide choice of parameters.

3.2.2 Scaling of the physical quantities in the $\mu R \gg 1$ regime

Assuming $\mu R \gg 1$, it is possible to derive an analytical scaling for various physical quantities, as originally derived in ref. [62] and similar in spirit to Landau's original computation for ordinary neutron stars (see, e.g., [61]).

---

[6] At least if we look for a solution in which the scalar field does the transition at a finite time.

It is instructive to consider (3.1) in the absence of gravity. As already pointed out, the theory has a conserved (additive) quantum number N, brought by the fermion field ψ. Being $\mu R \gg 1$, the real scalar field solution is well approximated by a stiff Fermi function [13],[62]

$$\phi(\rho) \approx \frac{\phi_0}{1 + e^{\mu(\rho - R)}}. \tag{3.38}$$

The definition of $k_{\rm F}$ is nothing but eq. (3.19) with $u = 0$ (since we work in the absence of gravity)

$$k_{\rm F}^2(\rho) = \omega_{\rm F}^2 - (m_f - f\phi(\rho))^2 \,. \tag{3.39}$$

Because of eq. (3.38), the Fermi momentum is nearly fixed to the constant value $\omega_{\rm F}$ for $\rho \lesssim R$, and for $\rho \approx R$ it goes to zero stiffly. Therefore, the field ψ is approximately confined within the sphere of radius R. We assume that the quanta of ψ are noninteracting, massless, and described by Fermi statistics at zero temperature. Thus, we obtain the standard relation for the particle density

$$n = \frac{\#\text{particles}}{\text{unit.volume}} = \frac{2}{8\pi^3} \int_0^{k_{\rm F}} 4\pi k^2 {\rm d}k = \frac{\omega_{\rm F}^3}{3\pi^2}. \tag{3.40}$$

Since $k_{\rm F} \simeq \omega_{\rm F} = \text{const}$, the total number of particles is

$$N = n \int_0^R 4\pi\rho^2 {\rm d}\rho = \frac{4}{9\pi}(R\omega_{\rm F})^3. \tag{3.41}$$

The fermion energy is

$$E_f = \int_0^R 4\pi\rho^2 {\rm d}\rho \, W = (3\pi)^{1/3} \Big(\frac{3}{4}N\Big)^{4/3} \frac{1}{R}, \tag{3.42}$$

where

$$W = \frac{\text{energy}}{\text{unit.volume}} = \frac{2}{8\pi^3} \int_0^{k_{\rm F}} 4\pi k^2 {\rm d}k \cdot k = \frac{\omega_{\rm F}^4}{4\pi^2}. \tag{3.43}$$

The energy associated with the scalar field ϕ is instead

$$E_s = \int_0^R 4\pi\rho^2 d\rho \, (U + V) \simeq \Big(\frac{1}{6}\mu\phi_0^2\Big) 4\pi R^2 \,, \tag{3.44}$$

where we have used the fact that

$$\frac{12}{\mu\phi_0^2} U \simeq \frac{12}{\mu\phi_0^2} V \simeq \delta(\rho - R) \,, \tag{3.45}$$

which can be shown using eq. (3.38) and $\mu R \gg 1$.

The total energy of our configuration is

$$E = E_f + E_s, \tag{3.46}$$

while the radius can be found by imposing $\partial E / \partial R = 0$, yielding

$$R = \Big[\frac{3}{4\pi}(3\pi)^{1/3}\Big(\frac{3}{4}N\Big)^{4/3}\Big]^{1/3} \Big(\frac{1}{\mu\phi_0^2}\Big)^{1/3} \tag{3.47}$$

Table 3.2. Analytical scalings of some physical quantities at the maximum mass M_c in the $\mu R \gg 1$ limit.

Mass	$\mu M_c/m_p^2 \sim 1/\Lambda^2$
Radius	$\mu R_c \sim \mu M_c/m_p^2 \sim 1/\Lambda^2$
$\tilde{\omega}_{\rm F}$	$\tilde{\omega}_{\rm F}^c \sim (\mu/m_p)^{1/2}/(\phi_0/m_f) \sim \Lambda^{1/2}/\eta$
Central pressure	$\tilde{P}_c \sim \tilde{\omega}_{\rm F}^4 \sim \Lambda^2/\eta^4$

and the mass

$$M = E(R) = 12\pi R^2\Big(\frac{1}{6}\mu\phi_0^2\Big). \tag{3.48}$$

From Eqs. (3.47) and (3.48), we get

$$R \sim N^{4/9} \qquad M \sim N^{8/9}\,. \tag{3.49}$$

Thus, at least for large N, the mass of the soliton is lower than the energy of the sum of N free particles, ensuring stability.[7]

In the absence of gravity, M can be arbitrarily large. However, due to relativistic effects, we expect the existence of a maximum mass beyond which the object is unstable against radial perturbations. We expect that gravity becomes important when $2GM/R \sim 1$. Therefore, the critical mass M_c can be estimated by simply imposing $R \sim 2GM_c$ in eq. (3.48), yielding $G^2M_c \sim 1/\mu\phi_0^2$ and thus

$$\frac{\mu M_c}{m_p^2} \sim \frac{1}{\Lambda^2}. \tag{3.50}$$

Likewise, one can obtain the scaling of all other relevant quantities, which we collect in Table 3.2.

Self-consistency criteria

When deducing the scaling reported in Table 3.2, we made the following assumptions:

i) $\mu R \gg 1$;

ii) a gas of *massless* fermions in the interior of the star.

In practice, the first assumption is not restrictive (see e.g. [63]). Indeed, since μ^{-1} is the Compton wavelength of the scalar boson, in the context of a *classical* field theory we should always impose $\mu R \gg 1$. In other words, if $\mu R \simeq 1$ the quantum effects of the scalar field become important on the scale of the star and one cannot trust the classical theory anymore. The hypothesis $\mu R \gg 1$ is an essential ingredient in order to approximate the scalar field profile with eq. (3.38), and to assume, as a consequence, that $k_{\rm F}$ is a step function. Besides, it guarantees that the energy

---

[7] This conclusion remains true in the fully relativistic theory as well.

density of the scalar field is near a delta function. Using the scaling reported in Table 3.2, condition *i)* implies $\Lambda \ll 1$.

One may worry that the second assumption can be violated since the scalar field is not located *exactly at* ϕ_0 in the origin $\rho = 0$, and therefore fermions are never exactly massless. It is enough to check that the fermion gas is *very close* to being a massless gas. Let us recall that the effective mass of the fermion is defined as

$$m_{\rm eff}(\rho) = m_f\Big(1 - \frac{\phi(\rho)}{\phi_0}\Big) \tag{3.51}$$

and therefore $m_{\rm eff}(\rho = 0) = m_f\epsilon$. We can say that the fermion gas is effectively massless when $W/P = 3$. From Eqs. (3.5) and (3.6), at the lowest order in ϵ one obtains

$$\frac{W}{P} = 3\Big(1 + \frac{2m_f^2\epsilon^2}{k_{\rm F}^2}\Big) + O(\epsilon^3), \tag{3.52}$$

which indicates we should require

$$\frac{2m_f^2\epsilon^2}{k_{\rm F}^2} \ll 1 \tag{3.53}$$

in the vicinity of the origin at $\rho \simeq 0$. At larger radii, the scalar field gradually moves away from the central configurations and fermions start retaining a bare mass. Inserting eq. (3.39) in the previous condition and expanding eq. (3.26) provides the condition we need to enforce to obey assumption *(ii)*, i.e.,

$$\frac{2m_f^2\epsilon^2}{(12\pi^2 P_c)^{1/2}} \ll 1. \tag{3.54}$$

We express ϵ using the scalar field profile approximation in eq. (3.38). Indeed, with simple manipulations, one finds

$$-\log\epsilon = \mu R \gg 1. \tag{3.55}$$

Substituting (3.55) in (3.54), and neglecting, at this stage, the numerical factors one obtains

$$\log\left(\frac{m_f}{P_c^{1/4}}\right) \ll \mu R. \tag{3.56}$$

Using the scaling relations in Table 3.2, we obtain

$$\log\left(\frac{\eta}{\Lambda^{1/2}}\right) \ll \frac{1}{\Lambda^2}. \tag{3.57}$$

Summing up, the following conditions on the parameters

$$\Lambda \ll 1, \tag{3.58}$$

$$\log\left(\frac{\eta}{\Lambda^{1/2}}\right) \ll \frac{1}{\Lambda^2} \tag{3.59}$$

are our self-consistency criteria to check if we are in a regime in which the scaling reported in Table 3.2 is expected to be valid. While it can be shown that the second condition implies the first, we prefer writing both for the sake of clarity. Notice that, for fixed $\Lambda \ll 1$, one can violate (3.59) for increasing values of η, but only logarithmically.

Confining and deconfining regimes

An important consequence of the scalings collected in Table 3.2 is that the critical mass and radius are independent of η at fixed Λ. We shall call the region of the parameters space where this happens the *confining regime* of the solutions. Indeed, in this regime the size of the soliton is dictated by the parameters of the scalar field, i.e. μ and ϕ_0, regardless of the value of the fermion mass m_f. Physically, we expect that this would be the case when there exists a hierarchy between the scalar and fermion parameters. Since this hierarchy is measured by η, we expect that the confining regime exists only when η is larger than a critical value, η_c.

To better clarify this point, we consider again eq. (3.19) for the Fermi momentum,

$$k_{\mathrm{F}}^2(\rho) = \omega_{\mathrm{F}}^2 e^{-2u(\rho)} - m_f\Big(1 - \frac{\phi(\rho)}{\phi_0}\Big)^2 . \tag{3.60}$$

In the $m_f \to 0$ limit, this quantity becomes positive definite and so the fermionic pressure cannot vanish at any finite radius. In other words, the radius of the star can be arbitrarily large, provided that m_f is sufficiently small. This is nothing but the well-known fact that a star made of purely relativistic gas does not exist.

Hence, if we enter a regime where the fermion bare mass m_f is so small that, even after the scalar field has moved away from the false vacuum (where the effective fermion mass is small by construction), the Fermi gas is still relativistic, then the radius of the star grows fast and a small variation in m_f produces a big variation in the radius. We call this regime the *deconfining regime* of the solution.

In terms of the dimensionless variables defined above, the $m_f \to 0$ limit becomes

$$\tilde{\omega}_{\mathrm{F}} \to \infty. \tag{3.61}$$

Therefore, we expect that, for a given choice of (Λ, η), the confining regime exists only if $\tilde{\omega}_{\mathrm{F}}$ is smaller than a certain value $\tilde{\omega}_{\mathrm{F}}^c$. Using the scaling for $\tilde{\omega}_{\mathrm{F}}^c$ in Table 3.2, this can be translated into the condition

$$\frac{\Lambda^{1/2}}{\eta} < c, \tag{3.62}$$

where c is a constant that has to be determined numerically.

At this point, it is natural to define η_c as the value of η in which eq. (3.62) is saturated. In this way, eq. (3.62) becomes

$$\eta > \eta_c = c\,\Lambda^{1/2}. \tag{3.63}$$

To summarize, when $\eta \gtrsim \eta_c$ (confining regime) the size of the soliton near the maximum mass is mostly determined by the properties of the scalar field, whereas it strongly depends on the fermion mass when $\eta \lesssim \eta_c$ (deconfining regime[8]).

---

[8] Note that, deep in the deconfining regime (when $\eta \to 0$), the Compton wavelength of the fermion, $1/m_f$, might become comparable to or higher than the radius of the star. In this case, we expect the Thomas-Fermi approximation to break down.

3.2.3 Energy conditions

For an energy-momentum tensor of the form

$$T^{\mu}_{\nu} = \mathrm{diag}\{-\rho, P_1, P_2, P_3\}, \tag{3.64}$$

the energy conditions take the following form:

- Weak energy condition: $\rho \geq 0$ and $\rho + P_i \geq 0$.
- Strong energy condition: $\rho + \sum_i P_i \geq 0$ and $\rho + P_i \geq 0$.
- Dominant energy condition: $\rho \geq |P_i|$.

For a spherically symmetric configuration, $P_1 = P_r$ is the radial pressure, while $P_2 = P_3 = P_t$ is the tangential pressure. For our model,

$$\rho = U + V + W\,, \tag{3.65}$$

$$P_r = V - U + P\,, \tag{3.66}$$

$$P_t = -U - V + P\,. \tag{3.67}$$

Since V, W, and P are nonnegative quantities, we obtain $\rho + P_r \geq 0$ and $\rho + P_t \geq 0$. Thus, the weak and strong energy conditions are satisfied if

$$U + V + W \geq 0, \tag{3.68}$$

$$3P - 2U + W \geq 0\,, \tag{3.69}$$

respectively. Since U is also a non-negative quantity, the weak energy condition is always satisfied, while the strong energy condition can be violated. In particular, it is violated even in the absence of fermions ($P = W = 0$).

The dominant energy condition, instead, gives two inequalities:

$$U + V + W \geq |P + V - U|, \tag{3.70}$$

$$U + V + W \geq |P - V - U|. \tag{3.71}$$

One can show that the dominant energy condition is satisfied whenever

$$W + 2(U + V) \geq P, \tag{3.72}$$

This inequality is satisfied if

$$W - P \geq 0\,, \tag{3.73}$$

which can be shown to be true using the analytic expressions of W and P.

To sum up, the weak and dominant energy conditions are always satisfied, while the strong energy condition can be violated (e.g. in the absence of fermions) as generically is the case for a scalar field with a positive potential [51].

3.3 Numerical results

In this section, we present the fermion soliton solutions in spherical symmetry obtained by integrating the field equations (3.24). We will confirm the existence of a solution beyond the thin-wall approximation used in ref. [13]. Also, based on the numerical solutions, we can confirm the scalings derived in the previous sections in a certain region of the parameter space and fix their prefactors.

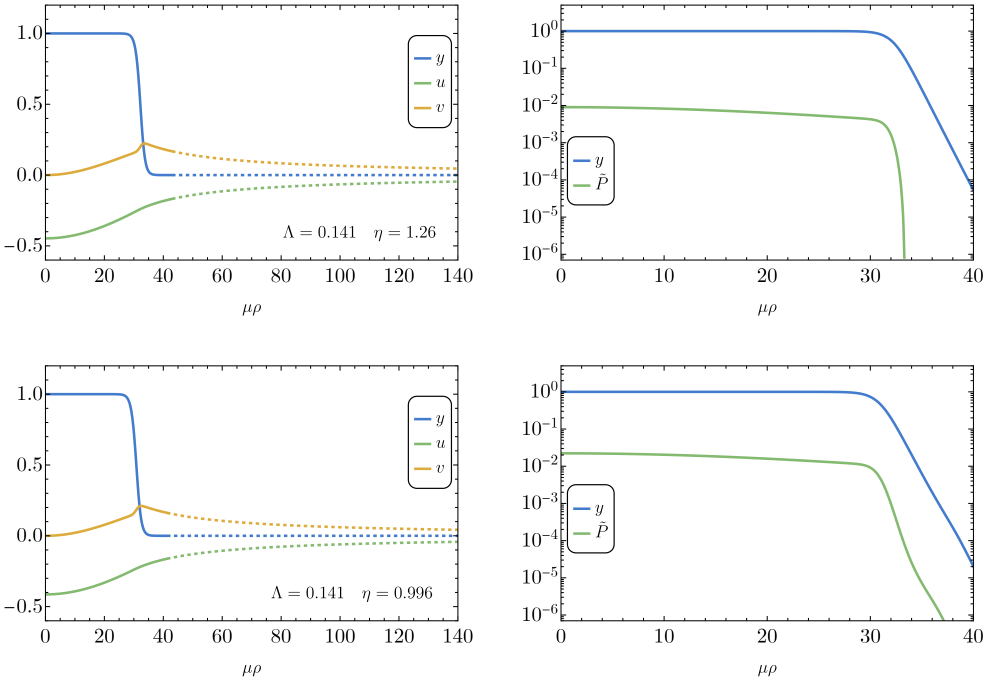

Figure 3.2. Radial profiles of the dimensionless pressure $\tilde{P}$, scalar profile y, and metric functions u (shifted) and v for two example configurations. Continuous lines represent numerical data, whereas dashed lines reconstruct the asymptotic behavior of the solutions by fitting with the Schwarzschild solution. **Top panels:** $\Lambda = 0.141$, $\eta = 1.26$, $\tilde{P}_c = 0.00903$, and $\log_{10}\epsilon = -13.9$. The mass and radius of the soliton fermion star are $\mu M/m_p^2 = 6.14$ and $\mu R = 33.8$, respectively. This solution falls within the confining regime. **Bottom panels:** $\Lambda = 0.141$, $\eta = 0.996$, $\tilde{P}_c = 0.0222$, and $\log_{10}\epsilon = -12.9$. The mass and radius of the soliton fermion star are $\mu M/m_p^2 = 5.71$ and $\mu R = 39.3$, respectively. This solution falls within the deconfining regime.

3.3.1 Numerical strategy

In this section, we summarize the numerical strategy we adopt to find soliton fermion solutions. Given the boundary condition (3.25), the set of equations (3.24) is solved numerically by adopting the following strategy:

1. We fix a certain value of $\tilde{\omega}_\mathrm{F}$;

2. for a given value of $\tilde{\omega}_\mathrm{F}$ and of the central scalar field (i.e., a value of ϵ), we obtain $\tilde{P}_c$ through eq. (3.26), and therefore x through the last equation in (3.24)[9];

3. we integrate the first three equations in (3.24) for the variables (u, v, y), starting from $r \approx 0$ to the point $r = R_f$ where the fermion pressure drops to negligible values, $\tilde{P}(R_f) = 0$;

4. we eliminate the fermionic quantities from the system of equations (3.24) and start a new integration with initial conditions given at $r = R_f$ imposing

---

[9] Equivalently, one can give initially $\tilde{P}_c$, ϵ and determine $\tilde{\omega}_\mathrm{F}$ inverting eq. (3.26).

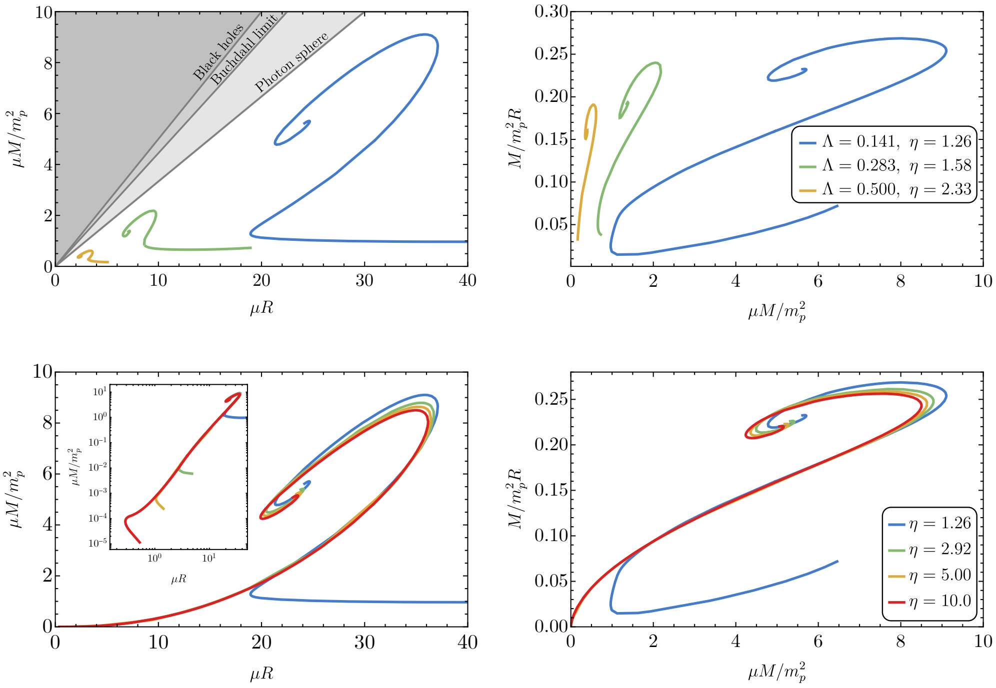

Figure 3.3. Mass-radius (left panels) and compactness-mass (right panels) diagrams for fermion soliton stars. The top panels refer to various values of (Λ, η) in the confining regime ($\eta > \eta_c$; see Sec. 3.2.2). As a reference, in the top-left panel we also draw the lines $R = 2\,GM$, $R = 9/4\,GM$, $R = 3\,GM$, corresponding to the Schwarzschild radius, Buchdhal's limit [28], and the photon-sphere radius. The bottom panels refer to various values of η for fixed $\Lambda = 0.141$. The smallest value of η considered is near but greater than the critical value. The inset shows the curves in logarithmic scale, to highlight that in this case there exists a turning point in the M-R diagram at low masses that proceeds toward the Newtonian limit of small M and large R.

continuity of the physical quantities. That is, the initial conditions on the metric and scalar fields at $r = R_f$ are obtained from the last point of the previous integration up to $r = R_f$;

5. we use a shooting method to find the value of ϵ that allows an asymptotically flat solution to exist, which means imposing $y(r \to \infty) \to 0$;

6. as previously discussed, because the scalar field does not have compact support, we define the radius of the star ($R > R_f$) as that containing 99% of the total mass, i.e. $\tilde{m}(R) = 0.99\,\mu M/m_p^2$ (eq. (3.28)), and the compactness is GM/R;

7. Finally, we repeat the procedure for a range of values of $\tilde{\omega}_{\rm F}$, finding a one-parameter family of solutions. As we shall discuss, in certain regimes (including the deconfining one) this family exists only if $\tilde{P}_c$ is above a certain threshold, therefore lacking a Newtonian limit.

As already noted, a vanishing scalar field ($y = 0, \partial_r y = 0$) is a solution to the scalar equation in eq. (3.24) only if $S = 0$, that is, in the absence of fermions.

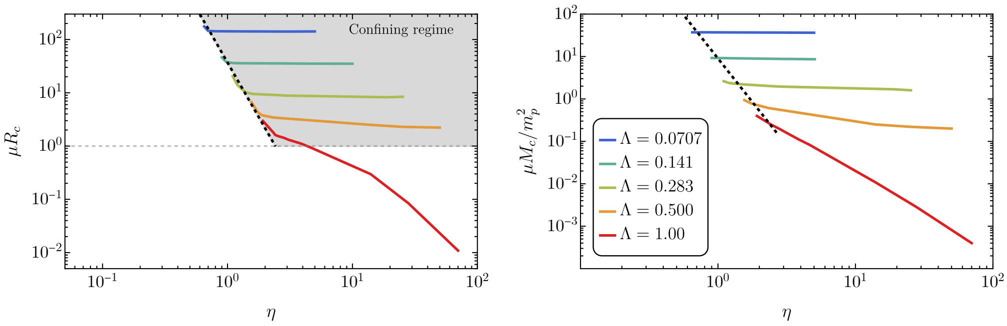

Figure 3.4. Left: Behavior of the critical radius R_c with Λ and η. The scaling (3.63) is highlighted by the diagonal black dashed line. We observe an agreement until $\Lambda \lesssim 0.3$ whereas, for larger Λ, η_c increasingly exceeds the predicted value. The horizontal grid line highlights when the $\mu R > 1$ regime ends. The shaded region above the two dashed lines is the confining regime. **Right:** Behavior of the critical radius M_c with Λ and η. We observe that the critical mass does not exhibit a significant change of behavior for $\eta < \eta_c$.

This ensures that in any solution with $y \to 0$ at infinity the fermion pressure must vanish at some finite radius. Therefore, the fermion soliton solution is described by a fermion fluid confined at $r \leq R_f$ and endowed with a real scalar field that is exponentially suppressed outside the star, as expected from the discussion in Sec. 3.2. A pictorial representation of these compact objects is shown in Fig. 1.1.

As described in the previous section, important parameters are the mass and radius of the critical solutions, M_c and R_c. In practice, we compute these quantities by identifying in the M-R diagram the point of maximum mass.

3.3.2 Fermion soliton stars

First of all, we confirm that fermion soliton stars exist beyond the thin-wall approximation used in ref. [13]. An example is shown in Fig. 3.2 which presents the radial profiles for the metric, scalar field, and fermion pressure.

Inspecting the panels of Fig. 3.2 can help us understand the qualitative difference between solutions in the confining regime (top) and the deconfining one (bottom). In the first case, as soon as the scalar field moves away from its central value at $\rho \to 0$, and the effective mass of the fermion field grows, the pressure quickly drops to zero. This is reflected in the fact that the macroscopic size of the star R is found to be very close to where the scalar field starts moving away from the false vacuum. This is the reason why the macroscopic properties of the star are mainly dictated by the scalar field potential. In the latter case, the small bare mass of fermions makes them remain ultra-relativistic even when the scalar field moves away from the false vacuum, generating a layer where fermionic pressure drops exponentially but remains finite. After the energy of fermions has fallen within the non-relativistic regime, fermionic pressure rapidly vanishes. The existence of such a layer makes the final mass and radius of the star dependent on the fermion mass, see more details below. Also, as the numerical shooting procedure requires matching the asymptotic behavior of the scalar field outside the region where the energy density of the fermions remains sizable, deconfining solutions are characterized by a larger tuning of the parameter controlling the central displacement ϵ.

In Fig. 3.3 we present the mass-radius and compactness-mass diagrams for various values of Λ and η, in the confining regime. In the top panels, we observe that Λ strongly affects the mass-radius scale and the maximum mass, while from the bottom panels, we observe that η has a weaker impact on the maximum mass, as expected from the discussion in Sec. 3.2.

The dependence of M_c and R_c on Λ and η is presented in Fig. 3.4. As expected, we observe that, for a fixed Λ, there is a critical value of η, below which the radius begins to grow rapidly. For $\eta > \eta_c$ and $\Lambda \lesssim 0.5$, we observe that the predictions given in Sec. 3.2 are valid, confirming the existence of a confining regime. Indeed, in that region of the parameter space, both the mass and the radius have little dependence on η. This dependence grows very slowly for an increasing value of η, in agreement with eq. (3.59). Moreover, the value of η_c scales, for $\Lambda \lesssim 0.3$, in agreement with eq. (3.63), while for larger values of Λ it exceeds the analytical scaling. At variance with the critical radius, the critical mass does not exhibit a change of behavior for $\eta < \eta_c$. As a consequence, the compactness decreases quickly.

In general, taking into account all the configurations numerically found, $\log_{10}\epsilon$ lies in the interval $(-150, -0.01)$.

Finally, in Table 3.3 we report the scaling coefficients computed numerically, which are valid in the confining regime ($\eta \gtrsim \eta_c$, $\Lambda \lesssim 0.5$).

3.3.3 On the existence of a Newtonian regime

From the bottom panels of Fig. 3.3, we observe that, even though η has a weak impact on the maximum mass, it can qualitatively change the $M - R$ diagram, especially at low masses. Overall, the mass-radius diagram reassembles that of solitonic boson stars [8, 9, 10, 11] with several turning points in both the mass and the radius, giving rise to multiple branches (see also [64]). The main branch is the one with $M'(R) > 0$ before the maximum mass, which is qualitatively similar to that of strange (quark) stars [65, 22]. However, the low-mass behavior (and the existence of a Newtonian regime) depends strongly on η.

For sufficiently large values of η (always in the confining regime), there exists a low-compactness branch in which $M'(R) < 0$ and where the fermionic pressure is small compared to the energy density, giving rise to a Newtonian regime. However, an interesting effect starts occurring for values of η near, but greater than, the critical one (e.g., the blue curve for $\eta = 1.26$ in the bottom panels of Fig. 3.3[10]) all the way down to the deconfining regime. In this case, there is still a lower turning point in the M-R diagram, but the compactness eventually starts *growing* (see right bottom panel). In this case, there is no Newtonian regime since the compactness is never arbitrarily small.

This peculiar behavior is also related to another important feature of the model, namely the fact that, for η sufficiently small, fermion soliton stars exist only above a minimum threshold for the central fermionic pressure. We clarify this point in

---

[10] Notice that, in the bottom-left panel, it is not possible to see the complete tail of the M-R diagram. As underlined in the text, in the center-right panel of Fig. 3.5 we plot the complete M-R diagram.

Table 3.3. Various scaling of the critical parameters with coefficients derived numerically in the $\Lambda \lesssim 0.5$ range.

Critical mass	$\mu M_c/m_p^2 \approx 0.19/\Lambda^2$
Critical radius	$\mu R_c \approx 0.71/\Lambda^2$
Compactness of the critical solution	$C_c \approx 0.27$
Critical value of the scale ratio	$\eta_c \approx 2.7\,\Lambda^{1/2}$

Fig. 3.5. In the left panels we show the mass of the star as a function of the central fermionic pressure for $\Lambda = 0.141$ and three values of η. For $\eta = 0.966$ and $\eta = 1.26$ (top and center panels), the pressure has a lower bound, corresponding to the absence of a Newtonian limit. For $\eta = 2.92$ (bottom panels) the behavior is qualitatively different and in this case the Newtonian regime is approached as $P_c \to 0$.

To clarify where the minimum pressure and these multiple branches are in the mass-radius diagram, in the right panels of Fig. 3.5, we show data points for $M - R$ using the same color scheme as in the corresponding left panels. Interestingly, the minimum pressure does not correspond to the minimum mass in Fig. 3.5, but it is an intermediate point in the $M - R$ diagram. In the center-right panel we show an extended version of the $\Lambda = 0.141$, $\eta = 1.26$ curve shown in Fig. 3.3. This highlights the peculiar behavior of the new branch, which has a further turning point at large radii.

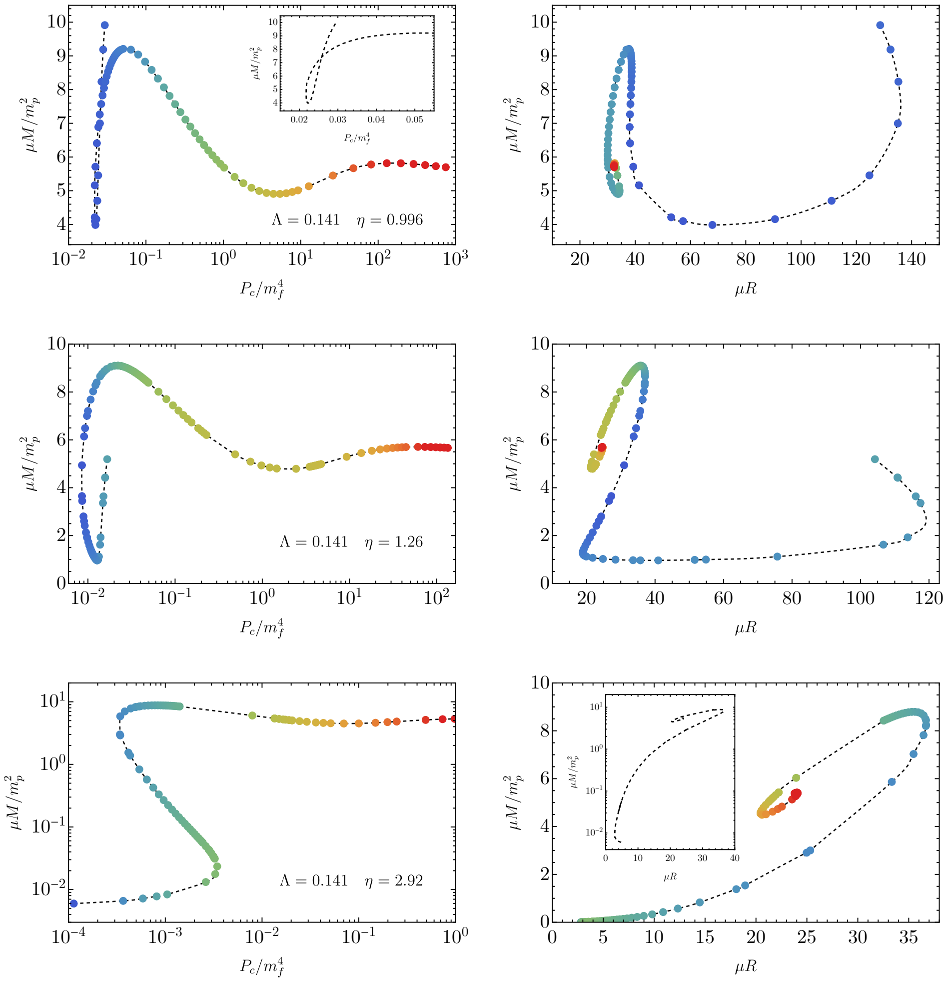

Figure 3.5. **Left panels:** The mass of fermion soliton stars as a function of the central fermionic pressure. **Right panels:** The corresponding mass-radius diagram using the same color scheme as in the left panels, in order to associate with each point the corresponding central pressure. **Top:** $\Lambda = 0.141$ and $\eta = 0.996$. This solution is in the deconfining regime and there is a lower bound on $\tilde{P}_c$ below which no solution exists. **Center:** $\Lambda = 0.141$ and $\eta = 1.26$. This solution is in the confining regime but, also in this case, there exists a lower bound on $\tilde{P}_c$. **Bottom:** $\Lambda = 0.141$ and $\eta = 2.92$. This solution is in the confining regime but, given the larger value of η, there is no lower bound on $\tilde{P}_c$ and a Newtonian regime exists. In all three cases, for a certain range of $\tilde{P}_c$ there are multiple solutions with the same central fermionic pressure and different central values of the scalar field.

Studying the stability of these different peculiar branches [64] is left for future work.[11]

Finally, note that in both cases there are values of the central fermionic pressure corresponding to multiple solutions, each one identified by a different central value of the scalar field.

3.4 Parameter space and astrophysical implications

Given the number of parameters of our model, it is interesting to study the characteristic mass and radius of fermion soliton stars in this theory. By defining

$$q \equiv (\mu\phi_0^2)^{1/3}, \tag{3.74}$$

as long as we are in the confining regime, one finds

$$M_c \sim \frac{0.19}{8\pi}\frac{m_p^4}{q^3} \sim 1.27\, M_\odot \left(\frac{q}{5\times 10^5\,\mathrm{GeV}}\right)^{-3}, \tag{3.75}$$

$$R_c \sim \frac{0.71}{8\pi}\frac{m_p^2}{q^3} \sim 6.5\,\mathrm{km} \left(\frac{q}{5\times 10^5\,\mathrm{GeV}}\right)^{-3}, \tag{3.76}$$

where we included the prefactors obtained using the numerical results. Given the cubic dependence on q, the model can accommodate compact objects of vastly different mass scales, while the compactness at the maximum mass is independent of q, $GM_c/R_c \sim 0.27$, which is slightly larger than that of a typical neutron star, but still smaller than the compactness of the photon sphere. Consequently, one expects fermion soliton stars to display a phenomenology more akin to ordinary neutron stars than to black holes [26]. The authors of ref. [13] considered the value $q = 30\,\mathrm{GeV}$, yielding supermassive objects with $M_c \sim 10^{12}\, M_\odot$ and $R_c \sim 10^{13}\,\mathrm{km} \sim 0.3\,\mathrm{pc}$. Instead, the choice

$$q = q_{\mathrm{astro}} \sim 5\times 10^5\ \mathrm{GeV} \tag{3.77}$$

leads to the existence of soliton solutions of mass and radius comparable to ordinary neutron stars.

Furthermore, the fact that the model is in the confining regime only above a critical value of η, eq. (3.63), implies (using eq. (3.23) and our numerical results)

$$m_f > 2.7\Big(\frac{\sqrt{8\pi}q^3}{m_p}\Big)^{1/2} \sim 0.6\,\mathrm{GeV}\left(\frac{q}{q_{\mathrm{astro}}}\right)^{3/2}, \tag{3.78}$$

a range including the neutron mass. Therefore, the fermion gas can be a standard degenerate gas of neutrons. It is also interesting to combine the above inequality (saturated when $m_f = m_f^c$) with eq. (3.75), finding a relation between the maximum mass of the soliton in the confining regime and the critical fermion mass,

$$M_c \sim 0.46 \left(\frac{\mathrm{GeV}}{m_f^c}\right)^2 M_\odot\,, \tag{3.79}$$

---

[11] We point to ref. [66], where a broad class of related theories is analyzed in terms of energy stability (though without taking gravity into account), and to ref. [67], in which the stability of neutron and boson stars is studied through catastrophe theory. However, the issue of stability in the present work remains open and needs a full radial perturbation analysis.

independently of q. Interestingly, this model allows for subsolar compact objects for fermions at (or slightly heavier than) the GeV scale, whereas it allows for supermassive ($M_c \sim 10^6 M_\odot$) compact stars for a degenerate gas of electrons ($m_f^c \sim 0.5\,\mathrm{MeV}$).

Clearly, the same value of q can be obtained with different combinations of μ and ϕ_0. In general,

$$\mu = 500 \left(\frac{q}{q_{\mathrm{astro}}}\right)^3 \left(\frac{500\,\mathrm{TeV}}{\phi_0}\right)^2 \mathrm{TeV} \tag{3.80}$$

$$= 500 \left(\frac{m_f^c}{0.6\,\mathrm{GeV}}\right)^2 \left(\frac{500\,\mathrm{TeV}}{\phi_0}\right)^2 \mathrm{TeV}\,, \tag{3.81}$$

so $\mu \sim \mathrm{GeV}$ for $q = q_{\mathrm{astro}}$ (or, equivalently, for $m_f^c = 0.6\,\mathrm{GeV}$) and $\phi_0 \sim 3 \times 10^5\,\mathrm{TeV}$. Note that the latter value is still much smaller than the Planck scale, so the condition $\Lambda \ll 1$ is satisfied. From our numerical results, Eqs. (3.75) and (3.76) are valid as long as $\Lambda \lesssim 0.5$, whereas, for larger values of Λ, M_c, R_c, and C_c decrease rapidly and the condition $\mu R \gg 1$ might not hold (see Fig. 3.4). This gives an upper bound on ϕ_0,

$$\phi_0 \lesssim \frac{0.5}{\sqrt{8\pi}} m_p \sim 10^{18}\,\mathrm{GeV}, \tag{3.82}$$

which, using eq. (3.80), can be translated into a lower bound on μ

$$\mu \gtrsim 8.4 \times 10^{-11} \left(\frac{q}{q_{\mathrm{astro}}}\right)^3 \mathrm{eV}. \tag{3.83}$$

Thus, also the scalar-field mass can vastly change depending on the value of q, reaching a lower limit that can naturally be in the ultralight regime.

Finally, in the deconfining regime, there is no minimum fermion mass so solutions can exist also beyond the range dictated by eq. (3.78), but soliton fermion stars in such a regime would be characterized by smaller values of compactness (see discussion in Sec 3.3).

3.5 Conclusions

In this chapter, we have found that fermion soliton stars exist as static solutions to Einstein-Klein-Gordon theory with a scalar potential and a Yukawa coupling to a fermion field. This confirms the results of ref. [13] obtained in the thin-wall approximation and provides a way to circumvent the no-go theorems [50, 51] for solitons obtained with a single real scalar field.

Focusing on spherical symmetry, we have explored the full parameter space of the model and derived both analytical and numerical scalings for some of the relevant quantities such as the critical mass and radius of a fermion soliton star. Interestingly, the model predicts the existence of compact objects in the subsolar/solar (resp. supermassive) range for a standard gas of degenerate neutrons (resp. electrons), which might be connected to an exotic explanation for the LIGO-Virgo mass-gap events that do not fit naturally within standard astrophysical scenarios.

We also unveiled the existence of a confining and deconfining regime – where the macroscopic properties of the soliton are mostly governed by the scalar field parameters or by the fermion mass, respectively – and the fact that no Newtonian analog exists for these solutions for fermion masses below a certain threshold.

Chapter 4

Fermion soliton stars with asymmetric vacua

Summary

Fermion soliton stars are a motivated model of exotic compact objects in which a nonlinear self-interacting real scalar field couples to a fermion via a Yukawa term, giving rise to an effective fermion mass that depends on the fluid properties. In this chapter, we continue our investigation of this model within General Relativity by considering a scalar potential with generic asymmetric vacua. This case provides fermion soliton stars with a parametrically different scaling of the maximum mass relative to the model parameters, showing that the special case of symmetric vacua, in which we recover our previous results, requires fine-tuning. In the more generic case studied here the mass and radius of a fermion soliton star are comparable to those of a neutron star for natural model parameters at the GeV scale. Finally, the asymmetric scalar potential inside the star can provide either a positive or a negative effective cosmological constant in the interior, being thus reminiscent of gravastars or anti-de Sitter bubbles, respectively. In the latter case, we find the existence of multiple, disconnected, branches of solutions.

4.1 Setup

We consider again the theory (3.1), i.e.

$$S = \int \mathrm{d}^4x\sqrt{-g}\Big[\frac{R}{16\pi G} - \frac{1}{2}\partial^\mu\phi\partial_\mu\phi - U(\phi) + \bar{\psi}(i\gamma^\mu D_\mu - m_f)\psi + f\phi\bar{\psi}\psi\Big], \tag{4.1}$$

where R is the Ricci scalar of the metric $g_{\mu\nu}$, ϕ is the scalar field with potential $U(\phi)$, ψ is the fermion with mass m_f, and f is the Yukawa coupling. As discussed in the previous chapter, the latter provides an effective mass, $m_{\text{eff}} = m_f - f\phi$, that is crucial for the existence of these solutions [13, 1], which indeed circumvent classical no-go theorems for the existence of solitons [50, 51]. The covariant derivative D_μ in eq. (4.1) takes into account the spin connection of the fermionic field.

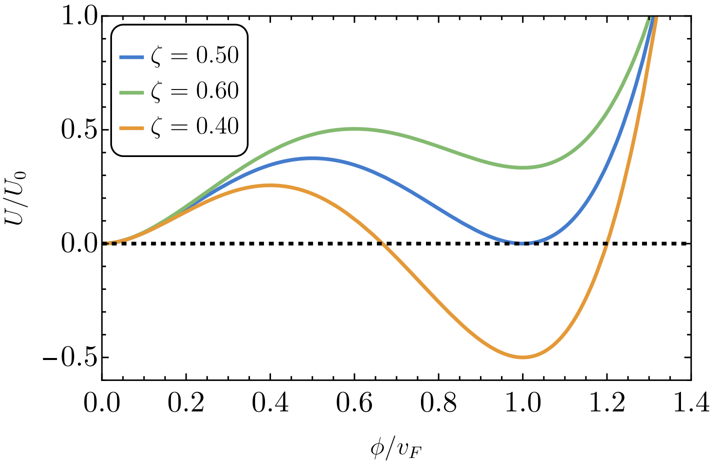

Figure 4.1. Scalar potential in eq. (4.2) normalized with respect to $U_0 = \mu^2 v_\mathrm{F}^2/12$ as function of ϕ/v_F for three different values of ζ.

Here we consider a generalized scalar potential,

$$U(\phi) = \frac{\mu^2 v_\mathrm{F}^2}{12}\frac{v_\mathrm{F}}{v_\mathrm{B}}\Big(\frac{\phi}{v_\mathrm{F}}\Big)^2\Big[3\Big(\frac{\phi}{v_\mathrm{F}}\Big)^2 - 4\Big(\frac{\phi}{v_\mathrm{F}}\Big)\Big(1+\frac{v_\mathrm{B}}{v_\mathrm{F}}\Big) + \frac{6v_\mathrm{B}}{v_\mathrm{F}}\Big]. \tag{4.2}$$

The latter features two minima at $\phi = 0$ and $\phi = v_\mathrm{F}$, separated by a maximum located at $\phi = v_\mathrm{B}$. The potential in eq. (4.2) can be also written as

$$U(\phi) = \frac{\mu^2}{2!}\phi^2 + \frac{\kappa}{3!}\phi^3 + \frac{\lambda}{4!}\phi^4, \tag{4.3}$$

with the definitions $\lambda = \frac{6\mu^2}{v_\mathrm{B} v_\mathrm{F}}$, $\kappa = -\frac{\lambda}{3}(v_\mathrm{F} + v_\mathrm{B})$.

By defining $\zeta = v_\mathrm{B}/v_\mathrm{F}$, it is possible to control the energy difference between vacua, as illustrated in Fig. 4.1. When $\zeta = 1/2$ the two minima are degenerate, whereas if $\zeta > 1/2$ the minimum $\phi = v_\mathrm{F}$ has more energy than $\phi = 0$. The opposite happens for $\zeta < 1/2$.

In the degenerate case $\zeta = 1/2$, eq. (4.2) takes the simple form

$$U(\phi) = \frac{1}{2}\mu^2\phi^2\Big(1 - \frac{\phi}{v_\mathrm{F}}\Big)^2, \tag{4.4}$$

which is the potential originally considered in [13] and fully investigated in the previous chapter.

We will focus on scenarios in which the fermion becomes effectively massless (i.e. $m_\mathrm{eff} = 0$) when the scalar field sits on the second vacuum, $\phi = v_\mathrm{F}$. This condition implies fixing

$$f = \frac{m_f}{v_\mathrm{F}}. \tag{4.5}$$

We will consider spherically symmetric equilibrium configurations, whose background metric can be expressed as

$$\mathrm{d}s^2 = -e^{2u(\rho)}\mathrm{d}t^2 + e^{2v(\rho)}\mathrm{d}\rho^2 + \rho^2(\mathrm{d}\vartheta^2 + \sin^2\vartheta\,\mathrm{d}\varphi^2), \tag{4.6}$$

in terms of two real metric functions $u(\rho)$ and $v(\rho)$.

As discussed in Sec. 3.1.1, fermions are treated through the Thomas-Fermi approximation [13, 1], practically meaning that they enter Einstein's equations as a perfect fluid characterized by an energy-momentum tensor of the form

$$T^{[f]}_{\mu\nu} = (W + P)u_\mu u_\nu + P g_{\mu\nu}, \tag{4.7}$$

where W is the energy density and P is the pressure of the fluid, while they also enter the scalar field equation through the scalar density S.

Following exactly the same steps discussed in sec. 3.1.2 (in particular we introduce dimensionless parameters Λ and η as in eq. (3.23)), one finds the same field equations given in eq. (3.24)

4.1.1 Scaling arguments

As highlighted in sec. 3.2.2, simple analytical estimates are possible in the macroscopic limit $\mu R \gg 1$, by studying eq. (4.1) in the absence of gravity (R is the stellar radius[1]).

The main physical difference with respect to the $\zeta = 1/2$ case is the presence of a nonzero energy density associated with the scalar field in the interior of the star. From eq. (4.2), the latter is

$$\varrho = U(\phi = v_{\rm F}) = \frac{\mu^2 v_{\rm F}^2}{12\zeta}(2\zeta - 1)\,. \tag{4.8}$$

In general, the total energy of the system is

$$E = E_k + E_s + E_v, \tag{4.9}$$

where E_k is the fermion energy, while $E_s = 4\pi R^2(\frac{1}{6}\mu v_{\rm F}^2)$, $E_v = \frac{4\pi}{3}R^3\varrho$ are the surface and the volume energy of the scalar field, respectively. The quantity $s = 1/6\,\mu v_{\rm F}^2$ plays the role of a surface energy density. The minimum-energy condition, $\partial E/\partial R = 0$ gives $E_k = 2E_s + 3E_v$, which in turn yields

$$M := E_{\min} = 12\pi s R^2 + \frac{16}{3}\pi\varrho R^3. \tag{4.10}$$

We estimate the critical mass M_c as the point at which $R \sim 2GM$. This gives a quadratic equation, whose positive root is

$$M_c \sim -\frac{s}{2\varrho G} + \frac{s}{2\varrho G}\sqrt{1 + \frac{4\varrho}{Gs^2}}. \tag{4.11}$$

In the limit $\varrho/Gs^2 \ll 1$, i.e. when the surface energy density dominates over that of the volume,

$$\frac{\mu M_c}{m_p^2} \sim \frac{1}{\Lambda^2}, \tag{4.12}$$

which is indeed the scaling found in the case of perfect degeneracy, $\zeta = 1/2$, studied in the previous chapter.

---

[1] In the numerical procedure, the radius R is defined as that containing 99% of the total mass (see 3.3.1).

In the opposite limit, $\varrho/Gs^2 \gg 1$, when the volume energy dominates we get

$$M_c \sim \frac{1}{G^{3/2}|\varrho|^{1/2}}. \tag{4.13}$$

Intriguingly, the latter scaling is what we would get from a bubble of cosmological constant $8\pi G\,\varrho$. As we shall discuss later, depending on the sign of ϱ, in this limit we can have a compact object with either a positive or a negative effective cosmological constant in the interior, reminiscent of gravastars [68, 36, 69] or anti-de Sitter bubbles [37], respectively.

Notice that eq. (4.13) can be also written as

$$\frac{\mu M_c}{m_p^2} \sim \frac{1}{\Lambda}, \tag{4.14}$$

showing a parametrically different scaling with respect to eq. (4.12). Moreover, using eq. (4.8) we get

$$\frac{\varrho}{Gs^2} \sim \frac{1}{\Lambda^2}\frac{\zeta - \frac{1}{2}}{\zeta}. \tag{4.15}$$

Remarkably, in the $\Lambda \ll 1$ limit (which, as we shall discuss, is the regime in which we find compact configurations of astrophysical interest) the volume energy dominates as soon as ζ departs from $1/2$. Therefore, the case of degenerate vacua, originally proposed in ref. [13], appears unnaturally fine-tuned.

Finally, we highlight that the macroscopic limit $\mu R \gg 1$ parametrically corresponds to the region $\Lambda \ll 1$. Indeed, the dimensionless radius of the critical configuration μR_c shows the same scaling of the critical mass (see eq. (4.12) or eq. (4.14)) because of the relation $R_c \sim 2GM_c$.

4.1.2 Confining regime

Along the line of arguments given in sec. 3.2.2 and in sec. 4.1.1, it is possible to compute the scaling of $\tilde{\omega}_{\mathrm{F}}$ for the critical solution in the regime $\mu R \gg 1$. In this case, the real scalar field solution is well approximated by a stiff Fermi function [13, 62]

$$\phi(\rho) \approx \frac{v_{\mathrm{F}}}{1 + e^{\mu(\rho - R)}}, \tag{4.16}$$

which sharply interpolates between the two vacua in a region of size μ^{-1}. In that region, the effective mass m_{eff} quickly increases allowing the fermion pressure to go to zero. Therefore, the (relativistic) Fermi gas is well confined in the core of the star $\rho \leq R$. This implies that the Fermi momentum is nearly constant in the core and equal to its central value ω_{F}. Consequently, the fermion number density is estimated as $\sim \omega_{\mathrm{F}}^3$ and the total number of fermions in the configuration is then $N \sim (R\omega_{\mathrm{F}})^3$. Hence,

$$\omega_F \sim N^{1/3}\frac{1}{R}. \tag{4.17}$$

Assuming $\zeta > 1/2$, the fact that $\mu R \gg 1$ (which, as already discussed, corresponds to $\Lambda \ll 1$) implies thought eq. (4.15) that that E_v dominates over E_s. Thus,

$$\varrho R^3 \sim E_v \sim E_k \sim N^{4/3}\frac{1}{R} \Rightarrow N^{1/3} \sim \varrho^{1/4} R. \tag{4.18}$$

Substituting eq. (4.18) into eq. (4.17), one gets $\omega_{\rm F} \sim \varrho^{1/4}$. By using eq. (4.8) and the definitions of the dimensionless quantities given in Sec. 4.1, we finally obtain[2]

$$\tilde{\omega}_{\rm F} \sim \frac{1}{\eta}\Big(\frac{2\zeta - 1}{12\zeta}\Big)^{1/4}. \tag{4.19}$$

The latter quantity is needed to find the confining regime of the model, which is the region in the parameter space where the mass and radius of the solution do not depend significantly on m_f. As discussed in sec. 3.2.2, we expect that, for a given choice of (Λ, η), the confining regime exists only if $\tilde{\omega}_{\rm F}$ is smaller than a certain value $\tilde{\omega}_{\rm F}^{\rm max}$. Using eq. (4.19),

$$\tilde{\omega}_{\rm F} < \tilde{\omega}_{\rm F}^{\rm max} \Rightarrow \eta > \eta_c = C(\zeta). \tag{4.20}$$

At variance with the $\zeta = 1/2$ case (where a similar argument gives $\eta_c \sim \Lambda^{1/2}$, see sec. 3.2.2), in the nondegenerate case η_c is independent of Λ. We numerically checked that $C(\zeta) \sim 1$. Therefore, as long as $\Lambda \ll 1$, requiring

$$\eta \gtrsim 1, \tag{4.21}$$

is enough to ensure that the solutions lay in the confining regime.

4.1.3 Binding energy

Given a configuration made of N fermions, whose total mass is M, it is useful to define the binding energy

$$E_B := M - m_f N. \tag{4.22}$$

We wish to compare the energy of the relativistic configuration, in which gravity and the scalar interaction act as a glue, with the energy of the configuration in which the N fermions are free particles. If $E_B < 0$ the relativistic configuration is stable under dispersion into free particles, i.e. the system is gravitationally bound.

In the Thomas-Fermi approximation, the number of fermions is [13]

$$N = \frac{4}{3\pi}\frac{m_f^3}{\mu^3}\int {\rm d}r\, r^2 e^{v(r)} x^3(r) \equiv \frac{m_f^3}{\mu^3}\tilde{N}\,. \tag{4.23}$$

Using eq. (3.23), we can rewrite eq. (4.22) as

$$\frac{\mu E_B}{m_p^2} = \frac{\mu M}{m_p^2} - \frac{\eta^4\Lambda^2}{8\pi}\tilde{N}. \tag{4.24}$$

Since $N \sim (R\omega_{\rm F})^3$, the combination of eq. (4.14) and eq. (4.19) gives $\tilde{N} \sim \frac{1}{(\Lambda\eta)^3}$. Substituting the latter into eq. (4.24) finally yields

$$\frac{\mu E_B}{m_p^2} \sim \frac{1}{\Lambda}\Big(1 - \eta\Big)\,. \tag{4.25}$$

Thus, the condition $E_B < 0$ translates again into eq. (4.21). In other words, being in the confining regime ensures also stability against dispersion into free particles.

---

[2] In the degenerate case $\zeta = 1/2$, the scaling is parametrically different, see Table II in the previous chapter.

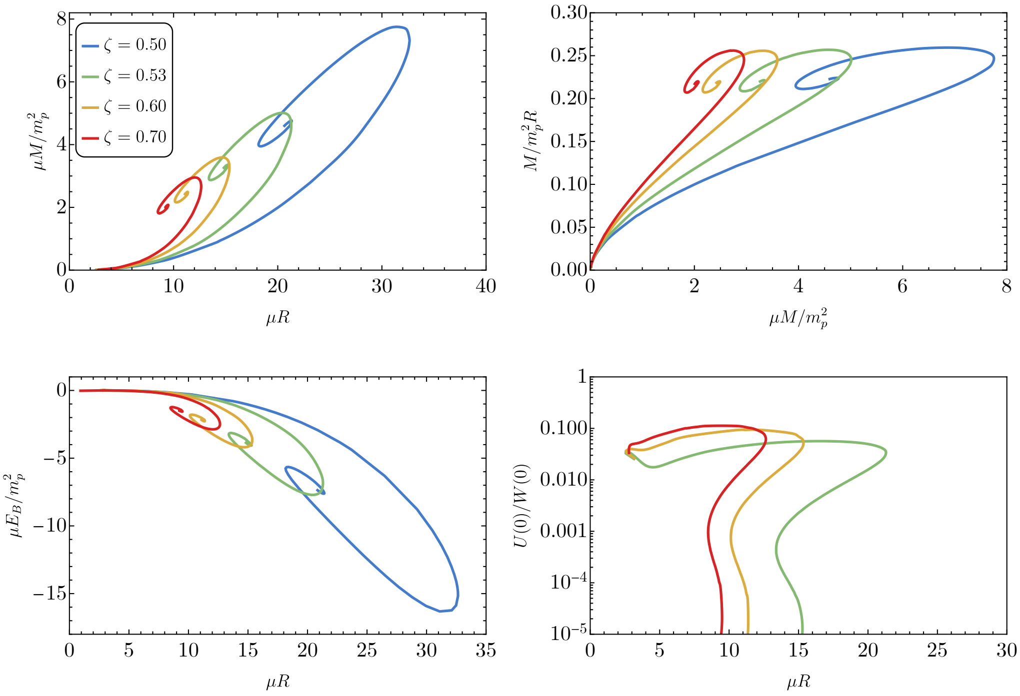

Figure 4.2. Mass-radius (left top panel), compactness-mass (right top panel), binding energy (left bottom panel), and ratio $U(\rho = 0)/W(\rho = 0)$ (right bottom panel) for fermion soliton stars with an effective positive cosmological constant in the interior ($\zeta > 1/2$) as the asymmetry between vacua grows. We fixed $\Lambda = 0.15$ and $\eta = 3$. The latter are representative values such that the Newtonian limit exists and the configurations lie in the confining regime, where the dependence of the critical mass on η is very weak. Varying Λ does not qualitatively change the behaviors of the diagrams. There exists a turning point in the M-R diagrams at low masses, which cannot be seen from the figure, that proceeds towards the Newtonian limit of small M and large R, similarly to what already found in the degenerate case. In the bottom-right panel, we do not show the degenerate curve $\zeta = 1/2$ since in this case $U(0) \approx 0$ by construction. Note that $U(0)/W(0) \to 0$ in the large central pressure limit, corresponding to the spiraling behavior in the $M - R$ diagram.

4.1.4 Energy conditions

If $\zeta > 1/2$ (corresponding to a positive effective cosmological constant in the interior), the scalar potential is positive definite and the same arguments discussed in sec. 3.2.3 hold, i.e. the weak and dominant energy conditions are satisfied, whereas the strong energy condition is violated. Different conclusions have to be drawn when $\zeta < 1/2$ (corresponding to a negative effective cosmological constant in the interior). In this case, the scalar potential is negative around $\phi = v_{\rm F}$, which in turn leads to a violation of the weak energy condition. Indeed, the latter is satisfied in $\phi \approx v_{\rm F}$, i.e. $\rho \approx 0$, if

$$U(\rho \approx 0) + W(\rho \approx 0) \geq 0. \tag{4.26}$$

Being the effective fermion mass negligible around $\phi \approx v_{\mathrm{F}}$, $W(\rho \approx 0) \approx 3P_c$. Using this fact, together with eq. (4.8), eq. (4.26) gives

$$3P_c + \frac{\mu^2 v_{\mathrm{F}}^2}{12\zeta}(2\zeta - 1) \geq 0. \tag{4.27}$$

Being $P_c = m_f^4 \tilde{P}_c$, we finally obtain that the weak energy condition imposes

$$\tilde{P}_c \geq \frac{1}{\eta^4} \frac{(1 - 2\zeta)}{36\zeta}. \tag{4.28}$$

As expected, this is trivially true if $\zeta > 1/2$. Conversely, it could be violated when $\zeta < 1/2$, as we show using the following heuristic argument (and exactly via numerical integration in the next section). Thinking in terms of the classical mechanics analogy described in sec. 3.2, when $\zeta < 1/2$ the false vacuum $\phi = v_{\mathrm{F}}$ of the inverted potential has more energy than the true vacuum $\phi = 0$. Thus, the particle can reach the true vacuum even in the absence of the fermions, which means that the solution exists also in the $P_c \to 0$ limit[3] . As we lower P_c, there will be a point in which the inequality (4.28) does not hold anymore. The existence of the latter point is confirmed by numerical results (see next section) which also show that the binding energy of solutions that violate (4.28) can be positive, i.e. there exist configurations energetically unstable.

4.2 Numerical results

A fermion soliton star is described by a core of relativistic fermion fluid mixed with an effective cosmological constant, surrounded by a shell of real scalar field that is exponentially suppressed outside the star. Depending on the value of ζ, we find different behaviors. If $\zeta = 1/2$ the effective cosmological constant vanishes and we recover the degenerate case presented in the previous chapter. If $\zeta > 1/2$, the effective cosmological constant inside the core is positive and, as we shall see, the solution follows the qualitative picture outlined in the previous section. Finally, if $\zeta < 1/2$ a different behavior appears, due to the violation of the weak energy condition. We shall refer to the $\zeta > 1/2$ and $\zeta < 1/2$ cases as *de Sitter and anti-de Sitter interiors*, respectively, although we stress that the metric in the interior would be effectively (anti) de Sitter only if the energy density of the scalar field dominates. As we shall discuss, this can be the case for certain configurations with an effective negative cosmological constant, while an effective positive cosmological constant never dominates the fermionic contribution.

4.2.1 De Sitter interior ($\zeta > 1/2$)

In Fig. 4.2 we present the mass-radius and compactness-mass diagrams for various values of $\zeta > 1/2$, in the confining regime. We observe that ζ affects the mass-radius scale and the maximum mass (left panel), while it has a weaker impact on the

---

[3] This is not in contradiction with the no-go theorem stated in ref. [51] since for $\zeta < 1/2$ the scalar field potential is not positive definite.

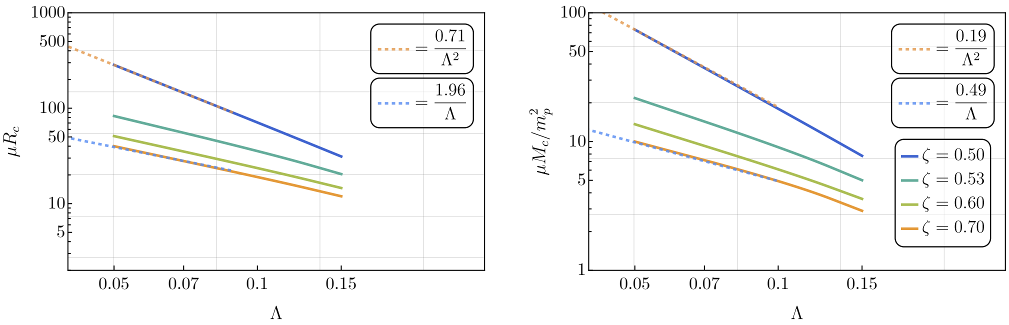

Figure 4.3. Critical radius R_c (left panel) and mass M_c (right panel) as functions of Λ and ζ. In the degenerate case ($\zeta = 1/2$), both quantities scale as $1/\Lambda^2$ in the $\Lambda \ll 1$ limit, while for $\zeta > 1/2$ they scale as $1/\Lambda$. These results are in agreement with the analytical estimates given in Sec. 4.1.1.

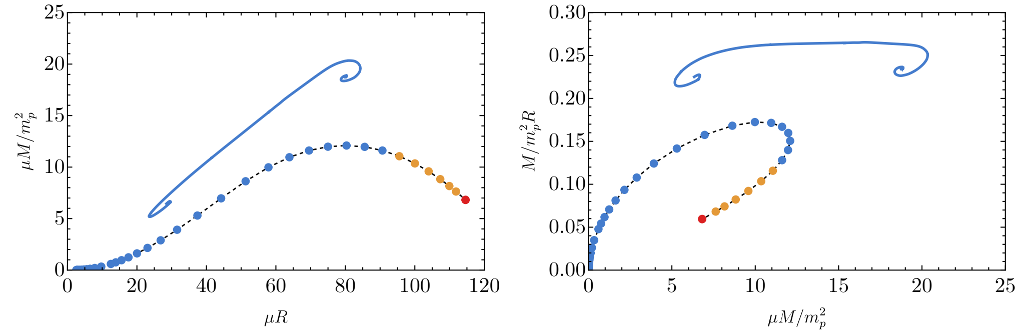

Figure 4.4. Mass-radius (left panel) and compactness-mass (right panel) diagrams for fermion soliton stars with an anti-de Sitter core. We fixed $\Lambda = 0.15$, $\eta = 3$ and $\zeta = 0.49$. Note the presence of two disconnected branches. The blue curves/points correspond to solutions satisfying the weak energy condition, while the others violate eq. (4.28). The red circle corresponds to $\tilde{P}_c \to 0$, i.e. a purely-scalar solitonic configuration in the absence of fermions that does not exist in the $\zeta \geq 1/2$ case.

compactness (right panel). Moreover, the binding energy is negative, which means that the configurations are stable against dispersion into free particles.

The dependence of M_c on Λ and ζ is presented in Fig. 3.4. As expected, $M_c \sim 1/\Lambda^2$ when there is a perfect symmetry between vacua ($\zeta = 1/2$), whereas for any $\zeta > 1/2$, the scaling changes parametrically in $M_c \sim 1/\Lambda$.

4.2.2 Anti-de Sitter interior ($\zeta < 1/2$)

In Fig. 4.4 we present the mass-radius diagram for $\zeta = 0.49$. The latter shows a different behavior from the $\zeta \geq 1/2$ case, due to the presence of two disconnected branches of solutions.

In particular, we highlight the existence of the point (red circle in Figs. 4.4

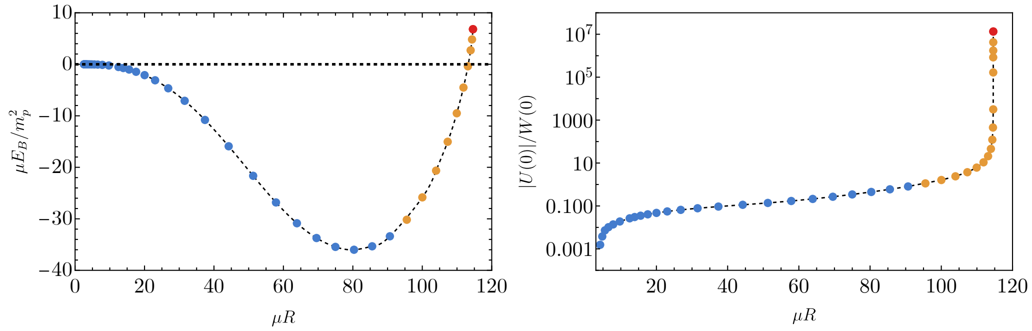

Figure 4.5. Binding energy (left panel) and ratio $|U(\rho = 0)|/W(\rho = 0)$ for the lower branch shown in Fig 4.4, using the same color scheme to highlight the violation of the weak energy conditions (4.28). We observe that there exists a set of solutions around $\mu R \sim 110$ where $|U(\rho = 0)|/W(\rho = 0) \gg 1$ while the binding energy is still negative.

and 4.5) mentioned in Sec. 4.1.4, where the fermion density is negligible[4], which in turn is linked with the divergence of the ratio $|U(\rho = 0)|/W(\rho = 0)$ shown in the right panel of Fig. 4.5. Moreover, in the left panel of Fig. 4.5 we show that the latter point is unstable with respect to dispersion into free particles.

Remarkably, from Fig. 4.5 we observe that there exists an intermediate regime, in which $|U(\rho = 0)|/W(\rho = 0) \gg 1$, but the configurations are gravitationally bound. This means that inside these solutions there is essentially an anti-de Sitter core, whereas the fermions, although with a negligible energy density in the core, are still crucial to energetically bind the configurations. As an example, we show one of these solutions in Fig. 4.6.

Analogous configurations, but with a de Sitter spacetime inside, do not exist when $\zeta > 1/2$. Indeed, in the latter case, fermions are always characterized by a higher energy density in the core than the scalar field, because they have to fill the energy gap between the false vacuum and the true vacuum of the inverted potential (when $\zeta \geq 1/2$ the solution does not exist in the absence of fermions). This is explicitly shown in the bottom-right panel of Fig. 4.2.

The latter results and the existence of two branches for $\zeta < 1/2$ can be better understood by looking at Fig. 4.7, where we show the mass as a function of $\tilde{\omega}_{\rm F}$ for both $\zeta < 1/2$ and $\zeta > 1/2$. In particular, we observe that for $\zeta \geq 1/2$ there exists a minimum value of $\tilde{\omega}_{\rm F}$, below which no solution is found. For $\zeta < 1/2$, instead, $\tilde{\omega}_{\rm F}$ can be arbitrarily small. This causes the detachment between the two branches of the $\zeta = 0.49$ curve, which also manifests in Fig. 4.4.

The existence of two branches makes it harder to identify configurations that are expected to be stable under radial perturbations. In this case, it is particularly interesting and important to perform a radial stability analysis, which is left for future work. In the next section, we shall focus on the more standard $\zeta > 1/2$ case.

---

[4] Analogous configurations, characterized by the absence of fermions and the violation of the WEC, were already discussed in the literature under the name of 'scalarons' and studied in connection with hairy black holes [52, 70, 71, 72].

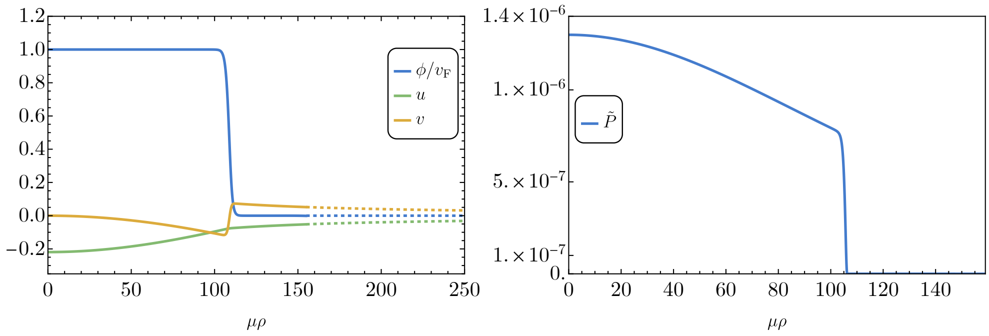

Figure 4.6. Radial profiles of scalar field ϕ, normalized with respect to $v_{\rm F}$, metric functions u, v (left panel) and fermion pressure (right panel) for a configuration with an effective anti-de Sitter core, but still a negative binding energy ($\Lambda = 0.15$, $\eta = 3$, $\zeta = 0.49$). Continuous lines represent numerical data, whereas dashed lines reconstruct the asymptotic behavior of the solution by fitting with the Schwarzschild spacetime. We observe a sharp (but continuous) transition between anti-de Sitter and Schwarzschild around $\mu\rho \sim 110$. The mass and radius of this configuration are $\mu M/m_p^2 \approx 7.63$ and $\mu R \approx 111.8$, the compactness is $C \approx 0.068$, while the solution parameters are $\tilde{P}_c = 1.30 \times 10^{-6}$ and $\log_{10}\epsilon = -44.8$. The binding energy is $\mu E_B/m_p^2 \approx -4.51$ and the ratio between cosmological constant and central fermion density inside is $|U(\rho = 0)|/W(\rho = 0) \approx 10.8$.

4.3 Parameter space and astrophysical implications

When $\zeta > 1/2$, it is straightforward to identify a critical mass M_c (and corresponding radius R_c) as the point of maximum mass in the M-R diagram, Fig. 4.2. As heuristically shown in Sec. 4.1.1 for $\Lambda \ll 1$, and confirmed numerically in Fig. 4.3 as long as $\Lambda \lesssim 0.15$, in this regime the critical mass and radius scale as

$$\frac{\mu M_c}{m_p^2} = A(\zeta, \eta)\,\frac{1}{\Lambda}, \tag{4.29}$$

$$\mu R_c = B(\zeta, \eta)\,\frac{1}{\Lambda}. \tag{4.30}$$

The region ($\Lambda \lesssim 0.15, \eta = 3$) is inside the confining regime, where the dependence of the critical quantities on η is very weak (see 3.3.2). Thus, within very good approximation A, B are functions of ζ only. Numerical fits show that $A(\zeta), B(\zeta)$ are functions of order unity (see legend in Fig. 4.3). Therefore, assuming $A, B \sim 1$ and defining $q = (\mu v_{\rm F})^{1/2}$, it is possible to give the following general estimate of the critical quantities,

$$\begin{aligned} M_c &\sim \mathcal{O}(M_\odot)\Big(\frac{0.6\,\text{GeV}}{q}\Big)^2, \\ R_c &\sim \mathcal{O}(\text{km})\Big(\frac{0.6\,\text{GeV}}{q}\Big)^2. \end{aligned} \tag{4.31}$$

Hence, the model can accommodate compact objects of vastly different mass scales, while the compactness at the maximum mass is independent of q, and equals to $GM_c/R_c \approx 0.27$ (see top-right panel of Fig. 4.2), which is slightly larger than that of

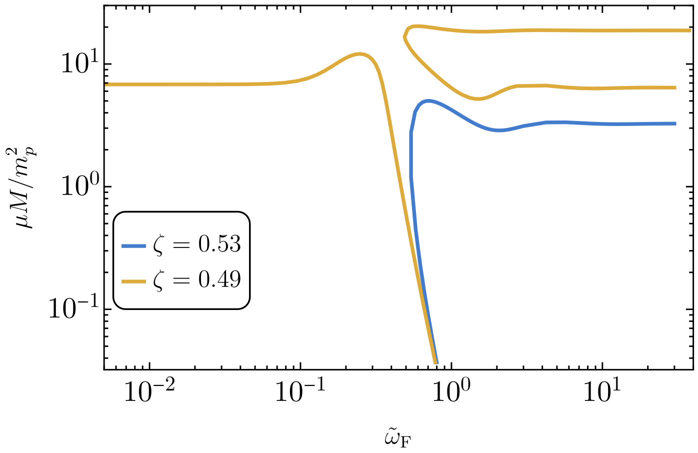

Figure 4.7. Mass as a function of $\tilde{\omega}_{\rm F}$. We fixed $\Lambda = 0.15$, $\eta = 3$. For $\zeta = 0.53$ (representative of $\zeta \geq 1/2$), there exists a minimum value of $\tilde{\omega}_{\rm F}$ around 0.5, while for $\zeta = 0.49$ (representative of $\zeta < 1/2$) $\tilde{\omega}_{\rm F}$ can be arbitrarily small, which in turn leads to two branches of solutions.

a typical neutron star, but still smaller than the compactness of the photon sphere of a Schwarzschild black hole ($GM/R = 1/3$). As a result, one expects fermion soliton stars to display a phenomenology more akin to ordinary neutron stars than to black holes [26].

Moreover, condition eq. (4.21) gives

$$m_f \gtrsim q. \tag{4.32}$$

Interestingly, the choice $q \sim q_{\rm astro} = 0.6\,{\rm GeV}$ leads to the existence of fermion soliton stars with mass and radius comparable to ordinary neutron stars, with a fermion mass in the natural energy scale $\mathcal{O}({\rm GeV})$. This is a striking difference with respect to the degenerate model presented in the previous chapter, which required scalar field parameters at much higher energy scales in order to obtain solar-mass compact configurations.

4.4 Discussion and Conclusions

We have constructed physically admissible configurations of fermion soliton stars in the presence of a scalar potential featuring two asymmetric vacuum states. This generalizes the original model of [13] (recently explored in full general relativity [1] and presented in the previous chapter), in which the two vacua are degenerate [2].

The breaking of the degeneracy drastically changes the qualitative properties of the solution, thus unveiling that the degenerate case is nongeneric and requires fine-tuning. First of all, the scaling of the maximum mass relative to the model parameters is different from the degenerate case and makes it easier to obtain solar-mass compact solutions with natural model parameters in the GeV scale. Secondly, the breaking of the degeneracy implies that the interior of the star can be described by either a positive or a negative effective cosmological constant; the latter case (effective anti-de Sitter core) being associated with compact solutions with further peculiar properties.

The case of de Sitter interior provides a concrete realization of a model somehow reminiscent of that of gravastars [68, 36, 69], which are indeed supported by a positive cosmological constant in the interior and feature anisotropic pressure [73] (naturally provided by the scalar field in our model). Our model is anyway different from the original gravastar, since for $\zeta > 1/2$ the contribution of the fermion fluid is comparable to, and typically much larger than, that of the effective cosmological constant (see right bottom panel of Fig. 4.2). Interestingly, a recent concrete realization of a gravastar was proposed in ref. [74].

Likewise, the case of anti-de Sitter interior is somehow reminiscent of that of anti-de Sitter bubbles [37]. This case shows interesting features such as multiple branches and viable configurations in which the contribution of fermions is negligible (but anyway needed for the existence of bound solutions).

Chapter 5

Compact objects from non-perturbative vacuum scalarization

Summary

In this chapter, we explore applications of the previous findings adopting a particle physics perspective. We consider a theory in which a real scalar field is Yukawa-coupled to a fermion and has a potential with two non-degenerate vacua. If the coupling is sufficiently strong, a collection of N fermions deforms the true vacuum state, creating energetically favored false-vacuum pockets in which fermions are trapped. We embed this model within General Relativity and prove that it admits self-gravitating compact objects where the scalar field acquires a non-trivial profile due to non-perturbative effects. We discuss some applications of this general mechanism: i) *neutron soliton stars* in low-energy effective QCD, which naturally happen to have masses around $2M_\odot$ and radii around $10\,\mathrm{km}$ even without neutron interactions; ii) *Higgs false-vacuum pockets* in and beyond the Standard Model; iii) *dark soliton stars* in models with a dark sector. In the latter two examples, we find compelling solutions naturally describing centimeter-size compact objects with masses around $10^{-6}M_\odot$, intriguingly in a range compatible with the Optical Gravitational Lensing Experiment (OGLE) + Hyper Suprime-Cam (HSC) microlensing anomaly. Besides these interesting examples, the mechanism of non-perturbative vacuum scalarization may play a role in various contexts in and beyond the Standard Model, providing a support mechanism for new compact objects that can form in the early Universe, can collapse into primordial black holes through accretion past their maximum mass, and serve as dark matter candidates.

5.1 The mechanism of non-perturbative vacuum scalarization

Along the lines of the previous chapters, we consider a simple model for NTSs in which a real scalar field h is coupled to a fermion through a Yukawa coupling.

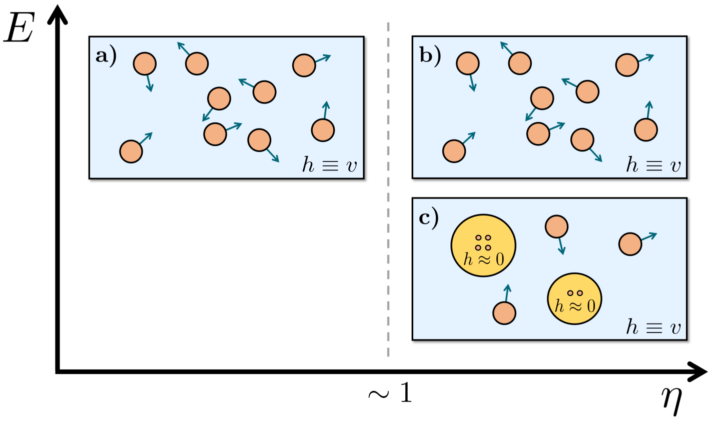

Figure 5.1. Sketch of the mechanism, showing the energy E of different configurations as a function of η, a fundamental parameter defined in eq. (5.13). The bigger η the more the theory becomes strongly coupled. The orange balls represent massive fermions, whereas the yellow balls represent the false vacuum pockets of the scalar field in which the fermions are massless (and therefore depicted by smaller orange balls). **(a)** Standard ground state of the system. **(b), (c)** Whenever $\eta \gtrsim 1$, it is energetically convenient for the system to trap a fraction of fermions in false vacuum pockets. For $\eta \lesssim 1$, equilibrium configurations describing bound false vacuum pockets do not exist.

The scalar potential features the typical Mexican hat shape, with two minima in $h = \pm v$ and a maximum in $h = 0$. However, the presence of the fermionic condensate $S = \langle \bar{\psi}\psi \rangle$ effectively modifies the shape of the scalar potential (see Fig. 5.2). In particular, if the Yukawa coupling f is sufficiently strong (or the scalar quartic λ sufficiently small), the point $h = 0$ becomes an actual (local) minimum of the theory. The latter condition is mathematically formulated by requiring that the parameter $\eta = f/(2\lambda)^{1/4} \gtrsim 1$. In this regime, we show the existence of a bound NTS where the scalar field interpolates between $h = 0$ (false vacuum) and $h = v$ (true vacuum)[1], working in a fully relativistic approach.

The physical implication of the latter result is that, if $\eta \gtrsim 1$, a collection of N fermions is able to deform the $h \equiv v$ ground state, giving rise to NTSs that describe false vacuum pockets, in which the N fermions are trapped (see Fig. 5.1). The latter are unable to escape (at least classically) because their energy is lower than Nm_f, the rest energy of N free fermions (m_f is the fermion bare mass). Thus, the energy of an everywhere uniform configuration $h \approx v$ becomes higher than the energy of a configuration that shows false vacuum pockets here and there. Since NTSs are intrinsically non-perturbative states (see Sec. 5.3), the ground state of the system acquires a nontrivial scalar profile by means of non-perturbative effects. We dub this mechanism *non-perturbative vacuum scalarization.*

Investigations in a similar spirit were recently carried out by ref. [75] in the context of exotic neutron stars.

---

[1] Without loss of generality, we are assuming that the asymptotic (scalar) ground state of the Universe is $h = v$. One can also consider a solitonic solution that connects $h = 0$ with $h = -v$, but then we would have a topological soliton (because the asymptotic value of the scalar field in the solution would be different from its value in the rest of the Universe).

5.2 Model for relativistic NTSs

Our starting point is the following theory, in which a (real) scalar boson h and a Dirac fermion ψ are minimally coupled to Einstein gravity[2],

$$\mathcal{L} = \frac{R}{16\pi G} - \frac{1}{2}\partial_\mu h \partial^\mu h - \bar{\psi}\gamma^\mu D_\mu \psi - U(h) - \frac{f}{\sqrt{2}} h\, \bar{\psi}\psi, \tag{5.1}$$

where the scalar potential is (see Fig. 5.2 for $\eta = 0$)

$$U(h) = \frac{\lambda}{16}\left(h^2 - v^2\right)^2. \tag{5.2}$$

Performing spontaneous symmetry breaking $h \to h + v$ in the Lagrangian (5.1) gives rise to a well-defined scalar mass term,

$$m_h^2 = \frac{\lambda v^2}{2}. \tag{5.3}$$

However, for clarity of exposition, we prefer to work directly with (5.1), which has a simpler analytical expression. The Yukawa interaction is controlled by the coupling f, giving an effective mass to the fermion,

$$m_{\text{eff}} = \frac{f}{\sqrt{2}} h. \tag{5.4}$$

It is also useful to define

$$m_f = m_{\text{eff}}(h = v) = \frac{f}{\sqrt{2}} v, \tag{5.5}$$

which is the effective fermion mass when the scalar sits on the minimum $v > 0$.

The fermionic field has a $U(1)$ global symmetry which ensures the conservation of the fermion number N (the Noether charge).

Our setup is similar to that of the previous chapters. An important difference is that here we relax the fine-tuning of the Yukawa coupling f previously imposed (see sec. 3.1 and sec. 4.1), which allows us to explore connections with more realistic particle-physics content, as later discussed.

We will consider spherically symmetric equilibrium configurations, whose background metric can be expressed as

$$\mathrm{d}s^2 = -e^{2u(\rho)}\mathrm{d}t^2 + e^{2v(\rho)}\mathrm{d}\rho^2 + \rho^2(\mathrm{d}\theta^2 + \sin^2\theta\,\mathrm{d}\varphi^2), \tag{5.6}$$

in terms of two real metric functions $u(\rho)$ and $v(\rho)$.

As previously stated, fermions are treated through the Thomas-Fermi approximation (see 3.1.1), practically meaning that they enter Einstein's equations as a perfect fluid characterized by an energy-momentum tensor of the form

$$T_{\mu\nu}^{[f]} = (W + P)u_\mu u_\nu + P g_{\mu\nu}, \tag{5.7}$$

---

[2] We use the signature $(-,+,+,+)$ for the metric and adopt natural units ($\hbar = c = 1$). With the normalization used for the fermionic kinetic term, the Dirac matrices have an extra $-i$ factor with respect to the usual ones but satisfy the usual relation $\{\gamma^\mu, \gamma^\mu\} = 2g^{\mu\nu}$. The covariant derivative D_μ takes into account the spin connection of the fermionic field. We are neglecting interactions with gauge fields, but it is straightforward to generalize our model including them.

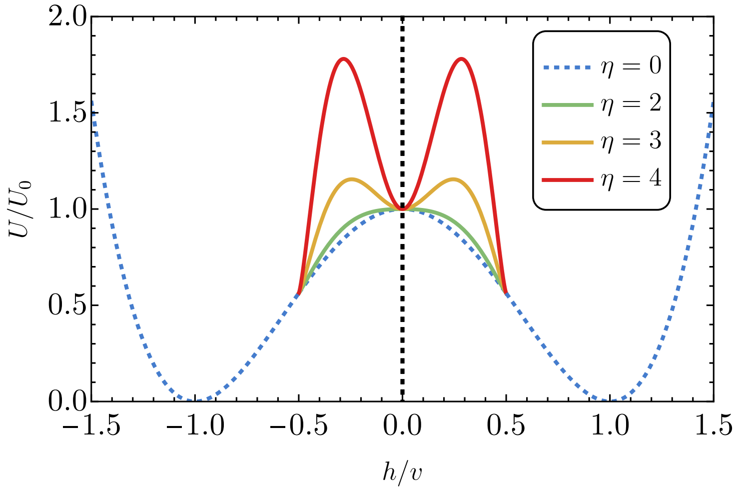

Figure 5.2. Effective scalar potential (see eq. (5.16)) normalized with respect to $U_0 = \lambda v^4/16$ as a function of h/v for various values of η in the Newtonian regime. In this regime, the zeros of the Fermi momentum are $h/v = \pm\tilde{\omega}_{\mathrm{F}}$ (for $|h|/v > \tilde{\omega}_{\mathrm{F}}$ the fermions are removed from the theory). We fixed a representative value $\tilde{\omega}_{\mathrm{F}} = 0.5$. We notice that when $\eta \gtrsim 1$ the effective potential develops a local minimum in $h = 0$. The shape of the potential is qualitatively the same even in the fully relativistic regime.

where W is the energy density and P is the pressure of the fluid, while they also enter the scalar field equation through the scalar density S, defined in sec. 3.1.1.

The fermion fluid is fully characterized once the Fermi momentum k_{F} is given. Within the Thomas-Fermi approximation, it can be shown that (see 3.1.1)

$$k_{\mathrm{F}}^2(\rho) = \omega_{\mathrm{F}}^2 e^{-2u(\rho)} - m_{\mathrm{eff}}^2 \,, \tag{5.8}$$

where ω_{F} is the Fermi energy at the origin ($\rho = 0$), which can be written in terms of the fermion central pressure $P(\rho = 0) \equiv P_c$ (see sec. 3.1.2 for details).

Analogously to what we did in sec. 3.1.2, it is convenient to introduce the dimensionless quantities

$$x = \frac{k_{\mathrm{F}}}{m_f}, \quad y = \frac{h}{v}, \quad r = m_h \rho \,, \quad \tilde{\omega}_{\mathrm{F}} = \frac{\omega_{\mathrm{F}}}{m_f} \,, \tag{5.9}$$

in terms of which the potential U and kinetic $V = \frac{1}{2} e^{-2v(\rho)} (\partial_\rho h)^2$ terms can be written as

$$U \equiv \mu^2 v_{\mathrm{F}}^2 \, \tilde{U}(y) \,, \qquad V \equiv \mu^2 v_{\mathrm{F}}^2 \, \tilde{V}(y). \tag{5.10}$$

Moreover, we introduce the following dimensionless fermionic quantities

$$\tilde{W} = \frac{W}{m_f^4}, \qquad \tilde{P} = \frac{P}{m_f^4}, \qquad \tilde{S} = \frac{S}{m_f^3}. \tag{5.11}$$

Finally, the field equations (i.e. the Einstein-Klein-Gordon equations with the addition of the Fermi momentum equation) take the compact form

$$
\begin{aligned}
&e^{-2v}-1-2e^{-2v}r\partial_r v=-\Lambda^2 r^2\left[\eta^4\tilde{W}+\tilde{U}+\tilde{V}\right],\\
&e^{-2v}-1+2e^{-2v}r\partial_r u=\Lambda^2 r^2\left[\eta^4\tilde{P}-\tilde{U}+\tilde{V}\ \right],\\
&e^{-2v}\Big[\partial_r^2 y+\Big(\partial_r u-\partial_r v+\frac{2}{r}\Big)\partial_r y\Big]-\frac{\partial\tilde{U}}{\partial y}-\eta^4\tilde{S}=0,\\
&x^2=\tilde{\omega}_{\mathrm{F}}^2 e^{-2u(r)}-y^2,
\end{aligned}
\tag{5.12}
$$

where $\tilde{U}$, $\tilde{V}$, $\tilde{P}$, $\tilde{W}$, and $\tilde{S}$ depend on x, y, and r. The above equations contain two dimensionless combinations of the parameters[3]

$$
\Lambda=\frac{\sqrt{8\pi}v}{m_p},\qquad \eta=\frac{f}{(2\lambda)^{1/4}}=\frac{m_f}{m_h^{1/2}v^{1/2}}\,,
\tag{5.13}
$$

the physical interpretation of which will be discussed in the next section.

NTSs in the model (5.1) are static and spherically symmetric solutions to the above system of ordinary differential equations. The boundary conditions are the same as those used in sec. 3.1.2, but in the present case[4] $y(r=0)=\epsilon$, where ϵ is the initial displacement with respect to the false vacuum $y=0$. The numerical procedure to build these solutions is the same as in sec. 3.3.1, to which we refer for more details.

Considering more than one Dirac fermion or including Majorana fermions in eq. (5.1) is a straightforward generalization. In the Thomas-Fermi approximation, this simply requires associating a Fermi momentum to each fermionic component and adding the relative energy density, pressure, and scalar density to the equations.

5.3 Properties and interpretation

Before presenting the numerical results, it is useful to discuss some general properties of these solutions.

The NTSs arising from eq. (5.1) are essentially fermion soliton stars with an effective positive cosmological constant inside, studied in the previous chapter. Therein, it was found that the energy of these solutions gets two contributions: one from the volume energy of the field and the other from a surface term (see sec. 4.1.1). The relative importance of these two terms depends on the actual region of the parameter space.

In a field theory with spontaneous symmetry breaking, it is reasonable to expect $v\ll m_p$, which also guarantees that quantum gravity effects can be safely neglected. From eq. (5.13), this implies $\Lambda\ll 1$, which corresponds to the regime where the energy is dominated by the volume contribution (see also eq. (4.15)). In this regime both the mass and the radius scale as $1/\Lambda$, while the parameter $\tilde{\omega}_{\mathrm{F}}$ scales as $1/\eta$.

---

[3] If we work in units such that $c=1,\hbar\neq 1$, η has dimensions of the square root of a coupling, i.e. $[\eta]=\hbar^{-1/4}$.

[4] In the absence of fermions, there is also a solitonic solution that connects the two minima of the potential ($h=\pm v$). This configuration represents a domain wall (which is a topological soliton) [76].

Moreover, the binding energy $E_B = M - m_f N$ of a configuration with N trapped fermions scales as (see sec. 4.1.3)

$$\frac{m_h E_B}{m_p^2} \sim \frac{1}{\Lambda}\Big(1-\eta\Big). \tag{5.14}$$

Thus, for fixed $\Lambda \ll 1$, the dimensionless binding energy is a linear decreasing function of η. Consequently, the bigger η the more bound the configurations[5], with $\eta \approx 1$ marking the transition from bound to unbound states. As we will discuss in detail later, for $\eta \lesssim 1$ the false vacuum pockets indeed disappear, and so does the nontrivial scalar profile of the ground state. Heuristically, this happens because the system has no benefit in investing some of its energy to build a false vacuum pocket to trap fermions that have a small mass gap between the two vacua of the scalar field. On the other hand, when $\eta \gtrsim 1$ the mass gap is big enough that it becomes energetically convenient to confine fermions in false vacuum pockets. For this reason, we will call the region

$$\eta \gtrsim 1\,, \tag{5.15}$$

confining regime[6] (in analogy to what was done in sec. 4.1.2). Moreover, the latter condition ensures that the point $h = 0$ in eq. (5.2) becomes a local minimum. Indeed, the effective scalar potential arising from eq. (5.1) is

$$\frac{U_{\rm eff}}{U_0} = \left(y^2 - 1^2\right)^2 + 8\,\eta^4 \tilde{S}\,y\,, \tag{5.16}$$

where $U_0 = \lambda v^4/16$. In order to analyze the behavior of the potential around the origin $y = 0$, we compute

$$\Big(\frac{U_{\rm eff}}{U_0}\Big)''(y=0) = \frac{8\eta^4\tilde{\omega}_{\rm F}^2}{\pi^2} - 4\,. \tag{5.17}$$

Thus, the point $y = 0$ will be a local minimum of the potential only if

$$\Big(\frac{U_{\rm eff}}{U_0}\Big)''(y=0) > 0\,, \tag{5.18}$$

which in turn yields

$$\tilde{\omega}_{\rm F} > \frac{\pi}{\sqrt{2}\,\eta^2}\,. \tag{5.19}$$

Using the fact that $\tilde{\omega}_{\rm F} \sim 1/\eta$, one gets again eq. (5.15). In Fig. 5.2 we explicitly show the behavior of the effective potential for different values of η in the Newtonian regime, where the fermion scalar density S is analytically expressed as a function of y only.

It is important to stress that the NTSs discussed here are genuinely non-perturbative states. Indeed, in the limit in which one of the relevant couplings (λ or f) is sent to zero, the energy diverges. When $\lambda \to 0$, this happens because

---

[5] This behavior could be modified by quantum corrections (see [77, 78] for investigations along this line in the absence of gravity).

[6] In units such that $c = 1, \hbar \neq 1$, the perturbativity bound is $\hbar^{1/4}\eta \lesssim \sqrt{4\pi} \sim O(1)$. Restoring natural units, the condition (5.15) corresponds to a strongly-coupled theory.

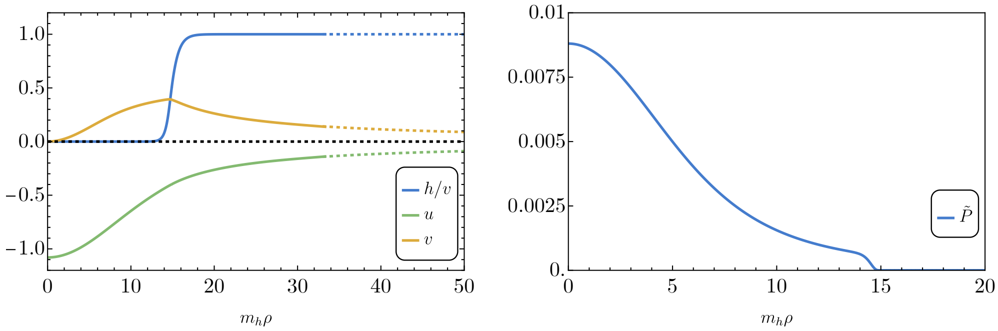

Figure 5.3. Radial profiles of scalar field h, normalized with respect to v, metric functions u, v (left panel), and fermion pressure (right panel) for a typical configuration ($\Lambda = 0.075$, $\eta = 4$). Continuous lines represent numerical data, whereas dashed lines reconstruct the asymptotic behavior of the solution by fitting with the Schwarzschild spacetime. The mass and radius of this configuration are $m_h M/m_p^2 \approx 4.08$ and $m_h R \approx 14.96$, the compactness is $C \approx 0.27$, while the solution parameters are $\tilde{P}_c = 8.8 \times 10^{-3}$ and $\log_{10} \epsilon = -19.00$. The binding energy is $m_h E_B/m_p^2 \approx -5.10$.

$\eta \to \infty$. When $f \to 0$, instead, the fermion mass vanishes (and so does the mass gap) and consequently the hydrostatic equilibrium implies $h \to v$ (see sec. 5.3.1), as already anticipated from the previous heuristic argument. Therefore, NTSs arising from eq. (3.1) actually become standard fermion stars [33] made of nearly massless fermions. In the zero-mass limit, the configuration does not have a finite radius and its energy diverges. In both cases, it is impossible to describe these solutions perturbatively around $f \approx 0$ or $\lambda \approx 0$.

Notice that if the two vacuum states are degenerate, whenever $\Lambda \ll 1$ there is no need for a strongly coupled fermion since the confining regime is achieved as long as $\eta \gtrsim \Lambda^{1/2}$ (see sec. 3.2.2), so η can also be small. Indeed, in the latter case, the volume density of the scalar is zero, and the system needs much less energy to form a false vacuum pocket.

Finally, we highlight that our semi-classical approach, in which the scalar field is described as a classical solution (while quantum effects are taken into account for fermions), is valid whenever the scalar self-interactions are weak, i.e. $\lambda \lesssim (4\pi)^2$.

5.3.1 Numerical results

In Fig. 5.3 we show an example of a solution with the radial profiles for the metric, scalar field, and fermion pressure.

In Fig. 5.4 we present the mass-radius and compactness-mass diagrams for various values of η in the confining regime $\eta \gtrsim 1$. As anticipated, we observe that the mass-radius diagram is very weakly dependent on η. Moreover, the compactness becomes arbitrarily small along the tail of the mass-radius diagram, giving rise to a Newtonian regime.

In Fig. 5.5 (left panel), we show the rescaled mass $M\Lambda$ and rescaled radius $R\Lambda$, confirming the expected scaling in the $\Lambda \ll 1$ limit. Overall, the mass-radius diagram is qualitatively similar to that of strange (quark) stars [65, 22].

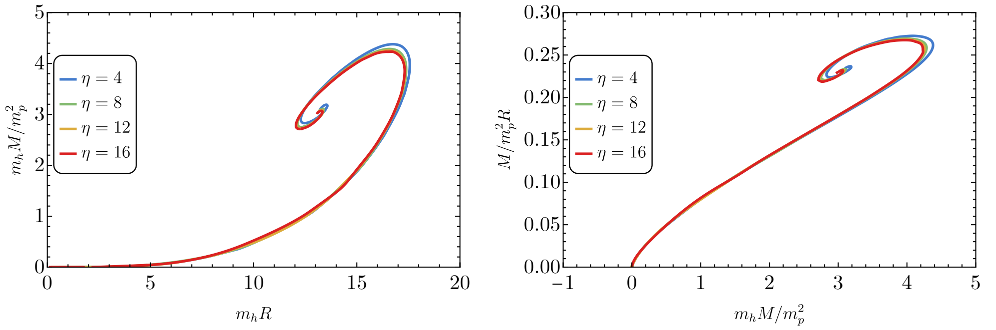

Figure 5.4. Mass-radius (left panel) and compactness-mass (right panel) diagrams for various values of η. We fixed $\Lambda = 0.075$. Varying Λ does not change the results qualitatively. There exists a turning point in the M-R diagrams at low masses, which cannot be seen from the figure, that proceeds towards the Newtonian limit of small M and large R, similarly to what already shown in sec. 3.3.3.

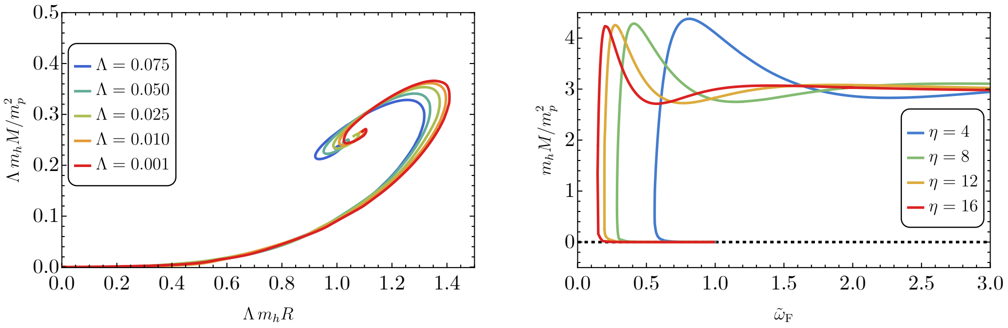

Figure 5.5. *Left panel:* Rescaled mass-radius diagrams for various Λ. We fix $\eta = 4$. Varying η does not produce appreciable changes as long as we stay in the confining regime $\eta \gtrsim 1$. As expected, there is an approximate scaling law as $\sim 1/\Lambda$, which becomes more and more accurate as $\Lambda \to 0$. *Right panel:* Mass as a function of $\tilde{\omega}_{\mathrm{F}}$ for various values of η. We fixed $\Lambda = 0.075$. Varying Λ does not change the results qualitatively. Notice the existence of a minimum value for $\tilde{\omega}_{\mathrm{F}}$ at any given η.

It is straightforward to identify a critical mass M_c (and corresponding radius R_c) as the point of maximum mass in the M-R diagram. As confirmed in Fig. 5.5, for $\Lambda \lesssim 0.1$ those quantities behave according to

$$\frac{m_h M_c}{m_p^2} = A(\eta)\,\frac{1}{\Lambda}, \qquad m_h R_c = B(\eta)\,\frac{1}{\Lambda}. \tag{5.20}$$

As shown in Fig. 5.4, in the confining regime the dependence of the critical quantities on η is very weak. Thus, A and B are approximately constant, and numerical fits show that $A \approx 0.36$ and $B \approx 1.35$. We therefore obtain

$$M_c \approx M_\odot \Big(\frac{0.34\,\mathrm{GeV}}{q}\Big)^2, \quad R_c \approx 5.5\,\mathrm{km} \Big(\frac{0.34\,\mathrm{GeV}}{q}\Big)^2, \tag{5.21}$$

where $q = (m_h v)^{1/2}$, in terms of which the condition (5.15) can be written as

$$m_f \gtrsim q. \tag{5.22}$$

Finally, the compactness of the critical configuration is $GM_c/R_c \sim A/B \sim 0.27$, slightly higher than that of a typical neutron star.

In Fig. 5.5 (right panel) we plot the mass as a function of $\tilde{\omega}_{\mathrm{F}}$ for various values of η at fixed $\Lambda = 0.075$, in the confining regime. In the low-mass region of these curves, where $m_h M/m_p^2 \approx 0$, $\tilde{\omega}_{\mathrm{F}} \to 1$. In that limit $\epsilon \to 1$, the fluid energy density (together with its number density) vanishes and thus the false vacuum pocket is lost. As long as we depart from the $m_h M/m_p^2 \approx 0$ branch, ϵ becomes a small number and the false vacuum pocket is recovered. From Fig. 5.5 (right panel) we also notice that, for any given η, $\tilde{\omega}_{\mathrm{F}}$ cannot be arbitrarily small. This means that configurations in which ϵ is small (i.e. truly false vacuum pockets) exist only above a minimum value $\tilde{\omega}_{\mathrm{F}}^{\min}$. We numerically verified that the scaling for $\tilde{\omega}_{\mathrm{F}}^{\min}$ is

$$\tilde{\omega}_{\mathrm{F}}^{\min} \approx \frac{2}{\eta}\,. \tag{5.23}$$

Notice that this quantity is independent of Λ. Since the number density n in the core is proportional to ω_{F}^3 (see sec. 4.1.2) for further details), we estimate

$$n^{\min} \approx \frac{1}{3\pi^2} m_f^3 \, (\tilde{\omega}_{\mathrm{F}}^{\min})^3 \approx \frac{8}{3\pi^2} (m_h v)^{3/2}\,. \tag{5.24}$$

The latter quantity can be interpreted as the minimum Noether charge per unit volume that allows for the existence of false vacuum pockets in the model (5.1). The configuration with the minimum possible Noether charge density has some peculiar properties. Calling $M_{\min}$ and $R_{\min}$, respectively, its mass and radius, numerical analysis shows that

$$\frac{m_h M_{\min}}{m_p^2} \approx 1.00, \qquad m_h R_{\min} \approx \frac{2.24}{\Lambda^{2/3}}. \tag{5.25}$$

Hence, in the $\Lambda \ll 1$ limit this special configuration is pushed towards the tail of the mass-radius diagram, where the compactness $G\,M_{\min}/R_{\min} \sim \Lambda^{2/3} \to 0$. We conclude that NTSs arising from eq. (5.1) scan a range of masses and radii starting from the configuration in eq. (5.25) deep in the tail of the mass-radius diagram, where relativistic gravitational effects are negligible, up to the critical configuration in eq. (5.21), above which the NTS is expected to undergo gravitational collapse.

In Fig. 5.6, we show the initial displacement ϵ and the binding energy of the configurations as a function of η. As expected from the discussion in Sec. 5.3, the bigger is η the lower the binding energy. In particular, we observe that the binding energy of the critical configurations, marked with a violet dot in Fig. 5.6, decreases linearly in η, as expected. Around $\eta \approx 1$, we find configurations with positive binding energy, in agreement with the estimate in eq. (5.14).

From the left panel of Fig. 5.6, we observe that the bigger is η, the lower the displacement ϵ, whereas, for $\eta \approx 1$, the displacement is $\epsilon \approx 1$, meaning that the scalar field is practically already on the true vacuum. In the latter case, as anticipated from the discussion in Sec. 5.3, the effective fermion mass is already very near to m_f and the picture of the configuration as a false vacuum pocket is lost. Therefore, we confirm that the ground state acquires a non-trivial scalar profile only if η is above a particular threshold. The numerical analysis done within the Thomas-Fermi

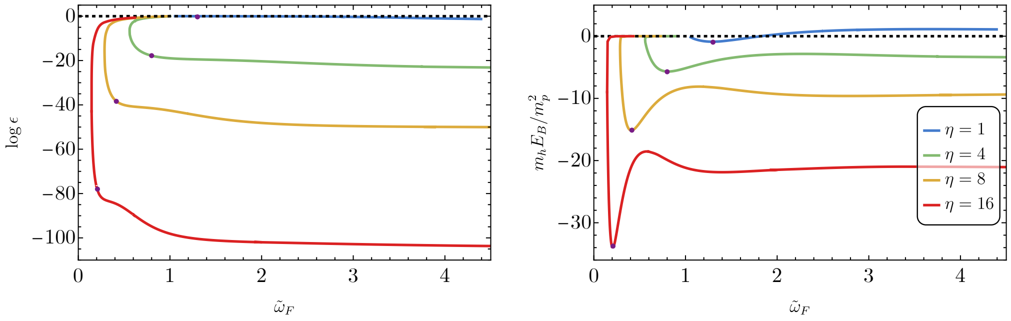

Figure 5.6. The initial displacement (left panel) and binding energy (right panel) for various values of η. We fixed $\Lambda = 0.075$. Varying Λ does not change the results qualitatively. As expected, the bigger η, the lower the binding energy. The configurations corresponding to the critical ones are highlighted with a violet marker.

approximation shows that already with $\eta \lesssim 2$ we enter the deconfining regime (with the appearance of several turning points in both the mass and the radius, similarly to what is shown in sec. 3.3.3) and for $\eta = 1$ all the configurations with $E_B < 0$ have $h \approx v$.

5.3.2 Stability of NTSs

There are three main independent mechanisms through which a NTS may decay in time. First of all, if the binding energy is positive, a configuration with N fermions trapped inside is triggered to disperse into free N particles by quantum and/or thermal fluctuations [79]. As discussed in Sec. 5.3.1, as long as eq. (5.22) is satisfied, the configurations are bound.

Second, NTSs may be unstable under classical perturbations. A full investigation of the latter point goes beyond the scope of this work. However, in the confining regime, the shape of the mass-radius diagram is qualitatively similar to that of strange (quark) stars [65, 22]. Therefore, we expect the configurations below the critical mass to be at least radially stable, as it happens for ordinary stars [61].

Third, the configurations could be unstable under fission into smaller configurations. Calling $E(N)$ the energy of a NTS with N trapped particles inside, whenever

$$E(N_1) + E(N_2) > E(N_1 + N_2) \tag{5.26}$$

fission is forbidden. The above equation can be recast in the following condition (also known as the Vakhitov–Kolokolov stability criterion [80, 81])

$$\frac{d^2E}{dN^2} < 0\,. \tag{5.27}$$

For the configurations laying below the critical mass, we numerically checked that eq. (5.27) holds.

5.4 Applications of the model

In this section, we discuss explicit realizations of the model under investigation, embedded in various theories.

5.4.1 Neutron soliton stars

A simple application of non-perturbative vacuum scalarization is in the context of the linear sigma model [82], a low-energy effective theory of QCD that implements spontaneous chiral symmetry breaking. In this context, the fermion in eq. (5.1) is just a nucleon, while the scalar field is a scalar meson called σ. Using the benchmark values $m_h \sim 500\,\mathrm{MeV}$ [83], $v \sim f_\pi \sim 130\,\mathrm{MeV}$ in eq. (5.25), the minimal configuration is estimated to be

$$M_{\rm min} \approx 10^{-19}\, M_\odot, \qquad R_{\rm min} \approx 1\,\mathrm{cm}, \tag{5.28}$$

while the critical one in eq. (5.21) is

$$M_c \approx 2\, M_\odot, \qquad R_c \approx 10\,\mathrm{km}, \tag{5.29}$$

with a compactness of $M_c/R_c \sim 0.27$, that is slightly larger than that of an ordinary neutron star. Moreover, being the mass of the nucleon $m_f \sim 1\,\mathrm{GeV}$, we get $\eta \approx 4$, ensuring that the configurations lay in the confining regime. These estimates are in agreement with the ones given in ref. [84].

Remarkably, the heaviest neutron stars discovered [85] have a mass compatible with the estimate in eq. (7.44). In the absence of a scalarization mechanism, it is well known that a standard degenerate Fermi gas of neutrons can support compact stars only up to $\sim 0.7 M_\odot$ [24], and nuclear interactions are therefore needed to explain heavy neutron stars. In our model, instead, we can achieve the same result by simply coupling the degenerate Fermi gas to a scalar field.

We are neglecting the energy density of the pions assuming that their mean values on the ground state are zero. However, they are inevitably present in the linear sigma model and the inclusion of a pion condensate could lead to interesting phenomenology [86]. Exploring these effects, however, would require a more involved analysis.

Our simple estimate suggests that the ground state of the heaviest neutron stars can in fact be scalarized and their core is made of a false vacuum pocket where the chiral symmetry is unbroken [75, 87]. Such NTSs may be formed in the early universe (see sec. 5.5), or during the merger of two neutron stars, if the energy involved is high enough ($\sim f_\pi$) to allow for the formation of false vacuum pockets and consequent trapping of nucleons.

5.4.2 Higgs false vacuum pockets

Non-perturbative vacuum scalarization may also play a role in the Higgs sector of the Standard Model (SM). Indeed, neglecting gauge interactions, eq. (5.1) naturally arises after electroweak symmetry breaking, as shown in Appendix B. In this scenario, h is the physical Higgs field and ψ a SM fermion. Using $m_h \sim 125\,\mathrm{GeV}$ and $v \sim 246\,\mathrm{GeV}$, the minimal configuration is found to be

$$M_{\text{min}} \approx 10^{-21}\, M_{\odot}, \qquad R_{\text{min}} \approx 0.2\,\mu\text{m}, \tag{5.30}$$

while the critical mass and radius are

$$M_c \approx (4 \times 10^{-6})\, M_{\odot}, \qquad R_c \approx 2\,\text{cm}. \tag{5.31}$$

These configurations are compelling candidates for non-particle dark matter and exotic compact objects. Indeed, it is intriguing to note that the critical mass range is naturally compatible with the OGLE+HSC observation of some microlensing events [88, 89]. However, non-perturbative vacuum scalarization occurs only if there is a strongly coupled fermion to the Higgs boson, that is, only if the condition in eq. (5.15) is satisfied. For the Higgs parameters, eq. (5.15) gives $m_f \gtrsim 175\,\mathrm{GeV}$, which is very near the top quark mass m_{top}. Nevertheless, as discussed in Sec. 5.3.1, numerical computations show that we need $\eta \gtrsim 2$ to form bound false vacuum pockets, meaning that m_f should be at least $\sim 350\,\mathrm{GeV}$. This suggests that non-perturbative vacuum scalarization does not occur in the SM[7]. In addition, even if the quark top mass was above the threshold, the electric charge carried by the fermions would produce a repulsive Coulomb force that in general renders large configurations unstable [91, 92]. Indeed, the total electric charge is estimated to be $Q \sim (2/3\,e)\, n\, R^3$. For the minimal configuration, this gives $Q_{\text{min}} \sim 10^{14}\,\mathrm{C}$, whereas for the critical one $Q_c \sim 10^{29}\,\mathrm{C}$. In both cases, the total electric charge is way above the maximum charge compatible with hydrostatic equilibrium [93], i.e. $10^{-22}\,\mathrm{C}$ for the minimal configuration, and $10^{-7}\,\mathrm{C}$ for the critical one.

However, top quarks also carry color charges. This gives a possible caveat to the previous arguments and leaves open the possibility of forming Higgs false vacuum pockets using only SM fields. To support the latter hypothesis, it is enough to estimate the fermion number density n inside the object. Using eq. (5.24), we obtain

$$n \sim m_f^3 \tilde{\omega}_{\text{F}}^3 \sim \frac{m_f^3}{\eta^3} \sim (m_h v)^{3/2}. \tag{5.32}$$

For the Higgs field parameters, $n \sim 7 \times 10^{47}\,\mathrm{cm}^{-3}$, which is orders of magnitude larger than the nuclear matter density, $n_{\text{nucl}} \sim 10^{38}\,\mathrm{cm}^{-3}$. Such high densities are expected to give rise to exotic states, in which interactions among fermions cannot be neglected anymore, such as a top/anti-top bound state [94] or a colored superconductor [95]. These scenarios could allow for bulk matter neutrality with respect to both electric and color charges. A self-consistent computation where eq. (5.7) is substituted by a new energy-momentum tensor, in which all these effects are taken into account, may lower the aforementioned threshold and allow for the existence of bound configurations.

Non-perturbative vacuum scalarization may naturally occur in extensions of the SM by a fourth generation of (heavy) fermions. However, the simplest models along

---

[7] A similar conclusion is found in ref. [90], where however the authors look for Higgs vacuum deformation around just one top quark (and not a collection thereof). Moreover, they neglect gauge interactions (and also gravity, since they are interested in microscopic states).

this direction are ruled out [96]. A viable possibility is adding only a fourth family of chiral leptons strongly coupled to the Higgs sector, without modifying the quark content. This would allow for evading bounds on the number of generations coming from the Higgs decay into gluons [96].

It is important to stress that, regardless of the particular beyond-SM context in which eq. (5.1) is obtained, as long as h is the Higgs boson, there are no free parameters in the model, being the mass and radius of the configurations very weakly dependent on m_f.

False vacuum pocket evaporation

Beyond the three standard mechanisms mentioned in Sec. 5.3.2, there could be other ways of destroying the object, depending on the specific embedding of the model. Here we mostly focus on the case of (compact) Higgs false-vacuum pockets, but the argument can be extended to other models in which the scalar h has Higgs-like couplings.

Let us assume that the fermions interact with (asymptotically) lighter SM particles (other than the Higgs boson). Inside the pocket, being the fermions effectively massless, their lifetime is expected to be extremely long. However, on the boundary of the pocket, the fermions re-acquire their mass and decays into lighter SM particles become kinetically allowed. Under the conservative assumption that all the decay products leave the pocket (effectively subtracting energy from the configuration), it is possible to give a rough estimate of the lifetime. The number of fermions in the boundary is $N^f_{\text{shell}} \sim m_h^{-1} R^2 \omega_{\text{F}}^3$, where m_h^{-1} is the size of the region where the fermions acquire their mass and ω_{F}^3 is the fermion number density. The number of fermions that leave the object per unit time is estimated as

$$\frac{dN^f_{\text{shell}}}{dt} \sim m_h^{-1} R^2 \omega_{\text{F}}^3 \times \Gamma(m_f \to \text{ something}). \tag{5.33}$$

A naive guess is $\Gamma(m_f \to \text{ something}) \sim m_f$. The latter estimate is conservative since we are assuming an $\mathcal{O}(1)$ interaction strength with the SM. Moreover, each fermion decay subtracts from the object an energy $\sim m_f$. Therefore, the total rate of energy loss is

$$\frac{dE_{\text{loss}}}{dt} \sim m_f \frac{dN^f_{\text{shell}}}{dt} \sim m_h^{-1} R^2 \omega_{\text{F}}^3 m_f^2. \tag{5.34}$$

The lifetime is estimated as

$$t_{\text{decay}} \sim \frac{M}{dE_{\text{loss}}/dt} \sim \frac{M}{m_h^{-1} R^2 \omega_{\text{F}}^3 m_f^2} \tag{5.35}$$

Since $M \sim m_p^2/m_h\Lambda$, $R \sim 1/m_h\Lambda$, $\omega_{\text{F}} = m_f \tilde{\omega}_{\text{F}} \sim m_f/\eta$, one finally gets

$$t_{\text{decay}} \sim \frac{m_p^2 m_h^2 \, \Lambda \, \eta^3}{m_f^5} \times \frac{v^2}{v^2} = \frac{1}{\Lambda\eta} \frac{1}{m_f} \sim \frac{\tilde{N}^{1/3}}{m_f} \tag{5.36}$$

We notice that in the limit $N \to \infty$ the lifetime would be infinity. Now,

$$t_{\text{decay}} \sim \frac{1}{\Lambda\eta} \frac{1}{\eta} \frac{1}{\sqrt{m_h v}} \sim \frac{1}{\Lambda \, \eta^2} \, 10^{-27} \, \text{sec} \tag{5.37}$$

Using the Higgs parameters, one gets $\Lambda \sim 10^{-16}$ and

$$t_{\mathrm{decay}} \sim \frac{10^{-11}\,\mathrm{sec}}{\eta^2}. \tag{5.38}$$

The actual computation of the lifetime should be carried out using a background field method (see e.g. ref. [97]) and is complicated by the fact that we are in a regime of strong gravitational field[8].

Moreover, several subtleties that can drastically change the latter estimate. First of all, our computation relies on the assumption that the fermions are a gas of weakly interacting particles. Conversely, if one adds sizeable interactions between fermionic particles, the lifetime may become much bigger, just like the lifetime of the neutron inside a nucleus could be bigger than the age of the Universe, whereas the lifetime of a free neutron is very short. Second, in a beyond-SM scenario, the decay into lighter SM particles can be forbidden if the fermions in the configuration possess extra symmetries (see e.g. [98]) or do not couple with other SM particles.

What can not be disentangled from the other SM content is the Higgs field. In principle, some Higgs quanta of the system may be converted into other SM particles, producing a net particle flux. Since the Higgs boson is in a non-linear wave configuration, computing the latter quantity is a non-trivial problem.

We give an estimate through the following argument. A NTS can be quantum mechanically described as a superposition of many coherent states (see e.g. [99]). Each soliton quantum represents an interacting state which has in principle nothing to do with the standard perturbative states of the theory. The soliton size R is set by the energy μ of these soliton quanta and the configuration is dominated by modes with momentum $k \lesssim \mu$. In particular,

$$R \sim \frac{1}{\mu}\,. \tag{5.39}$$

Since in our model $R \sim \frac{1}{m_h \Lambda}$, it is natural to estimate $\mu \sim m_h \Lambda \sim 10^{-14}\,\mathrm{GeV} = 10^{-5}\,\mathrm{eV}$. Therefore, just by energy conservation, the soliton quanta are not able to produce asymptotically a SM (massive) particle. Even neutrino (asymptotically) production is forbidden since $m_{\mathrm{neutrino}} \sim 10^{-2}\,\mathrm{eV} \gg \mu$.

What we cannot exclude is asymptotically photon production. However, since the Higgs boson does not couple to photons at the tree level, the overall effect is suppressed by loop effects. A rough estimate for the number of photons produced N_γ gives

$$\frac{dN_\gamma}{dt} \sim N_\mu \times \Gamma(\mu \to \gamma\gamma) \sim \frac{1}{\Lambda^4} \times \alpha^2 \mu \tag{5.40}$$

where α is the fine-structure constant and N_μ is the number of soliton quanta which is estimated to be $\sim m_h^2 v^2 R^3/\mu \sim 1/\Lambda^4$. Since the energy of each photon is $\sim \mu$, the change in the total energy is roughly $\mu\, dN_\gamma/dt$, which in turn gives the time needed to destroy the object

$$\frac{M}{\mu\, dN_\gamma/dt} \sim \frac{1}{\Lambda}\frac{1}{\alpha^2 m_h} \sim 10^{-6}\,\mathrm{sec}, \tag{5.41}$$

---

[8] We expect that strong gravity can only increase the lifetime of the object.

An important caveat of eq. (5.41) is that we are estimating the matrix element $\Gamma(\mu \to \gamma\gamma)$ as if the soliton quanta were the standard perturbative Higgs quanta of mass μ. However, we have already highlighted that the soliton quanta are purely interacting states which have nothing to do with the standard perturbative states. Therefore, a proper computation is needed to reliably estimate $\Gamma(\mu \to \gamma\gamma)$.

Accretion-driven collapse in the early Universe?

Even in those scenarios where the solitons evaporate (as in the case of the false-vacuum Higgs solitons), they might still play a role during the evolution of the Universe, for example, if they survive long enough to accrete a sizeable fraction of their mass.

Indeed, while for purely scalar solitons (such as boson stars) scalar accretion-driven collapse to a black hole is prevented by gravitational cooling [100, 54, 101], our solutions have a fermionic core which can undergo gravitational collapse upon accretion of ordinary matter.

In the simplest scenario, Higgs balls are produced in the radiation-dominated era with an initial mass M_i. In principle, such objects are able to accrete significantly before evaporation and one can therefore estimate the time needed to reach the critical mass M_c above which the object can collapse into a primordial black hole. Following Refs. [102, 103], we estimate the mass M of the object at the time t as

$$GM = \frac{t}{1 + \frac{t}{t_i}\left(\frac{t_i}{GM_i} - 1\right)}\,, \tag{5.42}$$

where t_i is the time of soliton formation and $t_i \gtrsim GM_i$ since M_i must be smaller than the horizon mass t_i/G. At $t \gg t_i$, the final mass asymptotically is

$$M \to \frac{M_i}{1 - GM_i/t_i}\,, \tag{5.43}$$

and can be significantly higher than M_i if $GM_i \sim t_i$.

Assuming that the object decays in a time t_d and requiring $M(t_d) > M_c$ for black-hole formation, we obtain

$$M_i > \frac{M_c}{1 + GM_c\left(\frac{1}{t_i} - \frac{1}{t_d}\right)} \sim \frac{M_c}{1 + \frac{GM_c}{t_i}}\,, \tag{5.44}$$

where the last step is valid if $t_d \gg t_i$.

For the case of the Higgs ball, we assume $M_c \sim 4 \times 10^{-6} M_\odot$, formation at the electroweak phase transition ($t_i \approx 2 \times 10^{-11}\,\mathrm{sec}$), and $t_d = t_i + t_{\mathrm{decay}}$, where t_{decay} is given in eq. 5.38. Therefore, for $\eta \approx 1$, these objects will collapse into black holes before evaporation only if

$$M_i \gtrsim 3 \times 10^{-6} M_\odot\,, \tag{5.45}$$

which is slightly smaller than the maximum mass and than the horizon mass at the time of formation.

The purpose of the previous estimates is to demonstrate the feasibility of black hole production by using NTSs as seeds to trigger gravitational collapse. Interestingly, this scenario would lead to the formation of PBHs with a mass determined by the maximum mass of the soliton, regardless of the formation epoch. However, further work is needed to translate these estimates into a concrete framework and to derive an actual prediction for the PBH abundance.

5.4.3 Dark soliton stars

The simplest beyond-SM scenario where non-perturbative vacuum scalarization is realized is in the context of the dark sector paradigm [104], where we interpret eq. (5.1) as embedded in the dark sector. The SM Higgs field $h_{\rm SM}$ interacts with the dark scalar h through the unavoidable scalar portal $\propto h_{\rm SM}^2 h^2, h_{\rm SM} h^2, h_{\rm SM}^2 h$. We assume $m_h \gtrsim m_{h_{\rm SM}}$, in order to kinematically forbid the Higgs boson direct decay into the dark scalar, allowing for evading collider constraints on the listed couplings.

In this framework, the evaporation bounds discussed in the previous section can be easily evaded. Indeed, assuming that ψ is the lightest fermion in the dark sector, decays on the boundaries are forbidden. Moreover, remembering that NTSs arising from eq. (5.1) are made of scalar quanta with characteristic energy $\mu \sim m_h \Lambda$, as long as

$$m_h \Lambda < m_{h_{\rm SM}} \sim 125\,{\rm GeV}\,, \tag{5.46}$$

the soliton quanta cannot produce asymptotically SM Higgs particles. Combining the latter equation with the requirement $m_h \gtrsim m_{h_{\rm SM}}$, we finally get

$$\Lambda < \frac{m_{h_{\rm SM}}}{m_h} \lesssim 1\,. \tag{5.47}$$

Since it is natural to assume $\Lambda \ll 1$, as discussed in Sec. 5.3, Eq (5.47) is easily satisfied even for a dark scalar much heavier than the SM Higgs boson.

If the scalar quartic λ is an $O(1)$ number, the condition $m_h \gtrsim m_{h_{\rm SM}}$ translates into $q \gtrsim q_{\rm SM} \approx 175\,{\rm GeV}$. Therefore, we conclude that these dark soliton stars are expected to be stable and support compact objects of masses naturally in the subsolar regime, according to eq. (5.21). In particular, for $m_h \sim v \sim 10^2\,{\rm GeV}$, we have a stable configuration with parameters similar to eq. (5.31).

The dynamical formation of NTSs arising in a similar framework has been recently studied in [57], through a first-order cosmological phase transition. The configurations produced, dubbed by the authors *Fermi balls*, are the non-relativistic limit of our solutions. If an initial distribution of Fermi balls is able to accrete and cool down, the final state will be a scalarized ground state (see **(c)** in Fig. 5.1), well-described by our solutions.

5.5 Hints at the possible formation mechanisms of NTSs

While we have not directly explored any dynamical formation channels, similar questions have already been addressed in the literature. The primordial formation for NTSs has been investigated by many authors (see e.g. [105, 106, 107, 108]), pointing out two main formation mechanisms, *solitosynthesis* and *solitogenesis*. In the former scenario, NTSs are formed by the fusion of N free fermions. This implies a non-zero cosmic asymmetry since it is necessary to accumulate a net number N

of fermions over antifermions in a given region of space. In the latter scenario, a relic abundance of NTSs is produced through a first- or second-order cosmological phase transition. Recently, ref. [108] reviewed these formation mechanisms in detail, showing that in certain cases NTSs can dominate the dark matter abundance. A further formation channel is provided from the Yukawa interaction present in eq. (5.1), as long as it is enough long-range. In this case, fermions undergo clustering and structure formation even in a radiation-dominated era [109, 110, 111].

5.6 Conclusions

In this chapter, we outlined the non-perturbative vacuum scalarization as a general mechanism to support new solitonic objects that can form in the early Universe and serve as dark matter candidates. For concreteness, we considered a theory with a real scalar field coupled to a fermion in the context of General Relativity and found solutions describing self-gravitating compact objects where the scalar field acquires a non-trivial profile due to non-perturbative effects. Remarkably, for natural model parameters between the QCD and the electroweak scale, this model predicts the existence of compact objects in the subsolar/solar range [3], which could be relevant for current and future LIGO-Virgo-KAGRA observations (see e.g. Refs. [112, 113]).

Besides the specific examples discussed in this work, other scenarios where this non-perturbative vacuum scalarization mechanism can play a role are fourth-generation models with extended Higgs sector [114], asymmetric dark matter models [12], mirror symmetries, minimal supersymmetric SM [115, 116], Type II see-saw mechanism [117], grand unified theories, inflation and cosmological phase transitions [118, 119]. Moreover, the inclusion of gauge fields into the solutions could give rise the important effects (see e.g. ref. [91, 92, 120]), which we plan to explore in future work.

Although NTSs are energetically favored and stable under (at least) radial perturbations, couplings to other fields or self-interactions might induce evaporation of the solution, the details of which depend on the specific embedding of the model in a given theory. Even in cases in which this time scale is short relative to typical astrophysical scales, in the early Universe NTSs might have enough time to accrete past the maximum mass or merge with other objects, with the possibility of forming primordial black holes in both cases [121, 58, 122, 123, 111, 124, 125]. Interestingly, this scenario would produce primordial black holes with a mass fixed in terms of the maximum mass of the soliton, regardless of the formation epoch. As we have shown, certain realizations of our model naturally lead to compact objects in a mass range that is compatible with the OGLE+HSC anomaly for some microlensing events [88, 89].

Chapter 6

Testing ECOs with gravitational waves: a short introduction

The detection of gravitational waves by LIGO [7] opened uncharted possibilities for testing the nature and properties of compact objects. The simplest sources of gravitational waves are binaries made of two compact objects (and indeed the first event detected was a binary of two black holes [7]). When the two objects are far apart, they are modeled as point masses orbiting each other under the force of gravity. This stage in the life of the binary is called *inspiral*. The evolution is conveniently described using a perturbative approach, such as the post-Newtonian (PN) expansion. As time goes by, the two objects become closer and closer, as the system gradually loses energy and angular momentum through the emission of gravitational waves. When the two objects come so close that their velocities approach the speed of light and the finite-size effects become dominant, perturbation theory breaks down and the binary enters the so-called *merger* phase, which is highly non-linear. Hence, fully numerical simulations are necessary to describe this stage. After the merger, the system is composed of a perturbed remnant, which oscillates according to characteristic frequencies. This stage is called *ringdown*. Finally, the system relaxes to a stationary configuration. In fig. 6.1, we present a pictorial illustration of a binary evolution throughout the three stages (inspiral, merger, and ringdown).

6.1 Sensitivity on ECO parameters

Consider a binary in circular orbit and let us call M_1 and M_2 the masses of the two objects. In the inspiral phase, the orbital frequency of this system is [19]

$$\nu = \frac{1}{2\pi}\sqrt{\frac{GM_{\rm tot}}{l_0^3}}\,, \tag{6.1}$$

where $M_{\rm tot} = M_1 + M_2$ is the total mass, and l_0 is the diameter of the circular orbit. The frequency f of the gravitational waves emitted is twice the orbital frequency [19], i.e.

$$f = \frac{1}{\pi}\sqrt{\frac{GM_{\rm tot}}{l_0^3}} \tag{6.2}$$

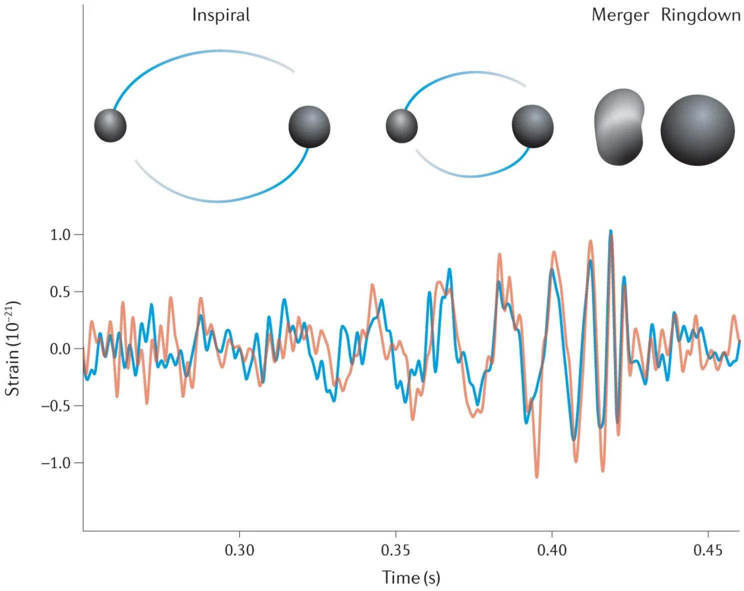

Figure 6.1. The gravitational-wave strain amplitude as a function of time for GW150914, detected at LIGO Hanford and Livingston observatories on September 14, 2015. In the top row, a pictorial illustration of the BH binary evolution throughout the three stages (inspiral, merger, and ringdown) is shown. Figure taken from ref. [126].

For a binary of two black holes, the end of the inspiral phase (or the beginning of the merger phase) is determined by the ISCO of the total system [127], i.e.

$$R_{\rm ISCO}^{BH} = 6\,GM_{\rm tot}\,. \tag{6.3}$$

The corresponding frequency deduced from eq. (6.2) is

$$f_{\rm ISCO}^{BH} = \frac{1}{6^{3/2}\pi\,GM_{\rm tot}}\,. \tag{6.4}$$

Numerical simulations show that the latter expression has to be corrected when the two black holes are highly spinning or the mass ratio M_1/M_2 is large. However, in this section we will always consider the case of nearly equal masses and low spins.

When the binary is made of two ECOs, we generalize eq. (6.4) as [31]

$$f_{\rm ISCO}^{ECO} = \frac{C^{3/2}}{3^{3/2}\pi\,GM_{\rm tot}}\,, \tag{6.5}$$

where C is the compactness (assumed to be the same for the two objects). This ansatz is corroborated by the study of the ISCO location for binaries of neutron stars [128]. Notice that when $C \to 1/2$ eq. (6.5) tends to eq. (6.4).

To detect the merger and ringdown phase of a binary involving ECOs, the characteristic frequency $f_{\rm ISCO}^{ECO}$ must fall within the sensitivity range of any of the present and future interferometers. For concreteness, we shall consider LIGO, Einstein Telescope (ET) and LISA. We show the relative frequency bands in table 6.1. For illustration purposes, we assume a binary of two equal mass ECOs ($M_1 = M_2 = M$), and we use eq. (6.5) to deduce the approximate regions in the parameter space

Table 6.1. Approximate GW frequency range of LIGO, ET and LISA.

LIGO	$f = [30 - 1000]\,\mathrm{Hz}$
ET	$f = [1 - 10^4]\,\mathrm{Hz}$
LISA	$f = [10^{-4} - 1]\,\mathrm{Hz}$

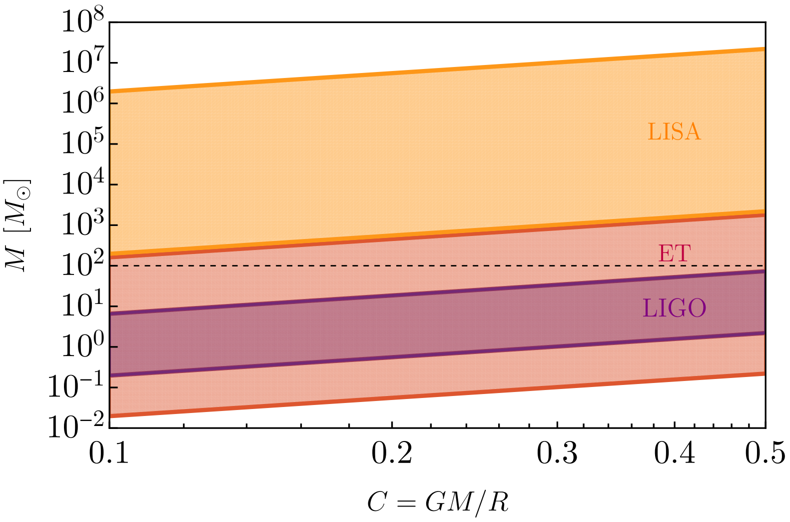

Figure 6.2. Approximate region of parameter space in the plane (C, M) probed by the interferometers LIGO, ET, and LISA. For illustration purposes, we have assumed a binary of two equal mass ECOs ($M_1 = M_2 = M$).

(C, M) that LIGO, ET and LISA probe. We show our results in fig. 6.2. Overall, we see that in the upcoming years we will be able to probe a large portion of the parameter space. Particularly intriguing is the so-called *subsolar range*, i.e. the region where $M \lesssim 1\,M_\odot$. Indeed, numerical simulations show that astrophysical black holes are heavier than $\sim 5\,M_\odot$ [129], whereas neutron stars lighter than $\sim [10^{-2} - 10^{-1}]\,M_\odot$ are unstable under explosion [130]. Therefore, the detection of a merger event involving a subsolar object lighter than $\sim 10^{-2}\,M_\odot$ would be the smoking gun for the discovery of new physics. Moreover, in the range $\sim [10^{-1} - 1]\,M_\odot$ tidal effects, as potentially already measurable during the ongoing O4 run of the LIGO/Virgo/Kagra (LVK) collaboration, can be used to rule out astrophysical origin [112].

As shown in fig. 6.2, ET will probe the subsolar range up to $\sim 10^{-2}\,M_\odot$. To go even further down, a second revolution in gravitational wave science will be necessary since the possibility of detecting such high-frequency gravitational waves is still under debate, although many proposals have been made (see e.g. ref. [131]).

Finally, observations of X-ray binary systems within the Milky Way suggest the existence of a lower mass gap between $\sim [3-5]\,M_\odot$ [132][1]. This is particularly intriguing because theoretical arguments exclude neutron stars heavier than $\sim 3\,M_\odot$ [134], whereas, as said, stellar black holes are expected to be heavier than $\sim 5\,M_\odot$ (this last statement is however delicate, being dependent on the assumptions upon which numerical simulations work). On the other hand, some of the detected LVK events (e.g., GW190814 [135] and GW230529 [136]) involve compact objects in the lower mass gap, the nature of which is still under study. This shows again how GWs offer amazing opportunities to shed light on the mystery of our Universe and probe the existence of exotic compact objects.

6.2 Binary inspiral

Once a waveform describing the merger of two compact objects is provided, it is reasonable to ask which observables are relevant to extract in order to constrain the nature and properties of the objects involved [137, 26]. The stage in the life of the binary where most of this information comes out is during the inspiral. As already mentioned, in the inspiral phase the dynamics is conveniently described through a post-Newtonian expansion. Adopting this framework, it is convenient to parametrize the Fourier-transformed GW signal as [26]

$$\tilde{h}(f) = \mathcal{A}(f)e^{i\psi}\,, \tag{6.6}$$

where f and $\mathcal{A}(f)$ are, respectively, the GW frequency and amplitude, whereas ψ is the phase of the signal.

At the lowest order (up to 1.5PN), the only parameters that enter the GW phase ψ are the masses of the two objects, and their dimensionless spins, while there is no dependence on the compactness of the components. Higher-order corrections (from 2PN) involve

- the *multipolar structure* of the bodies, which characterizes their inner structure [138, 139];
- *tidal Love numbers*, which quantify the way the bodies respond to the external gravitational field of their companion (see sec 6.2.2);
- *tidal heating*, which is essentially the amount of orbital energy dissipated by the binary due to tidal interactions (see e.g. ref [140]).

We will briefly illustrate the first two points in the following paragraphs, as they represent the most relevant quantities characterizing the internal structure of the inspiralling objects.

6.2.1 Multipolar structure

In a similar spirit to the multipolar expansion of the gravitational field in Newtonian gravity [141], the spacetime metric of a stationary isolated object can be expanded

---

[1] We used the adjective *lower* because there is also the so-called *upper mass gap*, between $\sim [50-120]\,M_\odot$, in which stellar evolution predicts the absence of black holes due to pair-instability supernovae (see e.g. ref. [133]).

in inverse powers of a suitable radial coordinate [142, 143]. The coefficients of this expansion are the multipole moments, which naturally split into two classes: the mass and current multipoles. We will call Q_L the mass multipole of order l and S_L the current multipole or order l, where L is a multi-index containing a number l of individual indices. It can be shown that when the spacetime is axially symmetric, the multipole moments reduce to scalar quantities Q_l, S_l [143].

Remarkably, BH no-hair and uniqueness theorems [144, 145, 143] enforce the multipole moments of any stationary black hole in isolation to be [26]

$$Q_l^{\mathrm{BH}} + iS_l^{\mathrm{BH}} = M^{l+1}(i\chi)^l \,, \tag{6.7}$$

where l is an integer, M is the mass of the BH and $\chi = J/M^2$ is the dimensionless spin (J is the angular momentum).

As already mentioned, during the inspiral stage the inner structure of the inspiralling bodies leaves its imprint on the dynamics through the multipole moments. In particular, the dominant effect is that of the spin-induced quadrupole moment Q_2 which yields a 2PN contribution to the phase [146, 26]. Therefore, multipole moments can be constrained with GW measures [147, 148]. Any deviation from the prediction in eq. (6.7) would signal departures from the Kerr metric. In general, measures of the multipole moments can be used to discriminate among different models of ECOs (see e.g. [41, 149]).

6.2.2 Tidal Love numbers

A robust analytical framework to understand tidal effects is encapsulated in the concept of tidal Love numbers (TLNs), which quantify the deformability properties of self-gravitating bodies [150]. Initially devised in the context of Newtonian gravity, TLNs have since been generalized in a fully relativistic context [151, 152, 153]. The basic idea is that when a self-gravitating body is immersed in an external gravitational field, the shape of the object will be consequently deformed, as pictorially shown in fig. 6.3. At first order, the multipolar deformation induced on the object will be linear in the strength of the external tidal field. The TLNs are then defined as the ratio between the induced multipole moments and the tidal moments of the external gravitational field:

$$Q_L = \lambda_l G_L, \qquad S_L = \sigma_l H_L, \qquad l \gtrsim 2 \,, \tag{6.8}$$

where λ_l (σ_l) is the electric (magnetic) tidal Love number. Here G_L (H_L) denotes the electric (magnetic) multipole moments of the external gravitational field.

The significance of TLNs has been particularly highlighted in the study of binary neutron star (NS) mergers, offering tantalizing prospects for constraining the equation of state (EOS) of dense matter through GW observations [154, 155, 156, 157, 158, 159, 160, 161, 162, 163, 164, 165, 166, 167, 168, 169, 170, 171, 172, 173, 174, 175, 176, 177, 178, 179, 180, 181] (see [182, 183] for reviews). Remarkably, these objects exhibit nearly EOS-independent relations between their moment of inertia, spin-induced quadrupole moment, and electric quadrupolar tidal deformability, which are found to hold with about 1% accuracy [184, 185, 186]. A similar approximate universality exists between TLNs of different multipolar order and different parity [187, 188].

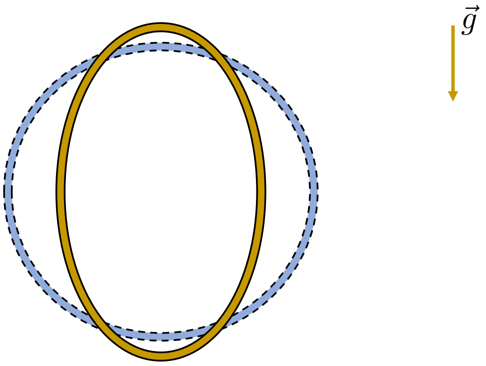

Figure 6.3. Pictorial representation of the induced multipole moments on the deformed objects (the orange ellipse) by an external gravitational field $\vec{g}$. The unperturbed object is represented by the blue circle.

The TLNs have also been studied in the context of asymptotically flat black holes (BHs), with the intriguing finding that, in general relativity, they vanish in the limit of static external perturbations for BHs in isolation [152, 153, 189, 190, 191, 192, 193, 194, 195, 196, 197, 198, 199, 200, 201, 202, 203, 204, 205]. However, this property is delicate, being violated for BH mimickers [206, 207], in the presence of a cosmological constant [208] or extended gravitational theories [207, 209, 210], in higher dimensions [211, 212, 213, 214, 215, 216] or in nonvacuum environments in the presence of secular effects, such as accretion or superradiant instabilities of ultralight bosonic fields [217, 218, 219, 220, 221, 222]. Furthermore, recently there has been an emerging interest in computing dynamical Love numbers [223, 224, 225, 226] and incorporating nonlinear effects [227, 228, 229].

The forthcoming next-generation ground-based GW detectors [230], such as the Einstein Telescope [231, 232] and Cosmic Explorer [233, 234], will improve the accuracy of measurements of tidal deformability [235, 180], potentially unveiling the existence of new physics in the gravitational signals [236].

6.3 Ringdown in a nutshell

6.3.1 Quasinormal modes

The last part in the binary lifetime is the ringdown phase, where the final remnant relaxes to a stationary state through the emission of GWs. The signal is conveniently described in perturbation theory as a superposition of waves $e^{i\omega t}$ with peculiar complex frequencies, i.e.

$$\omega = \omega_R + i\omega_I \, . \tag{6.9}$$

The presence of a non-zero imaginary part gives rise to damping in the signal (and it is linked to the emission of GWs). For this reason, these characteristic frequencies are called *quasinormal modes* (QNM) [237]. Their values form a discrete set and are therefore labeled by a set of integer numbers. Thanks to the uniqueness properties of Kerr black holes in vacuum [144, 145, 143], BH quasinormal modes are univocally determined just by mass and angular momentum. On the other hand, different types of compact objects will have different spectra (see e.g. refs. [238, 239, 240]). As those frequencies can be measured in the late part of the GW signal, QNMs offer an elegant way to test the nature of the final remnant and GR uniqueness theorems. This program goes under the name of *ECO spectroscopy*. While current detectors can only reliably extract one mode for massive BH mergers, future ones will detect more than one mode and really perform spectroscopy [241, 242].

6.3.2 Echoes

A striking feature of regular ECOs which possess a light ring (see sec. 2.4) is the emission of GW echos [243, 244]. During the ringdown, if the remnant does not have a horizon, the GW signal is partially reflected on the remnant's surface and goes back to the light ring in a time that depends on the remnant's compactness. As this scattering back and forward happens many times, a train of signals (the *echoes*) is produced. For a BH, this can not happen since the ingoing signal takes an infinite time to reach the horizon and gets completely absorbed. Therefore, echoes provide a quantitative test of the existence of a horizon after the merger [245].

Chapter 7

Tidal Love numbers of fermion soliton stars

Summary

In this chapter, we investigate the tidal deformations of fermion soliton stars (FSSs) and compute the corresponding tidal Love numbers for different model parameters. Furthermore, we discuss the existence of approximate universal relations for the electric and magnetic tidal deformabilities of these stars and compare them with other solutions of general relativity, such as neutron stars or boson stars. These relations for fermion soliton stars are less universal than for neutron stars, but they are sufficiently different from the ordinary neutron star case that a measurement of the electric and magnetic tidal Love numbers (as potentially achievable by next-generation gravitational wave detectors) can be used to disentangle these families of compact objects. Finally, we discuss the conditions for tidal disruption of fermion soliton stars in a binary system and estimate the detectability of the electromagnetic signal associated with such tidal disruption events.

7.1 Perturbations

The tidal deformabilities of compact objects can be computed using perturbation theory. This amounts to considering fluctuations in both the background metric and in the matter content of the theory, which in this case consists of the scalar and fermionic fields. The perturbed metric at first order reads

$$g_{\mu\nu} = \bar{g}_{\mu\nu} + h_{\mu\nu}\,, \tag{7.1}$$

where $\bar{g}_{\mu\nu}$ is the background spacetime metric and $h_{\mu\nu} \equiv \delta g_{\mu\nu}$ is a small tensorial perturbation. In the following, we use a bar superscript to denote the unperturbed quantities.

We assume that the perturbations are sourced by an external stationary tidal field (see sec. 7.2). Consequently, all the perturbations of the metric/fluid are independent of time.

The spherical symmetry of the background (see e.g. sec. 3.1.1) allows us to decompose the first-order perturbation $h_{\mu\nu}$ in spherical harmonics and to separate the perturbation into even and odd parity sectors, $h_{\mu\nu} = h^{\rm even}_{\mu\nu} + h^{\rm odd}_{\mu\nu}$. The even sector is often called *polar* or *electric*, while the odd one *axial* or *magnetic*. The gauge invariance of General Relativity can be used to impose four conditions on the metric perturbation and therefore simplify the final equations. A particularly convenient choice is the Regge-Wheeler gauge (see refs. [246, 19] for further details), where $h_{\mu\nu}$ is decomposed as

$$h^{\rm even}_{\mu\nu} = \begin{pmatrix} e^{2u} H_0^{lm}(\rho) Y^{lm} & H_1^{lm}(\rho) Y^{lm} & 0 & 0 \\ H_1^{lm}(\rho) Y^{lm} & e^{2v} H_2^{lm}(\rho) Y^{lm} & 0 & 0 \\ 0 & 0 & \rho^2 K^{lm}(\rho) Y^{lm} & 0 \\ 0 & 0 & 0 & \rho^2 \sin^2\theta K^{lm}(\rho) Y^{lm} \end{pmatrix}, \tag{7.2}$$

$$h^{\rm odd}_{\mu\nu} = \begin{pmatrix} 0 & 0 & h_0^{lm}(\rho) S_\theta^{lm} & h_0^{lm}(\rho) S_\varphi^{lm} \\ 0 & 0 & h_1^{lm}(\rho) S_\theta^{lm} & h_1^{lm}(\rho) S_\varphi^{lm} \\ h_0^{lm}(\rho) S_\theta^{lm} & h_1^{lm}(\rho) S_\theta^{lm} & 0 & 0 \\ h_0^{lm}(\rho) S_\varphi^{lm} & h_1^{lm}(\rho) S_\varphi^{lm} & 0 & 0 \end{pmatrix}, \tag{7.3}$$

with scalar and odd vector harmonics $\left(S_\theta^{lm}, S_\varphi^{lm}\right) \equiv \left(-Y^{lm}_{,\varphi}/\sin\theta,\, \sin\theta\, Y^{lm}_{,\theta}\right)$, and assuming an implicit sum over the angular indices l, m. Similarly, we decompose the fluid perturbations in spherical harmonics as $\delta X = X_1(\rho) Y^{lm}$, where δX indicates a given matter perturbation and $X_1(\rho)$ its radial dependence (omitting the multipole dependence on l, m and the sum over these indices). This results in an analogous decomposition for the fluid stress-energy tensor:

$$T_{\mu\nu} = \overline{T}_{\mu\nu} + \delta T_{\mu\nu}\,. \tag{7.4}$$

The corresponding Einstein equations then read $\delta G_{\mu\nu} = 8\pi G \delta T_{\mu\nu}$, in terms of the perturbed part of the Einstein tensor. Since the background spacetime is spherically symmetric, the two sectors are decoupled and can be solved independently.

In the following, we begin by discussing the matter content and then compute the metric perturbations in the two sectors.

7.1.1 Fermionic perturbations

By assuming that also the perturbed fluid is perfect (i.e., by neglecting anisotropic stress), one can introduce the perturbed quantities $W = \bar{W} + \delta W, P = \bar{P} + \delta P, u^\mu = \bar{u}^\mu + \delta u^\mu$, to get

$$\delta T^{[f]\mu}_{\nu} = (\delta W + \delta P)\bar{u}^\mu \bar{u}_\nu + (\bar{W} + \bar{P})(\delta u^\mu \bar{u}_\nu + \bar{u}^\mu \delta u_\nu) + \delta P \delta^\mu_\nu\,, \tag{7.5}$$

where the background four-velocity of the fluid is simply $\bar{u}^\mu = (e^{-u}, 0, 0, 0)$, while $\bar{u}_\mu = (-e^u, 0, 0, 0)$. It is important to stress that $\bar{u}^\mu \propto \delta^\mu_0$, so the only nonzero, nondiagonal elements of eq. (7.5) are the $0i$ components. On the other hand, in the presence of anisotropic stress, the ij contributions can also be different from zero.

Imposing $g_{\mu\nu}u^{\mu}u^{\nu} = -1$, one gets

$$\delta g_{\mu\nu}\bar{u}^{\mu}\bar{u}^{\nu} + 2\bar{g}_{\mu\nu}\bar{u}^{\mu}\delta u^{\nu} = 0 \Rightarrow \delta u^{0} = \frac{1}{2}e^{-3u}\delta g_{00}\,, \tag{7.6}$$

while $\delta u_0 = e^{-u}\delta g_{00}/2$. The tt-component of the fermionic perturbed energy-momentum tensor then reads

$$\begin{aligned}\delta T^{[f]0}_{0} &= -(\delta W + \delta P) + (\bar{W} + \bar{P})[\delta u^{0}(-e^{u}) \\ &\quad + e^{-u}\delta u_0] + \delta P = -\delta W\,. \end{aligned} \tag{7.7}$$

Similarly, it is straightforward to write down the remaining components of the perturbed stress-energy tensor:

$$\delta T^{[f]i}_{j} = \delta P \delta^{i}_{j} \tag{7.8}$$

$$\delta T^{[f]i}_{0} = -(\bar{W} + \bar{P})e^{u}\delta u^{i} \tag{7.9}$$

$$\delta T^{[f]0}_{i} = (\bar{W} + \bar{P})e^{-u}\delta u_{i}\,, \tag{7.10}$$

where $\delta u^{i} = d\xi^{i}/d\tau$, with ξ^{i} the spatial displacement of the fluid element due to the perturbations, and τ the proper time.

As discussed in ref. [247], in the zero-frequency limit of the time-dependent response to an external gravitational perturbation the perturbed fluid can either be static (i.e., characterized by zero three-velocity) or irrotational (i.e., characterized by zero vorticity). The latter is a more realistic assumption in a binary system, as discussed in Refs. [248, 247, 188]. Such different fluid configurations are found to impact the magnetic TLNs in both their sign and value, while the electric TLNs remain the same in both cases [247, 248]. Therefore, we write the spatial fluid velocity as [249]

$$\delta u^{i} = \{0, Q^{lm}(\rho)\, S^{lm}_{\theta}(\theta\,,\varphi), \frac{Q^{lm}(\rho)}{\sin\theta^{2}}\, S^{lm}_{\varphi}(\theta\,,\varphi)\}\,, \tag{7.11}$$

where $i = \rho, \theta, \varphi$ and

$$Q^{lm}(\rho) = -\frac{e^{-u}}{\rho^{2}}h^{lm}_{0}(\rho)\,, \tag{7.12}$$

as required to describe an irrotational fluid [250].

As already highlighted in the previous section, in the Thomas-Fermi approximation the fermionic fluid is fully characterized once the Fermi momentum $k_{\rm F}$ is given at each spacetime point. In the following we will assume a similar perturbative decomposition

$$k_{\rm F} = \bar{k}_{\rm F} + \delta k_{\rm F}\,. \tag{7.13}$$

Adopting the same decomposition also for the scalar field $\phi = \bar{\phi} + \delta\phi$, as discussed in the next subsection, we can write down $\delta W, \delta P, \delta S$ in terms of $\delta k_{\rm F}$ and $\delta\phi$, assuming that W, P, S can be computed as in the background case: see Eqs. (3.5), (3.6), and (3.7). This assumption is valid as long as the time scale of the tidal perturbation is much longer than that of the fundamental fermionic degrees of freedom, which is always the case.

In order to close the system of equations, we need a further condition that relates $\delta k_{\rm F}$ to the metric and scalar functions, analogous to eq. (3.19) for the background quantities. In principle, such a condition can be derived by generalizing the Thomas-Fermi approximation to a generic spacetime. This task can actually be accomplished by using the Einstein equations. In particular, adding up the $\theta\theta$ and $\varphi\varphi$ components gives δP as a function of H_0 and $\delta\phi$. We can also use eq. (3.6) to write

$$\delta P = \frac{\delta P}{\delta k_{\rm F}}\delta k_{\rm F} + \frac{\delta P}{\delta \phi}\delta\phi\,. \tag{7.14}$$

At this point we have two independent expressions for δP, which in turn gives δk_F as a function of metric, scalar, and background quantities only. In analogy with the background case, we therefore need to solve only the Einstein equations and the scalar field equation. The additional perturbations δW and δS are obtained by expanding Eqs. (3.5) and (3.7) as done in eq. (7.14). We give the explicit expressions in Appendix C.

7.1.2 Scalar perturbations

The energy-momentum tensor of a real scalar field reads

$$T^{[\phi]}_{\mu\nu} = \partial_\mu\phi\partial_\nu\phi - g_{\mu\nu}\left(\frac{1}{2}g^{\alpha\beta}\partial_\alpha\phi\partial_\beta\phi + U(\phi)\right)\,, \tag{7.15}$$

such that its perturbation becomes

$$\begin{aligned}\delta T^{[\phi]}_{\mu\nu} &= \partial_\mu\delta\phi\partial_\nu\bar{\phi} + \partial_\nu\delta\phi\partial_\mu\bar{\phi} - \delta g_{\mu\nu}\left(\frac{1}{2}\bar{g}^{\alpha\beta}\partial_\alpha\bar{\phi}\partial_\beta\bar{\phi} + U(\bar{\phi})\right)\\ &- \bar{g}_{\mu\nu}\left(\frac{1}{2}\delta g^{\alpha\beta}\partial_\alpha\bar{\phi}\partial_\beta\bar{\phi} + \bar{g}^{\alpha\sigma}\partial_\alpha\delta\phi\partial_\beta\bar{\phi} + \delta U\right)\,,\end{aligned} \tag{7.16}$$

where we have decomposed the scalar potential as $U(\phi) = U(\bar{\phi}) + \delta U$, and

$$\delta U = \frac{\partial U(\phi)}{\partial\phi}\Big|_{\bar{\phi}}\delta\phi\,. \tag{7.17}$$

7.1.3 Perturbation equations

We now turn to the solution of the linearized Einstein equations, focusing first on the polar sector and then on the axial sector.

Polar perturbations

Taking the difference between the $\theta\theta$ and $\varphi\varphi$ components reveals that $H_2(\rho) = H_0(\rho)$. From $\delta G^t_\rho = 8\pi G\delta T^t_\rho$ we get $H_1 \equiv 0$. Also, the $\rho\theta$ component can be used to relate K' to ϕ_1, H_0, and H_0' as follows:

$$K' = H_0' + 2H_0u' - 16\pi G\,\phi_1\phi_0'\,. \tag{7.18}$$

Finally, the difference between the $\rho\rho$ and tt components can be written as a master equation for H_0, with no further K dependence:

$$
\begin{aligned}
H_0'' &+ 8\pi G\, e^{2v}(P_1 + W_1) + \Big(\frac{2}{\rho} + u' - v'\Big) H_0' + 16\pi G \Big[(u' + v' - \frac{2}{\rho})\bar{\phi}' - \bar{\phi}''\Big]\phi_1 \\
&+ \Big[\frac{2}{\rho^2} - \frac{e^{2v}(l^2 + l + 2)}{\rho^2} + 16\pi G\, e^{2v}(\bar{P} + \bar{W} - \frac{1}{2}\bar{\phi}'^2 e^{-2v}) + \frac{4u'}{\rho} - 4u'^2\Big] H_0 = 0\,,
\end{aligned}
\tag{7.19}
$$

where P_1, W_1 and U_1 are the radial components of the matter perturbations δP, δW and δU after decomposition in spherical harmonics. The equation of motion for the scalar field reads

$$
\begin{aligned}
&\phi_1'' + \phi_1' \left(u' - v' + \frac{2}{\rho}\right) + H_0 \left[\left(u' + v' - \frac{2}{\rho}\right)\bar{\phi}' - \bar{\phi}''\right] \\
&- \left(\frac{l(l+1)e^{2v}}{\rho^2} + 16\pi G \bar{\phi}'^2\right)\phi_1 = e^{2v} \frac{\partial^2 U(\phi)}{\partial \phi^2}\Big|_{\bar{\phi}} \phi_1 - e^{2v} f S_1\,,
\end{aligned}
\tag{7.20}
$$

where, again, ϕ_1 is the radial component of the scalar field perturbation $\delta\phi$ after expansion in spherical harmonics.

Axial perturbations

The $\rho\varphi$ component of the perturbed Einstein equations implies $h_1 = 0$, and the $\rho\theta$ component implies $\phi_1 = 0$. We are therefore left with a single radial equation for the perturbed function h_0 (the $t\varphi$ component):

$$
h_0'' - (u' + v')\, h_0' + \frac{[2 - l(l+1)]e^{2v} - 2 + 2\rho(u' + v')}{\rho^2}\, h_0 = 0\,. \tag{7.21}
$$

We numerically solve all the perturbed equations by applying the transformation given in sec. 3.1.2, in analogy with what we did for the background equations.

7.2 Tidal Love numbers

Nonspinning, spherically symmetric, FSSs immersed in an external stationary tidal field will be deformed and develop a multipolar structure in response to the external field. This phenomenon may occur in coalescing binary systems, where each component tidally deforms its companion because of gravity. The assumption of a stationary field holds only in the early inspiral phase, when the orbital separation from the companion is very large and the orbit is slowly varying in time. Furthermore, one can make use of the approximation that the multipolar deformation induced on the objects is linear in the strength of the external tidal field to define the tidal Love numbers (see also sec. 6.2.2) as the ratio between the induced multipole moments and the tidal moments of the external gravitational field:

$$
Q_L = \lambda_l G_L, \qquad S_L = \sigma_l H_L, \qquad l \gtrsim 2\,. \tag{7.22}
$$

Here the symbols Q_L (S_L) denote the mass (current) multipole moments of order l of the object (L being a multi-index containing a number l of individual indices), and

G_L (H_L) the corresponding electric (magnetic) tidal multipole moments. In analogy with the electrostatic case, where the electrostatic potential can be expanded in multipole moments characterizing the shape of the charge distribution, the mass and current multipole moments in General Relativity are the coefficients of a proper asymptotic expansion of the metric components, characterizing the source of the gravitational field (see refs [142, 249] for further details.

The parameters λ_l (σ_l) are the electric (magnetic) tidal deformability, related to the dimensionless TLNs k_l^E (k_l^M) through the relations [151, 187, 249]

$$\begin{aligned} \lambda_l &= (GM)^{2l+1}\bar{\lambda}_l = \frac{2R^{2l+1}}{(2l-1)!!}k_l^E \,, \\ \sigma_l &= (GM)^{2l+1}\bar{\sigma}_l = \frac{(l-1)R^{2l+1}}{4(l+2)(2l-1)!!}k_l^M \,, \end{aligned} \qquad l \geq 2 \,, \tag{7.23}$$

in terms of the FSS mass M and radius R. The main contribution to the star's deformation comes from the quadrupole ($l = 2$), which will be the main focus of our analysis.

The TLNs can be extracted by asymptotically expanding the metric of the object, perturbed by the external tidal source, at spatial infinity. In asymptotically Cartesian mass-centered coordinates, the time-time and time-space components of the metric read

$$\begin{aligned} g_{00} =& -1 + \frac{2GM}{\rho} + \sum_{l\geq 2}\left[\frac{1}{\rho^{l+1}}\left(\frac{2(2l-1)!!}{l!}Q_L n_L\right) + \rho^l\left(\frac{2}{l!}G_L n_L\right)\right] \,, \\ g_{0i} =& \sum_{l\geq 2}\left[\frac{1}{\rho^{l+1}}\left(-\frac{4l(2l-1)!!}{(l+1)!}\epsilon_{ija_l}S_{jL-1}n_L\right) + \rho^l\left(\frac{l}{(l+1)!}\epsilon_{ija_l}H_{jL-1}n_L\right)\right] \,, \end{aligned} \tag{7.24}$$

where $n_i = x_i/\rho$ is the unit radial vector, $n_L = n^{a_1}\dots n^{a_l}$, and we absorb any factor of G in the definition of Q_L, S_L [142, 249]. For simplicity, we have neglected terms independent of ρ and proportional to spherical harmonics of order $l' < l$. In this coordinate frame, the mass dipole of the object vanishes identically. From this expansion, it is clear that the computation of the TLNs is based on the separation between the radially decaying multipolar response of the central object and the external growing solution.

In the following subsections, we compute the tidal deformability of nonrotating FSSs in both the polar (electric) and axial (magnetic) sectors. Since the background spacetime is spherically symmetric, these sectors are completely decoupled from each other and can be treated independently. Notice also that, while the electric response is the relativistic generalization of the Newtonian Love number, the magnetic sector is instead fully relativistic [152], since current distributions do not gravitate in Newtonian theory. Furthermore, one can expand the multipolar quantities in spherical harmonics, reducing the problem to radial equations, which are independent of the index m and do not couple perturbations with different values of l. These equations must be solved in both the exterior and interior regions of the object, matching the solutions at a characteristic extraction radius R_{ext}, as discussed below.

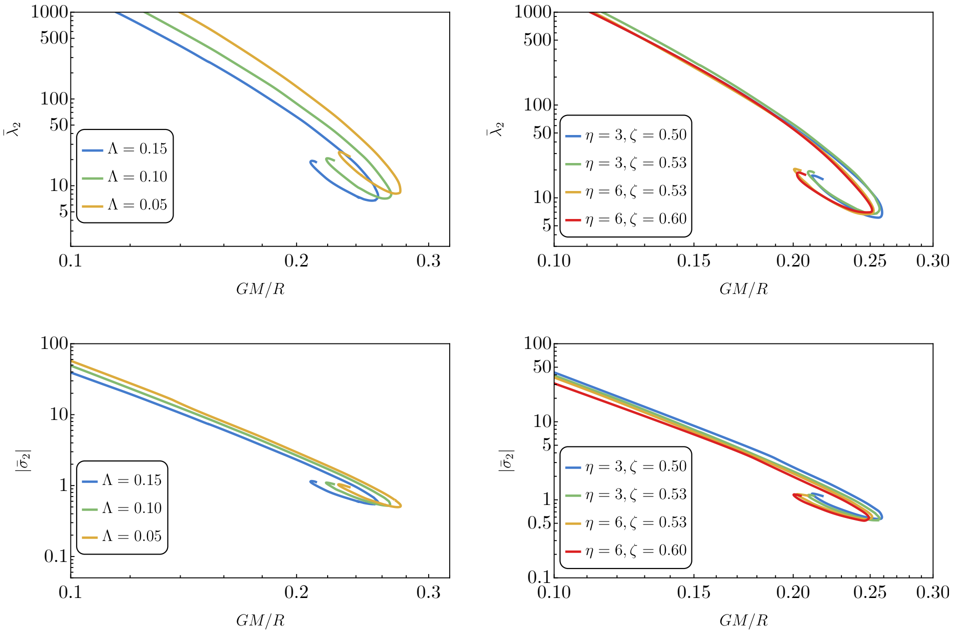

Figure 7.1. Electric (upper panels) and magnetic (lower panels) TLNs for the quadrupolar ($l = 2$) mode as a function of the FSS compactness GM/R. The different curves correspond to different values of the model parameters. In the left panels, we fix $\eta = 3, \zeta = 0.53$ and vary Λ. In the right panels, we fix $\Lambda = 0.15$ and vary η and ζ. We explicitly see that the curves depend only mildly on η and ζ.

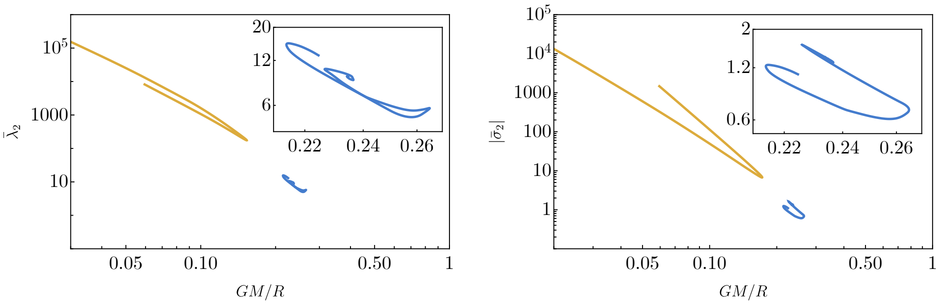

Figure 7.2. Same as Fig. 7.1, but for a negative effective cosmological constant ($\zeta = 0.49$) and for $\Lambda = 0.15, \eta = 3$. In this case there are two disjoint branches of solutions, related to the corresponding branches in the mass-radius diagram shown in Fig. 4.4 (the blue/orange lines corresponding to the upper/lower branches, respectively). The insets are zoomed-in versions of the small islands at large compactness, shown in blue.

7.2.1 Polar sector

In the polar sector, the perturbation equation for the field H_0 is given in eq. (7.19). In the vacuum region outside the object, it reduces to

$$\begin{aligned} H_0'' &+ \frac{2(\rho - GM)}{\rho(\rho - 2GM)} H_0' \\ &- \frac{(4G^2M^2 - 2l(l+1)GM\rho + l(l+1)\rho^2)}{\rho^2(\rho - 2GM)^2} H_0 = 0 \,. \end{aligned} \tag{7.25}$$

The vacuum solution is given in terms of associated Legendre polynomials as

$$H_0(\rho) = c_P \, P_{l2}\left(\frac{\rho}{GM} - 1\right) + c_Q \, Q_{l2}\left(\frac{\rho}{GM} - 1\right) \,, \tag{7.26}$$

where the integration constants c_P and c_Q are found in terms of $H_0(R_{\rm ext})$ and $H_0'(R_{\rm ext})$ by matching to the interior solution. At spatial infinity, $\rho \to \infty$, one gets

$$H_0(\rho) \simeq \tilde{c}_P \, \rho^l + \tilde{c}_Q \, \frac{1}{\rho^{l+1}} + \mathcal{O}\left(\frac{GM}{\rho}\right) \,, \tag{7.27}$$

where the tilde is used to distinguish these coefficients from the ones introduced in eq. (7.26), since an additional dependence on the mass M and numerical factors arises from the asymptotic expansion. One can then plug this expansion into the g_{00} component of the metric to get

$$g_{00} \sim -1 + \frac{2GM}{\rho} + \sum_{l \geq 2, m} \left(\frac{1}{\rho^{l+1}} \, \tilde{c}_{Q,lm} + \rho^l \, \tilde{c}_{P,lm}\right) Y^{lm} \,, \tag{7.28}$$

which can be compared with the asymptotic expansion shown in Eqs. (7.24) once the multipole moments are properly decomposed in terms of symmetric trace-free (STF) tensors Q_{lm} and G_{lm}.

By performing this matching, one can identify the growing solution in $H_0(\rho)$ with the tidal field and the decaying one with the response of the object, respectively, and then extract their multipole moments in terms of the coefficients $c_{Q,lm}$ and $c_{P,lm}$. For the leading multipole moment $l = 2$, the electric TLN reads [151]

$$\begin{aligned} k_2^E = {} & 8(1-2C)^2 C^5 (2C(y-1) - y + 2) \Big\{ 10C(C(2C(C(2C(y+1) + 3y - 2) \\ & - 11y + 13) + 3(5y - 8)) - 3y + 6) \\ & + 15(1-2C)^2 (2C(y-1) - y + 2) \log(1-2C) \Big\}^{-1} \,, \end{aligned} \tag{7.29}$$

where we have defined $C = GM/R_{\rm ext}$ and $y = \rho H_0'/H_0$, both evaluated at the extraction radius $R_{\rm ext}$, which is taken to be much larger than the FSS effective size R (in order for the TLN to be independent of it). In the actual numerical computation, we could not go further than $R_{\rm ext} \sim 2R$ due to the high fine-tuning required by the shooting method used to compute the initial displacement of the scalar field. However, we checked that this yields sufficiently accurate numerical results, due to the exponential decay of the scalar field at $\rho > R$.

The matching variable y can be computed by integrating eq. (7.19) in the interior of the FSS, imposing the boundary condition of regularity at the origin, $\rho = 0$:

$$H_0(\rho) = a_0\, \rho^l \left[1 + \mathcal{O}\left(\rho^2\right)\right] , \qquad \rho \to 0 , \tag{7.30}$$

where the constant a_0 does not affect the TLN, since the problem is linear and this constant enters in both the strength of the tidal field and the size of the induced multipolar deformation, and therefore it cancels out when computing their ratio.

In the upper panels of Fig. 7.1 we show the dimensionless TLN for the leading quadrupolar ($l = 2$) mode as a function of the compactness, as we vary different parameters of the model. Similarly to NSs, the characteristic mass-radius diagram (shown e.g. in fig. 4.2) displays a turning point at large compactness, which shows up also in the TLNs. We observe that in the phenomenologically interesting range around $GM/R \simeq 0.2$ corresponding to the critical solution, the TLN reaches values of the order of $\mathcal{O}(100)$, growing at small compactness due to the dependence $\bar{\lambda}_2 \propto C^{-5}$. The strongest dependence is on the parameter Λ, describing the scalar field vacuum expectation value: in general, lower values of Λ give rise to larger TLNs. The TLNs are almost independent of the degeneracy parameter ζ, which is varied to span both degenerate and nondegenerate vacua, if one considers vacua with positive energy.

When $\zeta < 0.5$, the interior region of the vacuum bubble has negative energy, mimicking an effective anti-de Sitter space (see sec. 4.2). This case, plotted in the left panel of fig. 7.2 for $\zeta = 0.49$, shows a different behavior of the TLN, reflecting what happens at the background level for the mass-radius diagram (see fig. 4.4). Indeed, the presence of two disjoint branches at the background level gives rise to two distinct branches of the TLNs. In particular, the small islands at large compactness (i.e., the blue curves in fig. 7.2 magnified in the insets) represent the TLNs of the upper branch of the mass-radius diagram (continuous blue line in fig. 4.4), whereas the orange curves are associated to the lower branch (dotted line in fig. 4.4). Turning points in the mass-radius diagram give rise to turning points in the TLNs.

7.2.2 Axial sector

In the axial sector, the perturbation equation for the field h_0 is given in eq. (7.21). As discussed in the previous section, in the following we will work under the assumption of an irrotational fluid also in the perturbed configuration. Under this assumption, the perturbation equation at large distances reduces to

$$h_0'' + \frac{(4GM - l(l+1)\rho)}{\rho^2(\rho - 2GM)} h_0 = 0 . \tag{7.31}$$

In the external region, the solution of the perturbation equation reads

$$\begin{aligned} h_0(\rho) = {} & d_P \left(\frac{\rho}{2GM}\right)^{l+1} {}_2F_1\left(-l+1, -l-2, -2l; \frac{2GM}{\rho}\right) \\ & + d_Q \left(\frac{2GM}{\rho}\right)^{l} {}_2F_1\left(l-1, l+2, 2l+2; \frac{2GM}{\rho}\right) , \end{aligned} \tag{7.32}$$

in terms of the hypergeometric function ${}_2F_1\left(a, b, c; x\right)$. The constants d_P and d_Q can be found by the matching procedure in terms of $h_0(R_{\text{ext}})$ and $h_0'(R_{\text{ext}})$. In the large distance regime $\rho \to \infty$ the asymptotic solution is

$$h_0(\rho) = \tilde{d}_P\, \rho^{l+1} + \tilde{d}_Q\, \frac{1}{\rho^l} + \mathcal{O}\left(\frac{GM}{\rho}\right) , \tag{7.33}$$

where, as we discussed in the electric case, the tilded coefficients include additional dependence on the mass and further numerical factors. From this expression, one can obtain the $g_{0\varphi}$ component of the metric as

$$g_{0\varphi} \sim \sum_{l\geq 2,m} \left(\frac{1}{\rho^l}\, \tilde{d}_{Q,lm} + \rho^{l+1}\, \tilde{d}_{P,lm}\right) S_{\varphi}^{lm} . \tag{7.34}$$

By STF decomposing the spatial-temporal part of the metric in Eqs. (7.24), one can again identify the growing and decaying modes of the solutions, and extract the magnetic TLNs. For the leading $l = 2$ mode one gets

$$\begin{aligned} k_2^M &= 96C^5(2C(y-2)-y+3)\Big\{10C(C(2C(Cy+C+y)+3(y-1))-3y+9) \\ &\quad + 15(2C(y-2)-y+3)\log(1-2C)\Big\}^{-1} , \end{aligned} \tag{7.35}$$

where we have defined the quantity $y = \rho h_0'/h_0$, evaluated at the extraction radius R_{ext}. As in the electric case, y can be found by numerically integrating eq. (7.21), with boundary conditions at the center of the FSS given by

$$h_0(\rho) = b_0\, \rho^{l+1}\left[1 + \mathcal{O}\left(\rho^2\right)\right] , \qquad \rho \to 0 , \tag{7.36}$$

where the constant b_0 cancels out in the definition of the TLN.

Similarly to the even sector, the lower panels of Fig. 7.1 and the right panel of Fig. 7.2 show the magnetic TLN for the quadrupolar mode ($l = 2$) for $\zeta \geq 1/2$ and $\zeta < 1/2$, respectively. One can appreciate the same trends observed in the electric case. The magnetic TLN is found to be about an order of magnitude smaller than the electric one, as observed for NSs [152, 188].

7.2.3 Quasi-universal relations

The TLNs of a NS depend on the underlying EOS of nuclear matter. In particular, for a given mass, different prescriptions for the EOS give rise to different radii and tidal deformabilities. However, it was found that the moment of inertia, the spin-induced quadrupole moment, and the electric quadrupolar tidal deformability are related to each other by nearly EOS-independent relations known as the I-Love-Q relations. The latter are approximately universal at the level of $\sim 1\%$, and hold even for strange quark stars [184, 185, 186].

Similar approximately universal relations for NSs also hold between their quadrupolar electric and magnetic tidal deformabilities [187], with an accuracy of about $(1 \div 10)\%$. In particular, the fitting function

$$\begin{aligned} \log|\bar{\sigma}_2| &= a_i + b_i \log\bar{\lambda}_2 + c_i(\log\bar{\lambda}_2)^2 \\ &\quad + d_i(\log\bar{\lambda}_2)^3 + e_i(\log\bar{\lambda}_2)^4 + f_i(\log\bar{\lambda}_2)^5 , \end{aligned} \tag{7.37}$$

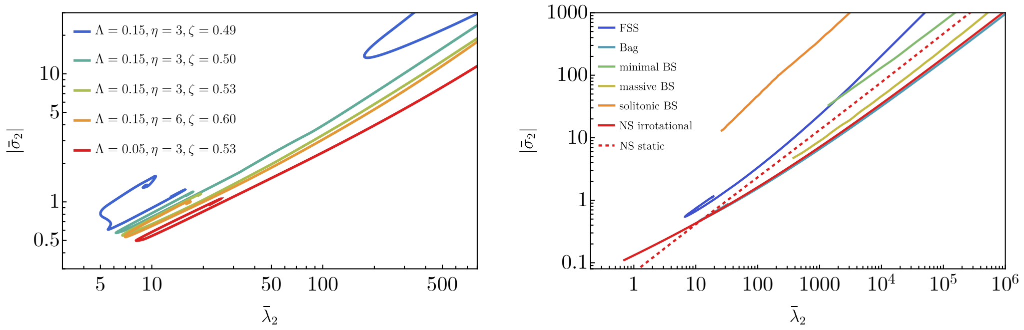

Figure 7.3. Left panel: universality relations for FSSs for different model parameters. In the $\zeta = 0.49$ case, the lower (upper) branch corresponds to the large compactness, blue (small compactness, orange) line of Fig. 7.2. Right panel: comparison of the FSS curve with $\Lambda = 0.15, \eta = 3, \zeta = 0.53$ with the universality curves for other compact objects, such as NSs in the irrotational (solid red line) and static configurations (dashed red line), soliton boson stars (orange line), massive boson stars (yellow line), minimal boson stars (green line) and an effective bag model (Bag, water green line).

with fitting coefficients $a_i = -2.03$, $b_i = 0.487$, $c_i = 9.69 \cdot 10^{-3}$, $d_i = 1.03 \cdot 10^{-3}$, $e_i = -9.37 \cdot 10^{-5}$, $f_i = 2.24 \cdot 10^{-6}$ is a good approximation for realistic NSs described by an irrotational fluid [175]. This fit is shown by the red solid line in the right panel of Fig. 7.3. As expected, as one increases the compactness, NSs approach the BH limit with vanishing tidal deformability.

Figure 7.3 also shows the corresponding approximate universality relations for FSSs. In the left panel, one can appreciate that for FSSs the $\bar{\sigma}_2 - \bar{\lambda}_2$ relations are less universal than for NSs, since the curves display $\mathcal{O}(1)$ corrections in the small compactness regime for different choices of the model parameters, while they are less affected in the large compactness region. The emergence of approximate universal relations can be understood by inspecting Eqs. (7.29) and (7.35). They both depend on two dimensionless parameters, C and y. Recall that both mass and radius scale approximately as $\sim 1/\Lambda^\alpha$, where $\alpha = 1$ for $\zeta \neq 0.5$, and $\alpha = 2$ for $\zeta = 0.5$ (see e.g. fig. 5.5), while the dependence on η, ζ is weak. From the definitions of C and y, we see that they are both left unchanged under such a rescaling. Thus, the TLNs will also be mildly dependent on the fundamental parameters of the theory. This dependence may become weaker and weaker for small values of Λ, which are however numerically challenging to achieve. Indeed, as shown in fig. 5.5, the universal scaling of the mass-radius diagram becomes more and more accurate for small Λ, and one expects to find a similar behavior for the TLNs.

In the right panel of Fig. 7.3, we compare the $\bar{\sigma}_2 - \bar{\lambda}_2$ relations for FSSs with those for realistic NSs. We find that the FSS relation differs from the NS curve, highlighting the different nature of these objects. By comparing the left and right panels of Fig. 7.3 we see that, although the TLNs of a FSS are less universal than those of a NS, the difference in the quasi-universal relations among these classes of objects are much larger than their individual spread. Thus, a sufficiently accurate measurement can tell the two relations apart.

The internal structure of FSSs allows for a comparison with the bag model described by the EOS [22]

$$W = W_0 + P/\omega \,, \tag{7.38}$$

which corresponds to the stiffest possible EOS, as the speed of sound $c_s = \sqrt{\omega}$ takes the maximal value throughout the object. By renormalizing the pressure and density to the central value W_0, one can show that this model allows for a maximal compactness of [22]

$$C_{\text{Bag}} \leq \frac{4}{9}\frac{\omega(4.18+\omega)}{0.77+4.69\omega+\omega^2} \,, \tag{7.39}$$

quantifying the distance from the Buchdahl bound (obtained in the incompressible fluid limit as $\omega \to \infty$). Notice that a nonzero value of the central density W_0 is necessary to ensure a finite radius.

It is therefore interesting to compare the relativistic TLNs of a FSS with those of the bag model assuming large internal pressure and sound speed $\omega = 1/3$, which has a maximum compactness of about $C_{\text{Bag}} \lesssim 0.4$. This comparison is motivated by the fact that, within its interior, the FSS is dominated by relativistic fermions, and the scalar field plays a negligible role. Following this comparison, one can solve the corresponding perturbation equations for the bag model to derive both the electric and magnetic TLNs. Notice that the presence of a discontinuity in the energy density at the object's surface induces a change in the boundary condition for the computation of the electric TLNs, which corresponds to shifting the parameter y by $-4\pi W_0 R^3/M$ [251]. The corresponding universality relations are shown by the water green curve in the right panel of Fig. 7.3. Similarly to the findings of ref. [184], they are not only in agreement with the standard fit for NSs with ordinary EOS, but the final result is also very mildly dependent on the sound speed ω. This suggests that the bag model does not capture the deformability properties of FSSs: the presence of the scalar field makes a sizeable contribution to the overall energy and dominates the object's outer region.

The right panel of Fig. 7.3 also shows the universality relations for different families of boson stars [207]. These complex bosonic self-gravitating configurations experience different tidal deformations compared to the other objects, which strongly depend on the properties of the scalar field potential.

Finally, we notice the presence of a hierarchy between the tidal deformability of each compact object in the configurations with maximal compactness (identified by the lower edges of each curve in Fig. 7.3). In particular, the bag model admits a higher (lower) electric (magnetic) TLN compared to FSSs. Among the various families of boson stars, the minimal model with no scalar interaction displays the largest tidal deformability, while solitonic boson stars are less (more) deformable than massive ones in the electric (magnetic) sector. Accurate tidal deformability measurements can be used to identify different families of compact objects.

As discussed above, we focused on the most interesting case of an irrotational fluid. For a static fluid, the magnetic TLNs of a NS have the opposite sign and are quantitatively different. They display an approximately universal relation different from irrotational fluid NSs [188], as shown by the red dashed line of Fig. 7.3 (obtained from the corresponding fit of ref. [235]). Interestingly, next-generation ground-based GW detectors [230], such as the Einstein Telescope and Cosmic Explorer, should allow us to measure σ_2 and λ_2 with sufficient precision to distinguish the irrotational-fluid case from the static-fluid case [235]. Since the difference between the NS curve and the FSS curve shown in Fig. 7.3 is even larger, future detectors should be able to distinguish FSSs from NSs based on tidal deformability measurements.

Furthermore, from Figs. 7.1 and 7.3 we see that FSSs have lower deformability than other ECOs for certain model parameters, so it could be difficult to tell them apart from black holes through the measurement of tidal effects in gravitational waveforms [112]. It would be interesting to quantify these expectations with more detailed parameter estimation calculations.

7.2.4 Tidal disruption

Let us consider a massive, nonspinning central object whose mass and radius are denoted by M_B and R_B, respectively. It is interesting to ask whether a FSS with radius R and mass M, orbiting around the central object, can be tidally disrupted, assuming $M \ll M_B$. To this end, we need to estimate the distance from the central object at which the FSS will disintegrate because the central body's tidal forces exceed the FSS's self-gravitation. The latter quantity is called the Roche radius of the system, and, up to relativistic corrections, is computed using the following formula

$$R_{\text{Roche}} \sim \gamma R_B \left(\frac{W_B}{W}\right)^{1/3} , \tag{7.40}$$

where W_B, W are the densities of the central object and FSS, respectively, and the numerical coefficient γ takes values ranging from 1.26 for rigid bodies to 2.44 for fluid bodies [252].

Whenever $\zeta > 1/2$ (asymmetric vacua regime), hydrostatic equilibrium imposes (introducing $q = \sqrt{\mu v_{\text{F}}}$)

$$\omega_{\text{F}} \sim \frac{m_f}{\eta} = q \, , \tag{7.41}$$

as long as we are above the minimal configuration in the mass-radius diagram, corresponding to the minimum value for ω_{F} (we do not take into account configurations along the mass-radius diagram under the minimal one because the initial displacement of the scalar field becomes $\mathcal{O}(1)$, and thus true solitonic configurations describing false vacuum pockets are not allowed: see e.g. sec. 5.3.1). Thus, the density W is estimated as the central fermion energy density $W_c \sim k_{\text{F}}^4 \sim \omega_{\text{F}}^4 \sim q^4$.

The physically most compelling scenario is when the tidal disruption happens before the merger phase. Imposing $R_{\text{Roche}} > R_{\text{ISCO}} = 6\, G M_B$ in eq. (7.40), we find the condition (ignoring $\mathcal{O}(1)$ factors)

$$q \lesssim \left(\frac{m_p}{M_B}\right)^{1/2} m_p \approx 1.3\,\text{GeV}\left(\frac{M_\odot}{M_B}\right)^{1/2} . \tag{7.42}$$

For an astrophysical solar-like object with $M_B \sim 1\, M_\odot$, the latter condition implies $q \lesssim 1\,\text{GeV}$. Higgs false vacuum balls and dark soliton stars (see sec. 5.4) require $q \gtrsim 10^2\,\text{GeV}$, and therefore do not get tidally disrupted before the merger. Instead, neutron soliton stars (also known as quark nuggets) correspond to $q \approx 0.2\,\text{GeV}$, potentially allowing for tidal disruption of these nontopological solitons, in a range of masses and radii starting from the (non-compact) minimal configuration

$$M_{\text{min}} \approx 10^{-19}\, M_\odot, \qquad R_{\text{min}} \approx 1\,\text{cm}\, , \tag{7.43}$$

up to the critical one

$$M_c \approx 2\,M_\odot, \qquad R_c \approx 10\,\mathrm{km}\,, \tag{7.44}$$

with a compactness of $GM_c/R_c \sim 0.27$, which is slightly larger than that of an ordinary NS. In the latter case, the mass of the FSS becomes comparable to the mass of the central object, and thus the previous estimates should be taken with a grain of salt, although they should provide the correct order of magnitude.

In a tidal disruption scenario, the quarks released in the disruption event would produce jets of hadrons and photons [84, 253, 254]. Assuming that the amount of energy emitted during a collision is of the order of $f_{\rm rad}(GM_BM/R_{\rm Roche})$ and considering an efficiency factor $f_{\rm rad}$ for the energy going into visible Standard Model radiation, the corresponding power output in one orbital period is given by

$$\mathcal{P} \simeq 10^{21} L_\odot f_{\rm rad}\left(\frac{M}{0.1 M_\odot}\right)\left(\frac{M_B}{M_\odot}\right)^{2/3}\left(\frac{q}{0.2\,\mathrm{GeV}}\right)^{10/3}\,, \tag{7.45}$$

where $L_\odot = 3.8\cdot 10^{26}\,\mathrm{W}$ is the luminosity of the Sun. This power is comparable to the one emitted by superradiance (see ref. [255] for a discussion).

To assess whether a telescope on Earth could detect this radiation, we assume an angular resolution of $\delta\Omega = 1^\circ \times 1^\circ = (\pi/180)^2\,\mathrm{sr}$ and that the binary is situated at a distance $d \simeq 1\,\mathrm{Gpc}$. Then, the frequency-weighted spectral density is estimated to be

$$\begin{aligned}\nu I_\nu = \frac{\mathcal{P}}{d^2\delta\Omega} &\simeq 10^{-9}\,\frac{\mathrm{W}}{\mathrm{m^2 sr}}\left(\frac{f_{\rm rad}}{10^{-10}}\right)\left(\frac{d}{\mathrm{Gpc}}\right)^{-2} \\ &\times\left(\frac{M_B}{M_\odot}\right)^{2/3}\left(\frac{M}{0.1M_\odot}\right)\left(\frac{q}{0.2\,\mathrm{GeV}}\right)^{10/3}\,.\end{aligned} \tag{7.46}$$

For comparison, the observed cosmic backgrounds of X-rays and gamma rays range from $10^{-10}\mathrm{W/m^2sr}$ at energies around 10 keV to $10^{-13}\mathrm{W/m^2sr}$ around 10 GeV [256], implying that the tidal disruption of these quark nuggets may produce detectable photons for an efficiency factor as small as 10^{-10}. If the central object is a BH, a sizeable fraction of the emitted matter could be accreted by the central object, giving rise to a subsequent afterglow.

7.3 Conclusions

In this chapter, we studied the deformability properties of FSSs, solutions of general relativity in which a real scalar field is coupled to a fermionic field by a Yukawa coupling [4]. The coupling generates an effective mass for the fermions as the scalar field transitions from a false vacuum to a true vacuum configuration. The structure of vacua in the scalar field potential determines the nature of the corresponding compact objects, whose mass-radius curves exhibit different phenomenology for different model parameters. We have studied both electric- and magnetic-type perturbations of a FSS background. By perturbing both the scalar and fermionic sectors (and assuming the latter to be described by the Thomas-Fermi approximation also in the perturbed configuration), we have derived the corresponding perturbation equations and solved them to obtain the conservative and irrotational TLNs. These are found to depend on the model parameters, especially on the scalar field vacuum expectation value. As in the case of NSs, the magnetic TLNs are generally smaller than the electric TLNs.

Using the tidal deformabilities computed in this way, we have investigated the existence of approximately universal relations between the Love numbers in both parity sectors, showing a mild dependence on the model parameters and therefore a solid prediction for these relations (even though they are less universal than the ones for NSs). We then compared the quasi-universal relations for FSSs with those found for other compact objects, such as NSs and boson stars, showing that the universality relations corresponding to different classes of compact objects are significantly different. This feature could be used as a novel probe to tell apart various classes of compact objects using tidal deformability measurements with next-generation detectors.

The characteristic values of the TLNs of FSSs (for model parameters corresponding to objects in the solar mass range) imply that these quantities may be measurable by future gravitational wave interferometers, such as the Einstein Telescope and Cosmic Explorer. In particular, the results of ref. [235] imply that these instruments could measure both the electric and magnetic Love numbers with an accuracy of a few percent, potentially allowing us to distinguish FSSs from other compact objects in the solar mass range, such as ordinary NSs or black holes [112].

Finally, we discussed the possible disruption of a FSS in a binary system with another compact object, such as a black hole, and derived a bound on the vacuum expectation values that may allow for a tidal disruption event before the ISCO frequency is reached. Such tidal disruption events could happen for nontopological quark nuggets, which could release jets of hadrons and photons during the event. If this process occurs in nature, it would provide a significant contribution to the observed cosmic backgrounds of X-rays and gamma rays, and even to single resolvable events.

Chapter 8

General conclusions and future prospects

In this thesis, we investigated a simple model for ECOs dubbed *fermion soliton stars* [13, 1, 2]. Depending on the parameters of the underlying theory, the model can accommodate ECOs in a vast range of masses, including compact subsolar and supermassive fermion soliton stars. In particular, for natural model parameters between the QCD and the electroweak scale, this model predicts the existence of compact objects in the subsolar/solar range [3], which could be relevant for current and future LIGO-Virgo-KAGRA observations (see e.g. Refs. [112, 113]). In Chapters 3 and 4, we explored in detail the properties of the model, highlighting the crucial role of the scalar vacuum structure in dictating the features of the solutions. In Chapter 5, we explored particle-physics implications of the previous findings, highlighting the mechanism of non-perturbative vacuum scalarization as a support mechanism for new compact objects that can form in the early Universe, can collapse into primordial black holes through accretion past their maximum mass, and serve as dark matter candidates. In chapter 7, we computed the TLNs of fermion soliton stars. We discussed the existence of approximate universal relations for the electric and magnetic tidal deformability of these stars, and compared them with other solutions of general relativity, such as neutron stars or boson stars, showing that a measurement of the electric and magnetic tidal Love numbers (as potentially achievable by next-generation gravitational wave detectors) can be used to disentangle these families of compact objects.

Although we focused on static and spherically symmetric background solutions, there is no fundamental obstacle in considering spinning configurations and the dynamical regime, both of which would be relevant to studying the phenomenology of fermion soliton stars, along the lines of what has been widely studied for boson stars [54] and for mixed fermion-boson stars [257]. Moreover, due to the existence of multiple branches [64] and the absence of a Newtonian limit in certain cases, an interesting study concerns the radial linear stability of these solutions. We hope to address these points in future work.

A further important extension concerns the dynamical formation of these solutions. Many different channels have already been proposed in the literature. For example, NTSs arising from eq. (5.1) can be produced by a first-order cosmological phase transition [57]. Alternatively, the Yukawa interaction, if enough long-range, drives clustering and leads to the formation of compact NTSs [109, 110, 111]. Further possible formation channels, worth exploring in future work, are the following. First of all, statistical fluctuations inevitably present even during a crossover, are in principle able to provide a large concentration of fermions [258] and can be, therefore, the dominant source of charge fluctuations which leads to NTS formation through solitosynthesis. Moreover, one could consider a configuration where there is a gas of N free (massive) fermions moving in the true scalar vacuum $h \equiv v$. If $\eta \gtrsim 1$ and for a sufficiently large perturbation of the scalar field with energy above a certain threshold, we expect to end up in the true (scalarized) ground state.

The idea that a system can scalarize non-linearly, i.e. only if perturbed above a certain threshold, has been already numerically studied for scalar perturbations around a Schwarzschild black hole in scalar-Gauss-Bonnet gravity theories [259]. An interesting extension of our work would be performing similar simulations in our model, possibly within a cosmological scenario.

Finally, we made an initial step towards a full investigation of the tidal interactions and tidal deformability of fermion soliton stars, and our results can be improved in various directions. It would be interesting to perform a more detailed study to understand how tidal effects could be used to distinguish different classes of ECOs. Moreover, it would be important to assess if the I-Love-Q relations are valid also for rotating FSSs. Finally, given the intrinsic time dependence in the evolution of a binary system, it would be interesting to investigate the FSS dissipative coefficients and frequency-dependent TLNs, as recently discussed in Refs. [223, 226] for Kerr-like compact objects. We leave these studies for future work.

Appendix A

Connection with scalar-tensor theories

In this Appendix, we discuss whether the model for fermion soliton stars presented in the main text can also arise in the context of a scalar-tensor theory of gravity (see, e.g., [260] for a review on modified theories of gravity).

In the so-called Jordan frame,[1] where gravity is minimally coupled to matter fields, scalar-tensor theories are described by the action (see, for example, [261])

$$\begin{aligned}\hat{S} = \int d^4x \, \frac{\sqrt{-\hat{g}}}{16\pi G}\Big[F(\hat{\phi})\hat{R} - Z(\hat{\phi})\hat{g}^{\mu\nu}\partial_\mu\hat{\phi}\partial_\nu\hat{\phi} - \hat{U}(\hat{\phi})\Big] \\ + \hat{S}_m(\hat{\psi}_m; \hat{g}_{\mu\nu})\,. \qquad \text{(A.1)}\end{aligned}$$

The coupling functions F and Z single out a particular theory within the class. For example, Brans-Dicke theory corresponds to $F = \hat{\phi}$ and $Z = \omega_0/\hat{\phi}$, where ω_0 is a constant.

We can write the theory in an equivalent form in the so-called Einstein frame, where gravity is minimally coupled to the scalar field. For this purpose, we perform a conformal transformation of the metric, $\hat{g}_{\mu\nu} = A^2(\phi)g_{\mu\nu}$ with $A(\phi) = F^{-1/2}(\hat{\phi})$, a field redefinition, $\phi = \phi(\hat{\phi})$, and a conformal rescaling of the matter field, $\hat{\psi}_m \to \psi_m$. The scalar field ϕ is now minimally coupled to $g_{\mu\nu}$, whereas ψ_m is minimally coupled to $\hat{g}_{\mu\nu}$ [261]. The energy-momentum tensor is $T_{\mu\nu} = A^2(\phi)\hat{T}_{\mu\nu}$, whereas the scalar potential becomes $U(\phi) = \frac{\hat{U}(\hat{\phi})}{16\pi G F^2(\hat{\phi})}$

The scalar field equation in the Einstein frame reads

$$\Box\phi = -T\frac{d\log A(\phi)}{d\phi} + \frac{\partial U}{\partial\phi}\,. \qquad \text{(A.2)}$$

Since in our theory (3.1) the scalar field is minimally coupled to gravity, it is natural to interpret it in the context of the Einstein frame. Thus, we can compare eq. (A.2) to the second equation in (3.11):

$$\Box\phi = -fS + \frac{\partial U}{\partial\phi}\,, \qquad \text{(A.3)}$$

---

[1] In this appendix we used a hat to denote quantities in the Jordan frame, whereas quantities without the hat refer to the Einstein frame where gravity is minimally coupled to the scalar field.

which, using eq. (3.8), can be written as

$$\Box\phi = \frac{f}{(m_f - f\phi)} T + \frac{\partial U}{\partial \phi} \,. \tag{A.4}$$

Therefore, if we identify

$$\frac{d \log A(\phi)}{d\phi} = \frac{-f}{(m_f - f\phi)} = \frac{1}{\phi - \phi_0} \,, \tag{A.5}$$

the scalar equation of our model is the same as in a scalar-tensor theory with coupling $A(\phi)$ in the Einstein frame. Integrating this equation yields (henceforth assuming $A(0) = 1$),

$$A(\phi) = 1 - \frac{\phi}{\phi_0} = \frac{m_{\rm eff}}{m_f} \,. \tag{A.6}$$

Interestingly, the matter coupling vanishes when $\phi \approx \phi_0$.

It is left to be checked if the gravitational sector of our model is equivalent to that of a scalar-tensor theory with $A(\phi)$ given by eq. (A.6). Let us consider a degenerate gas of noninteracting fermions with mass m_f in the Jordan frame, with energy-momentum

$$\hat{T}^{\mu\nu} = (\hat{W} + \hat{P})\hat{u}^\mu \hat{v}^\nu + \hat{g}^{\mu\nu}\hat{P} \tag{A.7}$$

where, assuming spherical symmetry,

$$\begin{aligned} \hat{W}(\hat{\rho}) &= \frac{2}{(2\pi)^3} \int_0^{\hat{k}_F(\hat{\rho})} d^3k \, \sqrt{k^2 + m_f^2} \\ \hat{P}(\hat{\rho}) &= \frac{2}{(2\pi)^3} \int_0^{\hat{k}_F(\hat{\rho})} d^3k \, \frac{k^2}{3\sqrt{k^2 + m_f^2}} \,. \end{aligned} \tag{A.8}$$

In spherical symmetry, since the spacetime has the same form as in eq. (3.13), it is straightforward to minimize the energy of the fermion gas at a fixed number of fermions (the calculation is exactly the same as the one done to obtain eq. (3.19)):

$$\hat{k}_F^2 = \hat{\omega}_F^2 e^{-2\hat{u}} - m_f^2 \,. \tag{A.9}$$

It is important to notice that in the standard scalar-tensor theory in the Jordan frame, there is no Yukawa interaction; therefore, the fermion particles do not acquire any effective mass.

In the Einstein frame, eq. (A.7) simply reads

$$T^{\mu\nu} = (W + P)u^\mu u^\nu + g^{\mu\nu}P \,, \tag{A.10}$$

where $W = A^4(\phi)\hat{W}$ and $P = A^4(\phi)\hat{P}$. Therefore, also in the Einstein frame we have a perfect fluid in the form of a zero-temperature Fermi gas. Let us now compute the expressions of W and P explicitly. First of all, from eq. (A.8), following the same computation presented in the main text, we get

$$\begin{aligned} \hat{W} &= \frac{m_f^4}{8\pi^2} \left[\hat{x}\sqrt{1 + \hat{x}^2}(1 + 2\hat{x}^2) - \log\Big(\hat{x} + \sqrt{\hat{x}^2 + 1}\Big) \right] \\ \hat{P} &= \frac{m_f^4}{8\pi^2} \left[\hat{x}\Big(\frac{2}{3}\hat{x}^2 - 1\Big)\sqrt{1 + \hat{x}^2} + \log\Big(\hat{x} + \sqrt{\hat{x}^2 + 1}\Big) \right] \end{aligned} \tag{A.11}$$

where $\hat{x} = \hat{k}_F/m_f$. Since $A(\phi) = m_{\text{eff}}/m_f$, we obtain

$$\begin{aligned} W &= \frac{m_{\text{eff}}^4}{8\pi^2}\left[\hat{x}\sqrt{1+\hat{x}^2}(1+2\hat{x}^2) - \log\Big(\hat{x} + \sqrt{\hat{x}^2+1}\Big)\right] \\ P &= \frac{m_{\text{eff}}^4}{8\pi^2}\left[\hat{x}\Big(\frac{2}{3}\hat{x}^2 - 1\Big)\sqrt{1+\hat{x}^2} + \log\Big(\hat{x} + \sqrt{\hat{x}^2+1}\Big)\right]. \end{aligned} \tag{A.12}$$

Note that $W(\hat{x})$ and $P(\hat{x})$ above implicitly define an equation of state that is exactly equivalent to that obtained from W and P in Eqs. (3.22a) and (3.22b). This shows that our model can be interpreted as a scalar-tensor theory in the Einstein frame with coupling to matter given by[2] $A(\phi) = m_{\text{eff}}/m_f$.

Furthermore, note that the dimensionless quantity $\hat{x} = \hat{k}_F/m_f = k_F/m_{\text{eff}} = x$ is invariant under a change from the Jordan to the Einstein frame. Therefore, W and P are exactly those given in Eqs. (3.22a) and (3.22b).

Finally, $\hat{S}$ in the Jordan frame reads

$$\hat{S} = \frac{2}{(2\pi)^3}\int_0^{\hat{k}_F} d^3k\,\frac{m_f}{\sqrt{k^2+m_f^2}} \tag{A.13}$$

$$= \frac{m_f^3}{2\pi^2}\left[\hat{x}\sqrt{1+\hat{x}^2} - \log\Big(\hat{x} + \sqrt{\hat{x}^2+1}\Big)\right], \tag{A.14}$$

while in the Einstein frame[3]

$$S = A^3\hat{S} = \frac{m_{\text{eff}}^3}{2\pi^2}\left[x\sqrt{1+x^2} - \log\Big(x + \sqrt{x^2+1}\Big)\right], \tag{A.15}$$

since $\hat{x} = x$. Thus, also in this case we obtain the same expression as in eq. (3.22c).

Having assessed that our model can be interpreted in the context of a scalar-tensor theory, it is interesting to study the latter in the Jordan frame. In particular, since

$$A(\phi) = \frac{1}{\sqrt{F(\hat{\phi})}}, \tag{A.16}$$

and $A(\phi) = 1 - \phi/\phi_0$, the coupling function $F(\hat{\phi})$ is *singular* in $\hat{\phi}(\phi_0)$. In the language of the scalar-tensor theory, we see that in the core of a fermion soliton star, where $\phi \approx \phi_0$ and matter is almost decoupled in the Einstein frame, the scalar field in the Jordan frame is strongly coupled to gravity.

---

[2] Note that our model and the scalar-tensor theory are not exactly equivalent to each other. Indeed, while in the scalar-tensor theory *any* matter field is universally coupled to $A(\phi)\hat{g}_{\mu\nu}$, in our model this is the case only for the fermion gas, while any other matter field is minimally coupled to the metric, in agreement with the fact that our model is based on standard Einstein's gravity.

[3] The fact that $S = A^3\hat{S}$ can be derived from the condition $A^4(\phi)\hat{T} = T \Rightarrow A^4(\phi)m_f\hat{S} = m_{\text{eff}}S$.

Appendix B

Embedding with the Standard Model

A simple way to derive eq. (5.1) is starting from the standard electroweak theory minimally coupled to Einstein gravity,

$$S = \int \mathrm{d}^4x\,\sqrt{-g}\Big[\frac{R}{16\pi G} - \mathcal{L}_{\text{fields}}\Big], \tag{B.1}$$

where

$$\begin{aligned}\mathcal{L}_{\text{fields}} = &-(\partial_\mu H)^\dagger(\partial^\mu H) - L^\dagger \not{D} L - R^\dagger \not{D} R\\ &-\frac{\lambda}{4}\Big(H^\dagger H - \frac{v^2}{2}\Big)^2 - f(L^\dagger H R + R^\dagger H^\dagger L),\end{aligned} \tag{B.2}$$

and H is the Higgs field, doublet under $SU(2)$, whereas

$$L = \begin{pmatrix} v_L \\ \psi_L \end{pmatrix}, \quad R = \psi_R, \tag{B.3}$$

are a $SU(2)$ doublet of left-handed fermions and a $SU(2)$ singlet of right-handed fermion, respectively.

By exploiting the $SU(2) \times U(1)$ gauge symmetry to remove the spurious degrees of freedom, we write

$$H = \begin{pmatrix} 0 \\ \frac{h}{\sqrt{2}} \end{pmatrix}. \tag{B.4}$$

Substituting in eq. (B.1), we recover eq. (5.1) where

$$\psi = \begin{pmatrix} \psi_L \\ \psi_R \end{pmatrix}. \tag{B.5}$$

Appendix C

Fermionic perturbations

In the axial sector, since $\phi_1 \equiv 0$, the $\theta\theta$ plus the $\varphi\varphi$ component of the Einstein equations gives simply $\delta k_{\mathrm{F}} = 0$. Thus, $\delta P = \delta W = \delta S = 0$. Conversely, in the polar sector, the same combination of the Einstein equations gives

$$P_1 = \frac{1}{2}H_0(\bar{P} + \bar{W}) + U_1 + \Big(f\bar{S} - \frac{\partial U}{\partial \phi}\Big|_{\bar{\phi}}\Big)\phi_1 \,. \tag{C.1}$$

Following the procedure described in Sec. 7.1.1, we express $k_{\mathrm{F}} = (k_{\mathrm{F}})_1(\rho)Y(\theta,\varphi)$ (omitting the multipolar indices) as

$$\begin{aligned}(k_{\mathrm{F}})_1 = \frac{1}{4\bar{k}_{\mathrm{F}}^4}\Bigg[&- \phi_1\Bigg(3\sqrt{\bar{k}_{\mathrm{F}}^2 + m_{\mathrm{eff}}^2}\Bigg(4\pi^2 \partial U/\partial\phi\big|_{\bar{\phi}} + f m_{\mathrm{eff}}^3\Bigg(\log\Bigg(1 - \frac{\bar{k}_{\mathrm{F}}}{\sqrt{\bar{k}_{\mathrm{F}}^2 + m_{\mathrm{eff}}^2}}\Bigg) \\ &- \log\Bigg(\frac{\bar{k}_{\mathrm{F}}}{\sqrt{\bar{k}_{\mathrm{F}}^2 + m_{\mathrm{eff}}^2}} + 1\Bigg)\Bigg) - 4\pi^2 f\bar{S}\Bigg) + 2f\bar{k}_{\mathrm{F}}^3 m_{\mathrm{eff}} + 6f\bar{k}_{\mathrm{F}} m_{\mathrm{eff}}^3\Bigg) \\ &+ 6\pi^2 H_0\sqrt{\bar{k}_{\mathrm{F}}^2 + m_{\mathrm{eff}}^2}(\bar{P} + \bar{W}) + 12\pi^2 U_1\sqrt{\bar{k}_{\mathrm{F}}^2 + m_{\mathrm{eff}}^2}\Bigg]\,,\end{aligned} \tag{C.2}$$

where $m_{\mathrm{eff}} = m_f - f\bar{\phi}$.

Expanding Eqs. (3.5), (3.7), and substituting eq. (C.1) and eq. (C.2), we obtain W_1, S_1 in terms of the background quantities m_{eff} and $\bar{k}_{\mathrm{F}}$, as well as metric and scalar perturbations, as follows:

$$
\begin{aligned}
W_1 = \frac{1}{4\pi^2\bar{k}_{\mathrm{F}}^2\sqrt{\bar{k}_{\mathrm{F}}^2+m_{\mathrm{eff}}^2}} \Bigg[& 3m_{\mathrm{eff}}^2\sqrt{\bar{k}_{\mathrm{F}}^2+m_{\mathrm{eff}}^2}(\phi_1(-4\pi^2\partial U/\partial\phi|_{\bar{\phi}} + f m_{\mathrm{eff}}^3(\log\left(\frac{\bar{k}_{\mathrm{F}}}{\sqrt{\bar{k}_{\mathrm{F}}^2+m_{\mathrm{eff}}^2}}+1\right) \\
& - \log\left(1-\frac{\bar{k}_{\mathrm{F}}}{\sqrt{\bar{k}_{\mathrm{F}}^2+m_{\mathrm{eff}}^2}}\right)) + 4\pi^2 f\bar{S}) + 4\pi^2 U_1) + \bar{k}_{\mathrm{F}}^2\sqrt{\bar{k}_{\mathrm{F}}^2+m_{\mathrm{eff}}^2}(\phi_1(-12\pi^2\partial U/\partial\phi|_{\bar{\phi}} \\
& + f m_{\mathrm{eff}}^3(-3\log\left(1-\frac{\bar{k}_{\mathrm{F}}}{\sqrt{\bar{k}_{\mathrm{F}}^2+m_{\mathrm{eff}}^2}}\right) + 3\log\left(\frac{\bar{k}_{\mathrm{F}}}{\sqrt{\bar{k}_{\mathrm{F}}^2+m_{\mathrm{eff}}^2}}+1\right) \\
& + 2\tanh^{-1}\left(\frac{\bar{k}_{\mathrm{F}}}{\sqrt{\bar{k}_{\mathrm{F}}^2+m_{\mathrm{eff}}^2}}\right)) + 12\pi^2 f\bar{S}) + 12\pi^2 U_1) - 4f\bar{k}_{\mathrm{F}}^5 m_{\mathrm{eff}}\phi_1 - 10f\bar{k}_{\mathrm{F}}^3 m_{\mathrm{eff}}^3\phi_1 \\
& - 6f\bar{k}_{\mathrm{F}} m_{\mathrm{eff}}^5\phi_1 + 6\pi^2 H_0(\bar{k}_{\mathrm{F}}^2+m_{\mathrm{eff}}^2)^{3/2}(\bar{P}+\bar{W})\Bigg], \qquad \text{(C.3)}
\end{aligned}
$$

$$
\begin{aligned}
S_1 = \frac{1}{4\pi^2\bar{k}_{\mathrm{F}}^2\sqrt{\bar{k}_{\mathrm{F}}^2+m_{\mathrm{eff}}^2}} \Bigg[& 12\pi^2 m_{\mathrm{eff}}\sqrt{\bar{k}_{\mathrm{F}}^2+m_{\mathrm{eff}}^2}(\phi_1(f\bar{S}-\partial U/\partial\phi|_{\bar{\phi}}) + U_1) - 3f m_{\mathrm{eff}}^4\phi_1 \\
& \left(\sqrt{\bar{k}_{\mathrm{F}}^2+m_{\mathrm{eff}}^2}\left(\log\left(1-\frac{\bar{k}_{\mathrm{F}}}{\sqrt{\bar{k}_{\mathrm{F}}^2+m_{\mathrm{eff}}^2}}\right) - \log\left(\frac{\bar{k}_{\mathrm{F}}}{\sqrt{\bar{k}_{\mathrm{F}}^2+m_{\mathrm{eff}}^2}}+1\right)\right) + 2\bar{k}_{\mathrm{F}}\right) \\
& - 2f\bar{k}_{\mathrm{F}}^2 m_{\mathrm{eff}}^2\phi_1\left(4\bar{k}_{\mathrm{F}} - 3\sqrt{\bar{k}_{\mathrm{F}}^2+m_{\mathrm{eff}}^2}\tanh^{-1}\left(\frac{\bar{k}_{\mathrm{F}}}{\sqrt{\bar{k}_{\mathrm{F}}^2+m_{\mathrm{eff}}^2}}\right)\right) - 2f\bar{k}_{\mathrm{F}}^5\phi_1 \\
& + 6\pi^2 H_0 m_{\mathrm{eff}}\sqrt{\bar{k}_{\mathrm{F}}^2+m_{\mathrm{eff}}^2}(\bar{P}+\bar{W})\Bigg]. \qquad \text{(C.4)}
\end{aligned}
$$

Acknowledgments

Denken ist Danken, usava dire Heidegger, *pensare è ringraziare*.

Penso ai miei maestri Paolo Pani ed Alfredo Urbano, a tutte le nostre discussioni di fisica. Li ringrazio per tutto ciò che mi hanno trasmesso, a partire dal loro modo di pensare la fisica e di fare ricerca. Mi ritengo molto fortunato ad averli incontrati e le conseguenze ultime di questo incontro sono una storia ancora da scrivere.

Penso a Gabriele Franciolini, perché è stato un riferimento durante i primi due anni del mio dottorato e gli sono grato per tutto quello che mi ha insegnato (cominciando da *Mathematica*).

Penso a tutti i miei collaboratori, ciascuno dei quali mi ha lasciato qualcosa e anche di più. In particolare ringrazio Valerio De Luca per il suo modo allegro e dirompente di fare fisica (e anche per le correzioni a questa tesi).

Penso a Marco Melis, Enrico Cannizzaro, Fabrizio Corelli, Robin Croft, Massimo Vaglio, Francesco Crescimbeni, Antonio Iovino e a tutto il gruppo di gravità di Roma, ai tanti (lunch) group meeting condivisi insieme, alle cene e alle pause caffè. Penso ai tanti visitatori, in particolare Davide Perrone.

Penso a Beth Long, Stefano Villani, Alessandro Veutro, Paolo Fachin, e a tutti i membri dei PhD seminar. Penso a tutte le avventure condivise insieme. Senza di loro il mio dottorato avrebbe perso metà del suo valore. Mi hanno insegnato che il modo migliore per prendersi cura di una comunità è diventarne parte attiva.

Penso a tutta la scuola di dottorato di Roma, Lucas, Rodrigo, Jacopo e a tutti gli altri, penso alle attività svolte insieme, alle combattutissime partite Fermi contro Marconi nel campetto di San Lorenzo.

Penso ai miei compagni di stanza, la 339b, Claudio, Enrico, Ilya, Saverio, Pier e tutti gli altri. Penso ad Enrico che puntualmente alle 13 abbassava la tapparella.

Penso ai periodi trascorsi a Baltimora, ai tanti pranzi con David Kaplan, Surjeet Rejendran e Francesco Serra, durante i quali non c'è stato un principio della fisica che non sia stato messo in discussione. Francesco è diventato anche il mio nuovo compagno di ufficio e ne sono contento: penso che il nostro vascello possa navigare lontano. Penso ad Emanuele Berti, Kostas, Luca e a tutto il gruppo di gravità, penso alle partite a Tedesca di fronte al dipartimento, e alle cene in giro. Penso ai visitatori che ho conosciuto in quei periodi, in particolare Matteo Della Rocca.

Penso agli amici che mi hanno accompagnato nei miei studi in fisica, Nicolò, Michela, Nick J, Elena, Matteo, Maria, ed in particolare Piergiuseppe. Lo ringrazio per le innumerevoli discussioni, per tutte le lezioni seguite insieme, per aver tanto contribuito ad accendere in me la passione per le interazioni fondamentali.

Penso a Marco, Alessio ed anche a Giovanni, a tutto il tempo speso insieme fin dalle scuole medie, le ora trascorse giocando a FIFA. Penso ai nostri aperitivi a San

Marco, ai vagabondaggi per le vie di Napoli.

Penso ai miei genitori, Letizia e Marco, senza i quali, non so se sia ovvio o misterioso scriverlo, non sarei qui. Ringrazio mia madre per la cura che sempre ha messo nel seguire la mia formazione. Penso alla mia sorellina Alisia, senza la quale nulla sarebbe lo stesso. Penso ai miei cuginetti, Giammy, Matty, Giulio, Pier ad Ale, per le sterminate ore di gioco spese insieme. Penso a zia Emanuela, a zio Tommy, ad Erika, a nonno Silvano e Luisa, a nonna Anna, a tutta la mia famiglia.

Penso agli insegnanti che ho incontrato e che, prestando fede alla parola, hanno lasciato un segno. In particolare la prof.ssa Rosalia e la prof.ssa Donatella, il prof. Pellino, la prof.ssa Gentile, il prof. Massimo Testa, il prof. Lucarelli, dal quale ho udito l'epigrafe che apre questa tesi e tutto quello che so di filosofia. Se fosse possibile, tornerei domani stesso a scuola per seguire le sue lezioni, poiché non ho dimenticato, come voleva Socrate, che i più grandi problemi sono quelli contenuti in ciascuno di noi, mentre tutto il resto è solo un gioco di onesti pirati.

Cos'altro manca? Come non pensare alla notte nell'alto mare aperto, sovrastato da miriadi di stelle splendenti? O all'azzurro del cielo in una tersa giornata di Sole, quando nell'autunno tutti gli alberi sono tinti di rosso? Non è forse dalla bellezza cesellata nell'essere che muove la curiosità scientifica e l'amore per la fisica?

Da ultimo, penso a Beatrice.

Vorrei tornare a quel giorno dove tu
ti arrampicavi su un albero,
fra le rocce del Tuscolo,
un fiore avvolgeva i tuoi capelli;
non ricordo se vidi una ninfa,
nella sua grande bellezza,
o forse vidi Momo,
nella sua semplicità,
che una volta abitava
nel vicino anfiteatro;
non ricordo nemmeno
le parole che dissi,
ma avrei dovuto dire
le parole del Poeta,
A light that glows unthanked
A light that cannot see itself and does not profit from its shine
A light that glows truly, showing right from wrong.

Bibliography

[1] L. Del Grosso, G. Franciolini, P. Pani, and A. Urbano, “Fermion soliton stars,” *Phys. Rev. D*, vol. 108, no. 4, p. 044024, 2023.

[2] L. Del Grosso and P. Pani, “Fermion soliton stars with asymmetric vacua,” *Phys. Rev. D*, vol. 108, no. 6, p. 064042, 2023.

[3] L. Del Grosso, P. Pani, and A. Urbano, “Compact objects in and beyond the Standard Model from non-perturbative vacuum scalarization,” 1 2024.

[4] E. Berti, V. De Luca, L. Del Grosso, and P. Pani, “Tidal Love numbers and approximate universal relations for fermion soliton stars,” *Phys. Rev. D*, vol. 109, no. 12, p. 124008, 2024.

[5] M. Cirelli, A. Strumia, and J. Zupan, “Dark Matter,” 6 2024.

[6] J. S. Schwinger, “On gauge invariance and vacuum polarization,” *Phys. Rev.*, vol. 82, pp. 664–679, 1951.

[7] B. P. Abbott *et al.*, “Observation of Gravitational Waves from a Binary Black Hole Merger,” *Phys. Rev. Lett.*, vol. 116, no. 6, p. 061102, 2016.

[8] R. Friedberg, T. D. Lee, and Y. Pang, “Scalar Soliton Stars and Black Holes,” *Phys. Rev. D*, vol. 35, p. 3658, 1987.

[9] C. Palenzuela, P. Pani, M. Bezares, V. Cardoso, L. Lehner, and S. Liebling, “Gravitational Wave Signatures of Highly Compact Boson Star Binaries,” *Phys. Rev. D*, vol. 96, no. 10, p. 104058, 2017.

[10] M. Bezares, M. Bošković, S. Liebling, C. Palenzuela, P. Pani, and E. Barausse, “Gravitational waves and kicks from the merger of unequal mass, highly compact boson stars,” *Phys. Rev. D*, vol. 105, no. 6, p. 064067, 2022.

[11] M. Bošković and E. Barausse, “Soliton boson stars, Q-balls and the causal Buchdahl bound,” *JCAP*, vol. 02, no. 02, p. 032, 2022.

[12] K. Petraki and R. R. Volkas, “Review of asymmetric dark matter,” *Int. J. Mod. Phys. A*, vol. 28, p. 1330028, 2013.

[13] T. D. Lee and Y. Pang, “Fermion Soliton Stars and Black Holes,” *Phys. Rev. D*, vol. 35, p. 3678, 1987.

[14] D. Baumann, *Cosmology.* Cambridge University Press, 7 2022.

[15] M. Shibata, “3-D numerical simulation of black hole formation using collisionless particles: Triplane symmetric case,” *Prog. Theor. Phys.*, vol. 101, pp. 251–282, 1999.

[16] E. de Jong, J. C. Aurrekoetxea, and E. A. Lim, “Primordial black hole formation with full numerical relativity,” *JCAP*, vol. 03, no. 03, p. 029, 2022.

[17] G. D. Birkhoff and R. E. Langer, *Relativity and modern physics.* 1923.

[18] B. F. Schutz, *A FIRST COURSE IN GENERAL RELATIVITY.* Cambridge, UK: Cambridge Univ. Pr., 1985.

[19] V. Ferrari, L. Gualtieri, and P. Pani, *General Relativity and its Applications.* CRC Press, 12 2020.

[20] N. K. Glendenning, *Compact stars: Nuclear physics, particle physics, and general relativity.* 1997.

[21] O. Benhar, *Structure and Dynamics of Compact Stars.* Lecture Notes in Physics, Springer International Publishing, 2023.

[22] A. Urbano and H. Veermäe, “On gravitational echoes from ultracompact exotic stars,” *JCAP*, vol. 04, p. 011, 2019.

[23] S. Chandrasekhar, “The maximum mass of ideal white dwarfs,” *Astrophys. J.*, vol. 74, pp. 81–82, 1931.

[24] J. R. Oppenheimer and G. M. Volkoff, “On massive neutron cores,” *Phys. Rev.*, vol. 55, pp. 374–381, 1939.

[25] R. C. Tolman, “Static solutions of Einstein’s field equations for spheres of fluid,” *Phys. Rev.*, vol. 55, pp. 364–373, 1939.

[26] V. Cardoso and P. Pani, “Testing the nature of dark compact objects: a status report,” *Living Rev. Rel.*, vol. 22, no. 1, p. 4, 2019.

[27] A. Alho, J. Natário, P. Pani, and G. Raposo, “Compactness bounds in general relativity,” *Phys. Rev. D*, vol. 106, no. 4, p. L041502, 2022.

[28] H. A. Buchdahl, “General Relativistic Fluid Spheres,” *Phys. Rev.*, vol. 116, p. 1027, 1959.

[29] J. Preskill, M. B. Wise, and F. Wilczek, “Cosmology of the Invisible Axion,” *Phys. Lett. B*, vol. 120, pp. 127–132, 1983.

[30] G. Steigman and M. S. Turner, “Cosmological Constraints on the Properties of Weakly Interacting Massive Particles,” *Nucl. Phys. B*, vol. 253, pp. 375–386, 1985.

[31] G. F. Giudice, M. McCullough, and A. Urbano, “Hunting for Dark Particles with Gravitational Waves,” *JCAP*, vol. 10, p. 001, 2016.

[32] L. Visinelli, “Boson stars and oscillatons: A review,” *Int. J. Mod. Phys. D*, vol. 30, no. 15, p. 2130006, 2021.

[33] G. Narain, J. Schaffner-Bielich, and I. N. Mishustin, “Compact stars made of fermionic dark matter,” *Phys. Rev. D*, vol. 74, p. 063003, 2006.

[34] A. H. Guth, M. P. Hertzberg, and C. Prescod-Weinstein, “Do Dark Matter Axions Form a Condensate with Long-Range Correlation?,” *Phys. Rev. D*, vol. 92, no. 10, p. 103513, 2015.

[35] M. Gorghetto, E. Hardy, J. March-Russell, N. Song, and S. M. West, “Dark photon stars: formation and role as dark matter substructure,” *JCAP*, vol. 08, no. 08, p. 018, 2022.

[36] P. O. Mazur and E. Mottola, “Gravitational vacuum condensate stars,” *Proc. Nat. Acad. Sci.*, vol. 101, pp. 9545–9550, 2004.

[37] U. H. Danielsson, G. Dibitetto, and S. Giri, “Black holes as bubbles of AdS,” *JHEP*, vol. 10, p. 171, 2017.

[38] J. Maldacena, A. Milekhin, and F. Popov, “Traversable wormholes in four dimensions,” *Class. Quant. Grav.*, vol. 40, no. 15, p. 155016, 2023.

[39] D. E. Kaplan and S. Rajendran, “Firewalls in General Relativity,” *Phys. Rev. D*, vol. 99, no. 4, p. 044033, 2019.

[40] K. Skenderis and M. Taylor, “The fuzzball proposal for black holes,” *Phys. Rept.*, vol. 467, pp. 117–171, 2008.

[41] M. Bianchi, D. Consoli, A. Grillo, J. F. Morales, P. Pani, and G. Raposo, “Distinguishing fuzzballs from black holes through their multipolar structure,” *Phys. Rev. Lett.*, vol. 125, no. 22, p. 221601, 2020.

[42] C. A. R. Herdeiro, “Black Holes: On the Universality of the Kerr Hypothesis,” *Lect. Notes Phys.*, vol. 1017, pp. 315–331, 2023.

[43] M. Bezares and N. Sanchis-Gual, “Exotic compact objects: a recent numerical-relativity perspective,” 6 2024.

[44] B. P. Abbott *et al.*, “GW170817: Observation of Gravitational Waves from a Binary Neutron Star Inspiral,” *Phys. Rev. Lett.*, vol. 119, no. 16, p. 161101, 2017.

[45] D. J. Kaup, “Klein-Gordon Geon,” *Phys. Rev.*, vol. 172, pp. 1331–1342, 1968.

[46] M. Colpi, S. L. Shapiro, and I. Wasserman, “Boson Stars: Gravitational Equilibria of Selfinteracting Scalar Fields,” *Phys. Rev. Lett.*, vol. 57, pp. 2485–2488, 1986.

[47] R. Brito, V. Cardoso, C. A. R. Herdeiro, and E. Radu, “Proca stars: Gravitating Bose–Einstein condensates of massive spin 1 particles,” *Phys. Lett. B*, vol. 752, pp. 291–295, 2016.

[48] C. Herdeiro, E. Radu, and E. dos Santos Costa Filho, “Proca-Higgs balls and stars in a UV completion for Proca self-interactions,” *JCAP*, vol. 05, p. 022, 2023.

[49] S. R. Coleman, “Q-balls,” *Nucl. Phys. B*, vol. 262, no. 2, p. 263, 1985. [Addendum: Nucl.Phys.B 269, 744 (1986)].

[50] G. H. Derrick, “Comments on nonlinear wave equations as models for elementary particles,” *J. Math. Phys.*, vol. 5, pp. 1252–1254, 1964.

[51] C. A. R. Herdeiro and J. a. M. S. Oliveira, “On the inexistence of solitons in Einstein–Maxwell-scalar models,” *Class. Quant. Grav.*, vol. 36, no. 10, p. 105015, 2019.

[52] U. Nucamendi and M. Salgado, “Scalar hairy black holes and solitons in asymptotically flat space-times,” *Phys. Rev. D*, vol. 68, p. 044026, 2003.

[53] F. E. Schunck and E. W. Mielke, “General relativistic boson stars,” *Class. Quant. Grav.*, vol. 20, pp. R301–R356, 2003.

[54] S. L. Liebling and C. Palenzuela, “Dynamical Boson Stars,” *Living Rev. Rel.*, vol. 15, p. 6, 2012.

[55] M. Gleiser, “Stability of Boson Stars,” *Phys. Rev. D*, vol. 38, p. 2376, 1988. [Erratum: Phys.Rev.D 39, 1257 (1989)].

[56] R. Garani, M. H. G. Tytgat, and J. Vandecasteele, “Condensed dark matter with a Yukawa interaction,” *Phys. Rev. D*, vol. 106, no. 11, p. 116003, 2022.

[57] J.-P. Hong, S. Jung, and K.-P. Xie, “Fermi-ball dark matter from a first-order phase transition,” *Phys. Rev. D*, vol. 102, no. 7, p. 075028, 2020.

[58] K. Kawana and K.-P. Xie, “Primordial black holes from a cosmic phase transition: The collapse of Fermi-balls,” *Phys. Lett. B*, vol. 824, p. 136791, 2022.

[59] F. Finster, J. Smoller, and S.-T. Yau, “Particlelike solutions of the einstein-dirac equations,” *Phys. Rev. D*, vol. 59, p. 104020, Apr 1999.

[60] P. E. D. Leith, C. A. Hooley, K. Horne, and D. G. Dritschel, “Nonlinear effects in the excited states of many-fermion einstein-dirac solitons,” *Phys. Rev. D*, vol. 104, p. 046024, Aug 2021.

[61] S. L. Shapiro and S. A. Teukolsky, *Black holes, white dwarfs, and neutron stars: The physics of compact objects.* 1983.

[62] T. Lee and Y. Pang, “Nontopological solitons,” *Physics Reports*, vol. 221, no. 5, pp. 251–350, 1992.

[63] B. Freivogel, T. Gasenzer, A. Hebecker, and S. Leonhardt, “A Conjecture on the Minimal Size of Bound States,” *SciPost Phys.*, vol. 8, no. 4, p. 058, 2020.

[64] D. Guerra, C. F. B. Macedo, and P. Pani, “Axion boson stars,” *JCAP*, vol. 09, no. 09, p. 061, 2019. [Erratum: JCAP 06, E01 (2020)].

[65] C. Alcock, E. Farhi, and A. Olinto, “Strange stars,” *Astrophys. J.*, vol. 310, pp. 261–272, 1986.

[66] P. Mathieu and T. F. Morris, “INSTABILITY OF STATIONARY STATES FOR NONLINEAR SPINOR MODELS WITH QUARTIC SELFINTERACTION,” *Phys. Lett. B*, vol. 126, pp. 74–76, 1983.

[67] F. V. Kusmartsev, E. W. Mielke, and F. E. Schunck, “Stability of neutron and boson stars: A New approach based on catastrophe theory,” 3 1991.

[68] P. O. Mazur and E. Mottola, “Gravitational Condensate Stars: An Alternative to Black Holes,” *Universe*, vol. 9, no. 2, p. 88, 2023.

[69] M. Visser and D. L. Wiltshire, “Stable gravastars: An Alternative to black holes?,” *Class. Quant. Grav.*, vol. 21, pp. 1135–1152, 2004.

[70] A. Corichi, U. Nucamendi, and M. Salgado, “Scalar hairy black holes and scalarons in the isolated horizons formalism,” *Phys. Rev. D*, vol. 73, p. 084002, 2006.

[71] X. Y. Chew, D.-h. Yeom, and J. L. Blázquez-Salcedo, “Properties of scalar hairy black holes and scalarons with asymmetric potential,” *Phys. Rev. D*, vol. 108, no. 4, p. 044020, 2023.

[72] X. Y. Chew and K.-G. Lim, “Scalar Hairy Black Holes with Inverted Mexican Hat Potential,” 7 2023.

[73] C. Cattoen, T. Faber, and M. Visser, “Gravastars must have anisotropic pressures,” *Class. Quant. Grav.*, vol. 22, pp. 4189–4202, 2005.

[74] T. Ogawa and H. Ishihara, “Solitonic gravastars in a U(1) gauge-Higgs model,” *Phys. Rev. D*, vol. 107, no. 12, p. L121501, 2023.

[75] R. Balkin, J. Serra, K. Springmann, S. Stelzl, and A. Weiler, “Heavy neutron stars from light scalars,” 7 2023.

[76] K. Saikawa, “A review of gravitational waves from cosmic domain walls,” *Universe*, vol. 3, no. 2, p. 40, 2017.

[77] J. A. Bagger and S. G. Naculich, “Quantum bags at strong coupling,” *Phys. Rev. D*, vol. 45, pp. 1395–1404, 1992.

[78] I. W. Stewart and P. G. Blunden, “Quantum solitons at strong coupling,” *Phys. Rev. D*, vol. 55, pp. 3742–3747, 1997.

[79] T. D. Lee and Y. Pang, “Nontopological solitons,” *Phys. Rept.*, vol. 221, pp. 251–350, 1992.

[80] R. Friedberg, T. D. Lee, and A. Sirlin, “A Class of Scalar-Field Soliton Solutions in Three Space Dimensions,” *Phys. Rev. D*, vol. 13, pp. 2739–2761, 1976.

[81] Y. Almumin, J. Heeck, A. Rajaraman, and C. B. Verhaaren, “Excited Q-balls,” *Eur. Phys. J. C*, vol. 82, no. 9, p. 801, 2022.

[82] R. Machleidt and D. R. Entem, “Chiral effective field theory and nuclear forces,” *Phys. Rept.*, vol. 503, pp. 1–75, 2011.

[83] J. R. Morones-Ibarra and A. Santos-Guevara, “A Calculation of the Sigma Meson Mass in Nuclear Matter,” *Acta Phys. Polon. B*, vol. 38, pp. 2553–2564, 2007.

[84] E. Witten, “Cosmic Separation of Phases,” *Phys. Rev. D*, vol. 30, pp. 272–285, 1984.

[85] R. W. Romani, D. Kandel, A. V. Filippenko, T. G. Brink, and W. Zheng, “PSR J0952−0607: The Fastest and Heaviest Known Galactic Neutron Star,” *Astrophys. J. Lett.*, vol. 934, no. 2, p. L17, 2022.

[86] V. Vijayan, N. Rahman, A. Bauswein, G. Martínez-Pinedo, and I. L. Arbina, “Impact of pions on binary neutron star mergers,” *Phys. Rev. D*, vol. 108, no. 2, p. 023020, 2023.

[87] M. Buballa and S. Carignano, “Inhomogeneous chiral symmetry breaking in dense neutron-star matter,” *Eur. Phys. J. A*, vol. 52, no. 3, p. 57, 2016.

[88] H. Niikura *et al.*, “Microlensing constraints on primordial black holes with Subaru/HSC Andromeda observations,” *Nature Astron.*, vol. 3, no. 6, pp. 524–534, 2019.

[89] H. Niikura, M. Takada, S. Yokoyama, T. Sumi, and S. Masaki, “Constraints on Earth-mass primordial black holes from OGLE 5-year microlensing events,” *Phys. Rev. D*, vol. 99, no. 8, p. 083503, 2019.

[90] S. Dimopoulos, B. W. Lynn, S. B. Selipsky, and N. Tetradis, “The Vacuum abhors top bags,” *Phys. Lett. B*, vol. 253, pp. 237–240, 1991.

[91] K.-M. Lee, J. A. Stein-Schabes, R. Watkins, and L. M. Widrow, “Gauged q Balls,” *Phys. Rev. D*, vol. 39, p. 1665, 1989.

[92] I. E. Gulamov, E. Y. Nugaev, A. G. Panin, and M. N. Smolyakov, “Some properties of U(1) gauged Q-balls,” *Phys. Rev. D*, vol. 92, no. 4, p. 045011, 2015.

[93] M. Fabbrichesi and A. Urbano, “Charged neutron stars and observational tests of a dark force weaker than gravity,” *JCAP*, vol. 06, p. 007, 2020.

[94] C. D. Froggatt and H. B. Nielsen, “Tunguska Dark Matter Ball,” *Int. J. Mod. Phys. A*, vol. 30, no. 13, p. 1550066, 2015.

[95] M. G. Alford, A. Schmitt, K. Rajagopal, and T. Schäfer, “Color superconductivity in dense quark matter,” *Rev. Mod. Phys.*, vol. 80, pp. 1455–1515, 2008.

[96] A. Lenz, “Constraints on a fourth generation of fermions from Higgs Boson searches,” *Adv. High Energy Phys.*, vol. 2013, p. 910275, 2013.

[97] A. G. Cohen, S. R. Coleman, H. Georgi, and A. Manohar, “The Evaporation of Q Balls,” *Nucl. Phys. B*, vol. 272, pp. 301–321, 1986.

[98] S.-S. Bao, X. Gong, Z.-G. Si, and Y.-F. Zhou, “Fourth generation Majorana neutrino, dark matter and Higgs physics,” *Int. J. Mod. Phys. A*, vol. 29, p. 1450010, 2014.

[99] G. Dvali, C. Gomez, L. Gruending, and T. Rug, “Towards a Quantum Theory of Solitons,” *Nucl. Phys. B*, vol. 901, pp. 338–353, 2015.

[100] E. Seidel and W.-M. Suen, “Formation of solitonic stars through gravitational cooling,” *Phys. Rev. Lett.*, vol. 72, pp. 2516–2519, 1994.

[101] R. Brito, V. Cardoso, and H. Okawa, “Accretion of dark matter by stars,” *Phys. Rev. Lett.*, vol. 115, no. 11, p. 111301, 2015.

[102] Y. B. Zel’dovich and I. D. Novikov, “The Hypothesis of Cores Retarded during Expansion and the Hot Cosmological Model,” *Soviet Astron. AJ (Engl. Transl.),*, vol. 10, p. 602, 1967.

[103] B. J. Carr and S. W. Hawking, “Black holes in the early Universe,” *Mon. Not. Roy. Astron. Soc.*, vol. 168, pp. 399–415, 1974.

[104] J. Alexander *et al.*, “Dark Sectors 2016 Workshop: Community Report,” 8 2016.

[105] J. A. Frieman, G. B. Gelmini, M. Gleiser, and E. W. Kolb, “Solitogenesis: Primordial Origin of Nontopological Solitons,” *Phys. Rev. Lett.*, vol. 60, p. 2101, 1988.

[106] K. Griest and E. W. Kolb, “Solitosynthesis: Cosmological Evolution of Nontopological Solitons,” *Phys. Rev. D*, vol. 40, p. 3231, 1989.

[107] W. N. Cottingham and R. Vinh Mau, “Soliton stars at finite temperature,” *Phys. Lett. B*, vol. 261, pp. 93–96, 1991.

[108] Y. Bai, S. Lu, and N. Orlofsky, “Origin of nontopological soliton dark matter: solitosynthesis or phase transition,” *JHEP*, vol. 10, p. 181, 2022.

[109] G. Domènech and M. Sasaki, “Cosmology of strongly interacting fermions in the early universe,” *JCAP*, vol. 06, p. 030, 2021.

[110] G. Domènech, D. Inman, A. Kusenko, and M. Sasaki, “Halo formation from Yukawa forces in the very early Universe,” *Phys. Rev. D*, vol. 108, no. 10, p. 103543, 2023.

[111] M. M. Flores, Y. Lu, and A. Kusenko, “Structure Formation after Reheating: Supermassive Primordial Black Holes and Fermi Ball Dark Matter,” 8 2023.

[112] F. Crescimbeni, G. Franciolini, P. Pani, and A. Riotto, “Primordial black holes or else? Tidal tests on subsolar mass gravitational-wave observations,” 2 2024.

[113] J. Golomb, I. Legred, K. Chatziioannou, A. Abac, and T. Dietrich, “Using Equation of State Constraints to Classify Low-Mass Compact Binary Mergers,” 3 2024.

[114] M. A. Luty, “Dynamical Electroweak Symmetry Breaking With Two Composite Higgs Doublets,” *Phys. Rev. D*, vol. 41, p. 2893, 1990.

[115] C. Csaki, “The Minimal supersymmetric standard model (MSSM),” *Mod. Phys. Lett. A*, vol. 11, p. 599, 1996.

[116] A. Delgado and M. Quirós, “Higgsino Dark Matter in the MSSM,” *Phys. Rev. D*, vol. 103, no. 1, p. 015024, 2021.

[117] S. Antusch, O. Fischer, A. Hammad, and C. Scherb, “Low scale type II seesaw: Present constraints and prospects for displaced vertex searches,” *JHEP*, vol. 02, p. 157, 2019.

[118] M. Carena, A. Megevand, M. Quiros, and C. E. M. Wagner, “Electroweak baryogenesis and new TeV fermions,” *Nucl. Phys. B*, vol. 716, pp. 319–351, 2005.

[119] A. Angelescu and P. Huang, “Multistep Strongly First Order Phase Transitions from New Fermions at the TeV Scale,” *Phys. Rev. D*, vol. 99, no. 5, p. 055023, 2019.

[120] Y. Endo, H. Ishihara, and T. Ogawa, “Relativistic nontopological soliton stars in a U(1) gauge Higgs model,” *Phys. Rev. D*, vol. 105, no. 10, p. 104041, 2022.

[121] M. Khlopov, B. A. Malomed, and I. B. Zeldovich, “Gravitational instability of scalar fields and formation of primordial black holes,” *Mon. Not. Roy. Astron. Soc.*, vol. 215, pp. 575–589, 1985.

[122] V. De Luca, G. Franciolini, A. Kehagias, P. Pani, and A. Riotto, “Primordial Black Holes in Matter-Dominated Eras: the Role of Accretion,” 12 2021.

[123] T. Kim, P. Lu, D. Marfatia, and V. Takhistov, “Regurgitated Dark Matter,” 9 2023.

[124] M. Lewicki, K. Müürsepp, J. Pata, M. Vasar, V. Vaskonen, and H. Veermäe, “Dynamics of false vacuum bubbles with trapped particles,” 5 2023.

[125] P. Huang and K.-P. Xie, “Primordial black holes from an electroweak phase transition,” *Phys. Rev. D*, vol. 105, no. 11, p. 115033, 2022.

[126] M. Bailes *et al.*, “Gravitational-wave physics and astronomy in the 2020s and 2030s,” *Nature Rev. Phys.*, vol. 3, no. 5, pp. 344–366, 2021.

[127] A. Ori and K. S. Thorne, “The Transition from inspiral to plunge for a compact body in a circular equatorial orbit around a massive, spinning black hole,” *Phys. Rev. D*, vol. 62, p. 124022, 2000.

[128] D. Lai and A. G. Wiseman, "Innermost stable circular orbit of inspiraling neutron star binaries: Tidal effects, postNewtonian effects and the neutron star equation of state," *Phys. Rev. D*, vol. 54, pp. 3958–3964, 1996.

[129] T. Sukhbold, T. Ertl, S. E. Woosley, J. M. Brown, and H. T. Janka, "Core-Collapse Supernovae from 9 to 120 Solar Masses Based on Neutrino-powered Explosions," *Astrophys. J.*, vol. 821, no. 1, p. 38, 2016.

[130] M. Colpi, S. Shapiro, and S. Teukolsky, "The explosion of a rotating neutron star near the minimum mass," 6 1990.

[131] V. Domcke, C. Garcia-Cely, and N. L. Rodd, "Novel Search for High-Frequency Gravitational Waves with Low-Mass Axion Haloscopes," *Phys. Rev. Lett.*, vol. 129, no. 4, p. 041101, 2022.

[132] W. M. Farr, N. Sravan, A. Cantrell, L. Kreidberg, C. D. Bailyn, I. Mandel, and V. Kalogera, "The mass distribution of stellar-mass black holes," *The Astrophysical Journal*, vol. 741, p. 103, Oct. 2011.

[133] G. Franciolini, K. Kritos, L. Reali, F. Broekgaarden, and E. Berti, "Observing black hole mergers beyond the pair-instability mass gap with next-generation gravitational wave detectors," *Phys. Rev. D*, vol. 110, no. 2, p. 023036, 2024.

[134] C. E. Rhoades, Jr. and R. Ruffini, "Maximum mass of a neutron star," *Phys. Rev. Lett.*, vol. 32, pp. 324–327, 1974.

[135] R. Abbott *et al.*, "GW190814: Gravitational Waves from the Coalescence of a 23 Solar Mass Black Hole with a 2.6 Solar Mass Compact Object," *Astrophys. J. Lett.*, vol. 896, no. 2, p. L44, 2020.

[136] A. G. Abac *et al.*, "Observation of Gravitational Waves from the Coalescence of a 2.5–4.5 M Compact Object and a Neutron Star," *Astrophys. J. Lett.*, vol. 970, no. 2, p. L34, 2024.

[137] E. Poisson and C. M. Will, *Gravity: Newtonian, Post-Newtonian, Relativistic.* Cambridge University Press, 2014.

[138] N. V. Krishnendu, K. G. Arun, and C. K. Mishra, "Testing the binary black hole nature of a compact binary coalescence," *Phys. Rev. Lett.*, vol. 119, no. 9, p. 091101, 2017.

[139] S. Kastha, A. Gupta, K. G. Arun, B. S. Sathyaprakash, and C. Van Den Broeck, "Testing the multipole structure of compact binaries using gravitational wave observations," *Phys. Rev. D*, vol. 98, no. 12, p. 124033, 2018.

[140] H. S. Chia, Z. Zhou, and M. M. Ivanov, "Bring the Heat: Tidal Heating Constraints for Black Holes and Exotic Compact Objects from the LIGO-Virgo-KAGRA Data," 4 2024.

[141] C. M. Will, *Gravity: Newtonian, Post-Newtonian, and General Relativistic*, pp. 9–72. 2016.

[142] K. S. Thorne, “Multipole Expansions of Gravitational Radiation,” *Rev. Mod. Phys.*, vol. 52, pp. 299–339, 1980.

[143] V. Cardoso and L. Gualtieri, “Testing the black hole ‘no-hair’ hypothesis,” *Class. Quant. Grav.*, vol. 33, no. 17, p. 174001, 2016.

[144] S. W. Hawking and G. F. R. Ellis, *The Large Scale Structure of Space-Time*. Cambridge Monographs on Mathematical Physics, Cambridge University Press, 2 2023.

[145] B. Carter, “Axisymmetric Black Hole Has Only Two Degrees of Freedom,” *Phys. Rev. Lett.*, vol. 26, pp. 331–333, 1971.

[146] L. Blanchet, “Gravitational radiation from postNewtonian sources and inspiraling compact binaries,” *Living Rev. Rel.*, vol. 5, p. 3, 2002.

[147] N. K. Johnson-Mcdaniel, A. Mukherjee, R. Kashyap, P. Ajith, W. Del Pozzo, and S. Vitale, “Constraining black hole mimickers with gravitational wave observations,” *Phys. Rev. D*, vol. 102, p. 123010, 2020.

[148] N. Sennett, T. Hinderer, J. Steinhoff, A. Buonanno, and S. Ossokine, “Distinguishing Boson Stars from Black Holes and Neutron Stars from Tidal Interactions in Inspiraling Binary Systems,” *Phys. Rev. D*, vol. 96, no. 2, p. 024002, 2017.

[149] M. Vaglio, C. Pacilio, A. Maselli, and P. Pani, “Multipolar structure of rotating boson stars,” *Phys. Rev. D*, vol. 105, no. 12, p. 124020, 2022.

[150] A. E. H. Love, “Earth, the yielding of the, to disturbing forces,” *Mont. Not. Roy. Astr. Soc.*, vol. 69, p. 476, Apr. 1909.

[151] T. Hinderer, “Tidal Love numbers of neutron stars,” *Astrophys. J.*, vol. 677, pp. 1216–1220, 2008. [Erratum: Astrophys.J. 697, 964 (2009)].

[152] T. Binnington and E. Poisson, “Relativistic theory of tidal Love numbers,” *Phys. Rev. D*, vol. 80, p. 084018, 2009.

[153] T. Damour and A. Nagar, “Relativistic tidal properties of neutron stars,” *Phys. Rev. D*, vol. 80, p. 084035, 2009.

[154] L. Baiotti, T. Damour, B. Giacomazzo, A. Nagar, and L. Rezzolla, “Analytic modelling of tidal effects in the relativistic inspiral of binary neutron stars,” *Phys. Rev. Lett.*, vol. 105, p. 261101, 2010.

[155] L. Baiotti, T. Damour, B. Giacomazzo, A. Nagar, and L. Rezzolla, “Accurate numerical simulations of inspiralling binary neutron stars and their comparison with effective-one-body analytical models,” *Phys. Rev. D*, vol. 84, p. 024017, 2011.

[156] J. Vines, E. E. Flanagan, and T. Hinderer, “Post-1-Newtonian tidal effects in the gravitational waveform from binary inspirals,” *Phys. Rev. D*, vol. 83, p. 084051, 2011.

[157] F. Pannarale, L. Rezzolla, F. Ohme, and J. S. Read, “Will black hole-neutron star binary inspirals tell us about the neutron star equation of state?,” *Phys. Rev. D*, vol. 84, p. 104017, 2011.

[158] J. E. Vines and E. E. Flanagan, “Post-1-Newtonian quadrupole tidal interactions in binary systems,” *Phys. Rev. D*, vol. 88, p. 024046, 2013.

[159] B. D. Lackey, K. Kyutoku, M. Shibata, P. R. Brady, and J. L. Friedman, “Extracting equation of state parameters from black hole-neutron star mergers. I. Nonspinning black holes,” *Phys. Rev. D*, vol. 85, p. 044061, 2012.

[160] B. D. Lackey, K. Kyutoku, M. Shibata, P. R. Brady, and J. L. Friedman, “Extracting equation of state parameters from black hole-neutron star mergers: aligned-spin black holes and a preliminary waveform model,” *Phys. Rev. D*, vol. 89, no. 4, p. 043009, 2014.

[161] E. E. Flanagan and T. Hinderer, “Constraining neutron star tidal Love numbers with gravitational wave detectors,” *Phys. Rev. D*, vol. 77, p. 021502, 2008.

[162] M. Favata, “Systematic parameter errors in inspiraling neutron star binaries,” *Phys. Rev. Lett.*, vol. 112, p. 101101, 2014.

[163] K. Yagi and N. Yunes, “Love can be Tough to Measure,” *Phys. Rev. D*, vol. 89, no. 2, p. 021303, 2014.

[164] A. Maselli, V. Cardoso, V. Ferrari, L. Gualtieri, and P. Pani, “Equation-of-state-independent relations in neutron stars,” *Phys. Rev. D*, vol. 88, no. 2, p. 023007, 2013.

[165] A. Maselli, L. Gualtieri, and V. Ferrari, “Constraining the equation of state of nuclear matter with gravitational wave observations: Tidal deformability and tidal disruption,” *Phys. Rev. D*, vol. 88, no. 10, p. 104040, 2013.

[166] W. Del Pozzo, T. G. F. Li, M. Agathos, C. Van Den Broeck, and S. Vitale, “Demonstrating the feasibility of probing the neutron star equation of state with second-generation gravitational wave detectors,” *Phys. Rev. Lett.*, vol. 111, no. 7, p. 071101, 2013.

[167] B. P. Abbott *et al.*, “GW170817: Observation of Gravitational Waves from a Binary Neutron Star Inspiral,” *Phys. Rev. Lett.*, vol. 119, no. 16, p. 161101, 2017.

[168] A. Bauswein, O. Just, H.-T. Janka, and N. Stergioulas, “Neutron-star radius constraints from GW170817 and future detections,” *Astrophys. J. Lett.*, vol. 850, no. 2, p. L34, 2017.

[169] E. R. Most, L. R. Weih, L. Rezzolla, and J. Schaffner-Bielich, “New constraints on radii and tidal deformabilities of neutron stars from GW170817,” *Phys. Rev. Lett.*, vol. 120, no. 26, p. 261103, 2018.

[170] I. Harry and T. Hinderer, "Observing and measuring the neutron-star equation-of-state in spinning binary neutron star systems," *Class. Quant. Grav.*, vol. 35, no. 14, p. 145010, 2018.

[171] E. Annala, T. Gorda, A. Kurkela, and A. Vuorinen, "Gravitational-wave constraints on the neutron-star-matter Equation of State," *Phys. Rev. Lett.*, vol. 120, no. 17, p. 172703, 2018.

[172] B. P. Abbott *et al.*, "GW170817: Measurements of neutron star radii and equation of state," *Phys. Rev. Lett.*, vol. 121, no. 16, p. 161101, 2018.

[173] S. Akcay, S. Bernuzzi, F. Messina, A. Nagar, N. Ortiz, and P. Rettegno, "Effective-one-body multipolar waveform for tidally interacting binary neutron stars up to merger," *Phys. Rev. D*, vol. 99, no. 4, p. 044051, 2019.

[174] T. Abdelsalhin, L. Gualtieri, and P. Pani, "Post-Newtonian spin-tidal couplings for compact binaries," *Phys. Rev. D*, vol. 98, no. 10, p. 104046, 2018.

[175] X. Jiménez Forteza, T. Abdelsalhin, P. Pani, and L. Gualtieri, "Impact of high-order tidal terms on binary neutron-star waveforms," *Phys. Rev. D*, vol. 98, no. 12, p. 124014, 2018.

[176] B. Banihashemi and J. Vines, "Gravitomagnetic tidal effects in gravitational waves from neutron star binaries," *Phys. Rev. D*, vol. 101, no. 6, p. 064003, 2020.

[177] T. Dietrich, A. Samajdar, S. Khan, N. K. Johnson-McDaniel, R. Dudi, and W. Tichy, "Improving the NRTidal model for binary neutron star systems," *Phys. Rev. D*, vol. 100, no. 4, p. 044003, 2019.

[178] T. Dietrich, T. Hinderer, and A. Samajdar, "Interpreting Binary Neutron Star Mergers: Describing the Binary Neutron Star Dynamics, Modelling Gravitational Waveforms, and Analyzing Detections," *Gen. Rel. Grav.*, vol. 53, no. 3, p. 27, 2021.

[179] Q. Henry, G. Faye, and L. Blanchet, "Tidal effects in the gravitational-wave phase evolution of compact binary systems to next-to-next-to-leading post-Newtonian order," *Phys. Rev. D*, vol. 102, no. 4, p. 044033, 2020.

[180] C. Pacilio, A. Maselli, M. Fasano, and P. Pani, "Ranking the Love for the neutron star equation of state: the need for third-generation detectors," 4 2021.

[181] A. Maselli, A. Sabatucci, and O. Benhar, "Constraining three-nucleon forces with multimessenger data," *Phys. Rev. C*, vol. 103, no. 6, p. 065804, 2021.

[182] A. Guerra Chaves and T. Hinderer, "Probing the equation of state of neutron star matter with gravitational waves from binary inspirals in light of GW170817: a brief review," *J. Phys. G*, vol. 46, no. 12, p. 123002, 2019.

[183] K. Chatziioannou, "Neutron star tidal deformability and equation of state constraints," *Gen. Rel. Grav.*, vol. 52, no. 11, p. 109, 2020.

[184] K. Yagi and N. Yunes, “I-Love-Q,” *Science*, vol. 341, pp. 365–368, 2013.

[185] K. Yagi and N. Yunes, “I-Love-Q Relations in Neutron Stars and their Applications to Astrophysics, Gravitational Waves and Fundamental Physics,” *Phys. Rev. D*, vol. 88, no. 2, p. 023009, 2013.

[186] K. Yagi and N. Yunes, “I-Love-Q Relations: From Compact Stars to Black Holes,” *Class. Quant. Grav.*, vol. 33, no. 9, p. 095005, 2016.

[187] K. Yagi, “Multipole Love Relations,” *Phys. Rev. D*, vol. 89, no. 4, p. 043011, 2014. [Erratum: Phys.Rev.D 96, 129904 (2017), Erratum: Phys.Rev.D 97, 129901 (2018)].

[188] T. Delsate, “I-Love relations for irrotational stars,” *Phys. Rev. D*, vol. 92, no. 12, p. 124001, 2015.

[189] T. Damour and O. M. Lecian, “On the gravitational polarizability of black holes,” *Phys. Rev. D*, vol. 80, p. 044017, 2009.

[190] P. Pani, L. Gualtieri, A. Maselli, and V. Ferrari, “Tidal deformations of a spinning compact object,” *Phys. Rev. D*, vol. 92, no. 2, p. 024010, 2015.

[191] P. Pani, L. Gualtieri, and V. Ferrari, “Tidal Love numbers of a slowly spinning neutron star,” *Phys. Rev. D*, vol. 92, no. 12, p. 124003, 2015.

[192] N. Gürlebeck, “No-hair theorem for Black Holes in Astrophysical Environments,” *Phys. Rev. Lett.*, vol. 114, no. 15, p. 151102, 2015.

[193] R. A. Porto, “The Tune of Love and the Nature(ness) of Spacetime,” *Fortsch. Phys.*, vol. 64, no. 10, pp. 723–729, 2016.

[194] A. Le Tiec and M. Casals, “Spinning Black Holes Fall in Love,” *Phys. Rev. Lett.*, vol. 126, no. 13, p. 131102, 2021.

[195] H. S. Chia, “Tidal deformation and dissipation of rotating black holes,” *Phys. Rev. D*, vol. 104, no. 2, p. 024013, 2021.

[196] A. Le Tiec, M. Casals, and E. Franzin, “Tidal Love Numbers of Kerr Black Holes,” *Phys. Rev. D*, vol. 103, no. 8, p. 084021, 2021.

[197] P. Charalambous, S. Dubovsky, and M. M. Ivanov, “On the Vanishing of Love Numbers for Kerr Black Holes,” *JHEP*, vol. 05, p. 038, 2021.

[198] P. Charalambous, S. Dubovsky, and M. M. Ivanov, “Hidden Symmetry of Vanishing Love Numbers,” *Phys. Rev. Lett.*, vol. 127, no. 10, p. 101101, 2021.

[199] M. M. Ivanov and Z. Zhou, “Revisiting the matching of black hole tidal responses: A systematic study of relativistic and logarithmic corrections,” *Phys. Rev. D*, vol. 107, no. 8, p. 084030, 2023.

[200] P. Charalambous, S. Dubovsky, and M. M. Ivanov, “Love symmetry,” *JHEP*, vol. 10, p. 175, 2022.

[201] T. Katagiri, M. Kimura, H. Nakano, and K. Omukai, "Vanishing Love numbers of black holes in general relativity: From spacetime conformal symmetry of a two-dimensional reduced geometry," *Phys. Rev. D*, vol. 107, no. 12, p. 124030, 2023.

[202] M. M. Ivanov and Z. Zhou, "Vanishing of Black Hole Tidal Love Numbers from Scattering Amplitudes," *Phys. Rev. Lett.*, vol. 130, no. 9, p. 091403, 2023.

[203] R. Berens, L. Hui, and Z. Sun, "Ladder symmetries of black holes and de Sitter space: love numbers and quasinormal modes," *JCAP*, vol. 06, p. 056, 2023.

[204] R. P. Bhatt, S. Chakraborty, and S. Bose, "Addressing issues in defining the Love numbers for black holes," *Phys. Rev. D*, vol. 108, no. 8, p. 084013, 2023.

[205] C. Sharma, R. Ghosh, and S. Sarkar, "Exploring ladder symmetry and Love numbers for static and rotating black holes," *Phys. Rev. D*, vol. 109, no. 4, p. L041505, 2024.

[206] P. Pani, "I-Love-Q relations for gravastars and the approach to the black-hole limit," *Phys. Rev. D*, vol. 92, no. 12, p. 124030, 2015. [Erratum: Phys.Rev.D 95, 049902 (2017)].

[207] V. Cardoso, E. Franzin, A. Maselli, P. Pani, and G. Raposo, "Testing strong-field gravity with tidal Love numbers," *Phys. Rev. D*, vol. 95, no. 8, p. 084014, 2017. [Addendum: Phys.Rev.D 95, 089901 (2017)].

[208] S. Nair, S. Chakraborty, and S. Sarkar, "Asymptotically de Sitter black holes have nonzero tidal Love numbers," *Phys. Rev. D*, vol. 109, no. 6, p. 064025, 2024.

[209] V. Cardoso, M. Kimura, A. Maselli, and L. Senatore, "Black Holes in an Effective Field Theory Extension of General Relativity," *Phys. Rev. Lett.*, vol. 121, no. 25, p. 251105, 2018.

[210] V. De Luca, J. Khoury, and S. S. C. Wong, "Implications of the weak gravity conjecture for tidal Love numbers of black holes," *Phys. Rev. D*, vol. 108, no. 4, p. 044066, 2023.

[211] B. Kol and M. Smolkin, "Black hole stereotyping: Induced gravito-static polarization," *JHEP*, vol. 02, p. 010, 2012.

[212] V. Cardoso, L. Gualtieri, and C. J. Moore, "Gravitational waves and higher dimensions: Love numbers and Kaluza-Klein excitations," *Phys. Rev. D*, vol. 100, no. 12, p. 124037, 2019.

[213] L. Hui, A. Joyce, R. Penco, L. Santoni, and A. R. Solomon, "Static response and Love numbers of Schwarzschild black holes," *JCAP*, vol. 04, p. 052, 2021.

[214] M. J. Rodriguez, L. Santoni, A. R. Solomon, and L. F. Temoche, "Love numbers for rotating black holes in higher dimensions," *Phys. Rev. D*, vol. 108, no. 8, p. 084011, 2023.

[215] P. Charalambous and M. M. Ivanov, “Scalar Love numbers and Love symmetries of 5-dimensional Myers-Perry black holes,” *JHEP*, vol. 07, p. 222, 2023.

[216] P. Charalambous, “Love numbers and Love symmetries for p-form and gravitational perturbations of higher-dimensional spherically symmetric black holes,” *JHEP*, vol. 04, p. 122, 2024.

[217] D. Baumann, H. S. Chia, and R. A. Porto, “Probing Ultralight Bosons with Binary Black Holes,” *Phys. Rev. D*, vol. 99, no. 4, p. 044001, 2019.

[218] V. Cardoso and F. Duque, “Environmental effects in gravitational-wave physics: Tidal deformability of black holes immersed in matter,” *Phys. Rev. D*, vol. 101, no. 6, p. 064028, 2020.

[219] V. De Luca and P. Pani, “Tidal deformability of dressed black holes and tests of ultralight bosons in extended mass ranges,” *JCAP*, vol. 08, p. 032, 2021.

[220] V. Cardoso, K. Destounis, F. Duque, R. P. Macedo, and A. Maselli, “Black holes in galaxies: Environmental impact on gravitational-wave generation and propagation,” *Phys. Rev. D*, vol. 105, no. 6, p. L061501, 2022.

[221] V. De Luca, A. Maselli, and P. Pani, “Modeling frequency-dependent tidal deformability for environmental black hole mergers,” *Phys. Rev. D*, vol. 107, no. 4, p. 044058, 2023.

[222] E. Cannizzaro, V. De Luca, and P. Pani, “Tidal deformability of black holes surrounded by thin accretion disks,” 8 2024.

[223] S. Nair, S. Chakraborty, and S. Sarkar, “Dynamical Love numbers for area quantized black holes,” *Phys. Rev. D*, vol. 107, no. 12, p. 124041, 2023.

[224] M. V. S. Saketh, Z. Zhou, and M. M. Ivanov, “Dynamical tidal response of Kerr black holes from scattering amplitudes,” *Phys. Rev. D*, vol. 109, no. 6, p. 064058, 2024.

[225] M. Perry and M. J. Rodriguez, “Dynamical Love Numbers for Kerr Black Holes,” 10 2023.

[226] S. Chakraborty, E. Maggio, M. Silvestrini, and P. Pani, “Dynamical tidal Love numbers of Kerr-like compact objects,” 10 2023.

[227] V. De Luca, J. Khoury, and S. S. C. Wong, “Nonlinearities in the tidal Love numbers of black holes,” *Phys. Rev. D*, vol. 108, no. 2, p. 024048, 2023.

[228] M. M. Riva, L. Santoni, N. Savić, and F. Vernizzi, “Vanishing of Nonlinear Tidal Love Numbers of Schwarzschild Black Holes,” 12 2023.

[229] S. Iteanu, M. M. Riva, L. Santoni, N. Savić, and F. Vernizzi, “Vanishing of Quadratic Love Numbers of Schwarzschild Black Holes,” 10 2024.

[230] V. Kalogera *et al.*, “The Next Generation Global Gravitational Wave Observatory: The Science Book,” 11 2021.

[231] M. Maggiore *et al.*, “Science Case for the Einstein Telescope,” *JCAP*, vol. 03, p. 050, 2020.

[232] M. Branchesi *et al.*, “Science with the Einstein Telescope: a comparison of different designs,” *JCAP*, vol. 07, p. 068, 2023.

[233] B. P. Abbott *et al.*, “Exploring the Sensitivity of Next Generation Gravitational Wave Detectors,” *Class. Quant. Grav.*, vol. 34, no. 4, p. 044001, 2017.

[234] R. Essick, S. Vitale, and M. Evans, “Frequency-dependent responses in third generation gravitational-wave detectors,” *Phys. Rev. D*, vol. 96, no. 8, p. 084004, 2017.

[235] X. Jiménez Forteza, T. Abdelsalhin, P. Pani, and L. Gualtieri, “Impact of high-order tidal terms on binary neutron-star waveforms,” *Phys. Rev. D*, vol. 98, no. 12, p. 124014, 2018.

[236] H. S. Chia, T. D. P. Edwards, D. Wadekar, A. Zimmerman, S. Olsen, J. Roulet, T. Venumadhav, B. Zackay, and M. Zaldarriaga, “In pursuit of Love numbers: First templated search for compact objects with large tidal deformabilities in the LIGO-Virgo data,” *Phys. Rev. D*, vol. 110, no. 6, p. 063007, 2024.

[237] E. Berti, V. Cardoso, and A. O. Starinets, “Quasinormal modes of black holes and black branes,” *Class. Quant. Grav.*, vol. 26, p. 163001, 2009.

[238] P. Pani, E. Berti, V. Cardoso, Y. Chen, and R. Norte, “Gravitational wave signatures of the absence of an event horizon. I. Nonradial oscillations of a thin-shell gravastar,” *Phys. Rev. D*, vol. 80, p. 124047, 2009.

[239] C. F. B. Macedo, P. Pani, V. Cardoso, and L. C. B. Crispino, “Astrophysical signatures of boson stars: quasinormal modes and inspiral resonances,” *Phys. Rev. D*, vol. 88, no. 6, p. 064046, 2013.

[240] K. K. Nandi, R. N. Izmailov, A. A. Yanbekov, and A. A. Shayakhmetov, “Ring-down gravitational waves and lensing observables: How far can a wormhole mimic those of a black hole?,” *Phys. Rev. D*, vol. 95, no. 10, p. 104011, 2017.

[241] E. Berti, V. Cardoso, and C. M. Will, “On gravitational-wave spectroscopy of massive black holes with the space interferometer LISA,” *Phys. Rev. D*, vol. 73, p. 064030, 2006.

[242] E. Berti, A. Sesana, E. Barausse, V. Cardoso, and K. Belczynski, “Spectroscopy of Kerr black holes with Earth- and space-based interferometers,” *Phys. Rev. Lett.*, vol. 117, no. 10, p. 101102, 2016.

[243] J. Abedi and N. Afshordi, “Echoes from the Abyss: A highly spinning black hole remnant for the binary neutron star merger GW170817,” *JCAP*, vol. 11, p. 010, 2019.

[244] E. Maggio, A. Testa, S. Bhagwat, and P. Pani, “Analytical model for gravitational-wave echoes from spinning remnants,” *Phys. Rev. D*, vol. 100, no. 6, p. 064056, 2019.

[245] V. Cardoso and P. Pani, “Tests for the existence of black holes through gravitational wave echoes,” *Nature Astron.*, vol. 1, no. 9, pp. 586–591, 2017.

[246] T. Regge and J. A. Wheeler, “Stability of a Schwarzschild singularity,” *Phys. Rev.*, vol. 108, pp. 1063–1069, 1957.

[247] P. Pani, L. Gualtieri, T. Abdelsalhin, and X. Jiménez-Forteza, “Magnetic tidal Love numbers clarified,” *Phys. Rev. D*, vol. 98, no. 12, p. 124023, 2018.

[248] P. Landry and E. Poisson, “Gravitomagnetic response of an irrotational body to an applied tidal field,” *Phys. Rev. D*, vol. 91, no. 10, p. 104026, 2015.

[249] T. Abdelsalhin, *Tidal deformations of compact objects and gravitational wave emission.* PhD thesis, Rome U., 2019.

[250] Y. Kojima, “Equations governing the nonradial oscillations of a slowly rotating relativistic star,” *Phys. Rev. D*, vol. 46, pp. 4289–4303, 1992.

[251] T. Hinderer, B. D. Lackey, R. N. Lang, and J. S. Read, “Tidal deformability of neutron stars with realistic equations of state and their gravitational wave signatures in binary inspiral,” *Phys. Rev. D*, vol. 81, p. 123016, 2010.

[252] S. L. Shapiro and S. A. Teukolsky, *Black holes, white dwarfs and neutron stars. The physics of compact objects.* 1983.

[253] J. Audouze, R. Schaeffer, and J. Silk, “High Energy Cosmic Ray Signature of Quark Nuggets,” in *19th International Cosmic Ray Conference (ICRC19), Volume 8*, vol. 8 of *International Cosmic Ray Conference*, p. 290, Aug. 1985.

[254] Y. Bai, A. J. Long, and S. Lu, “Dark Quark Nuggets,” *Phys. Rev. D*, vol. 99, no. 5, p. 055047, 2019.

[255] R. Brito, V. Cardoso, and P. Pani, “Superradiance,” *Lect. Notes Phys.*, vol. 906, pp. pp.1–237, 2015.

[256] R. Hill, K. W. Masui, and D. Scott, “The Spectrum of the Universe,” *Appl. Spectrosc.*, vol. 72, no. 5, pp. 663–688, 2018.

[257] S. Valdez-Alvarado, C. Palenzuela, D. Alic, and L. A. Ureña López, “Dynamical evolution of fermion-boson stars,” *Phys. Rev. D*, vol. 87, no. 8, p. 084040, 2013.

[258] K. Griest, E. W. Kolb, and A. Massarotti, “Statistical Fluctuations as the Origin of Nontopological Solitons,” *Phys. Rev. D*, vol. 40, p. 3529, 1989.

[259] D. D. Doneva and S. S. Yazadjiev, “Beyond the spontaneous scalarization: New fully nonlinear mechanism for the formation of scalarized black holes and its dynamical development,” *Phys. Rev. D*, vol. 105, no. 4, p. L041502, 2022.

[260] E. Berti *et al.*, “Testing General Relativity with Present and Future Astrophysical Observations,” *Class. Quant. Grav.*, vol. 32, p. 243001, 2015.

[261] T. P. Sotiriou and V. Faraoni, “f(R) Theories Of Gravity,” *Rev. Mod. Phys.*, vol. 82, pp. 451–497, 2010.